AD-A069 779 ILLINOIS UNIV AT URBANA-CHAMPAIGN COORDINATED SCIENCE LAB F/6 20/2
STUDIES OF HIGH-DOSE ION IMPLANTATION IN SILICON.(U)
SEP 78 M Y TSAI DAAB07-72-C-0259
UNCLASSIFIED R-824 NL

1 OF 2
AD
A069779

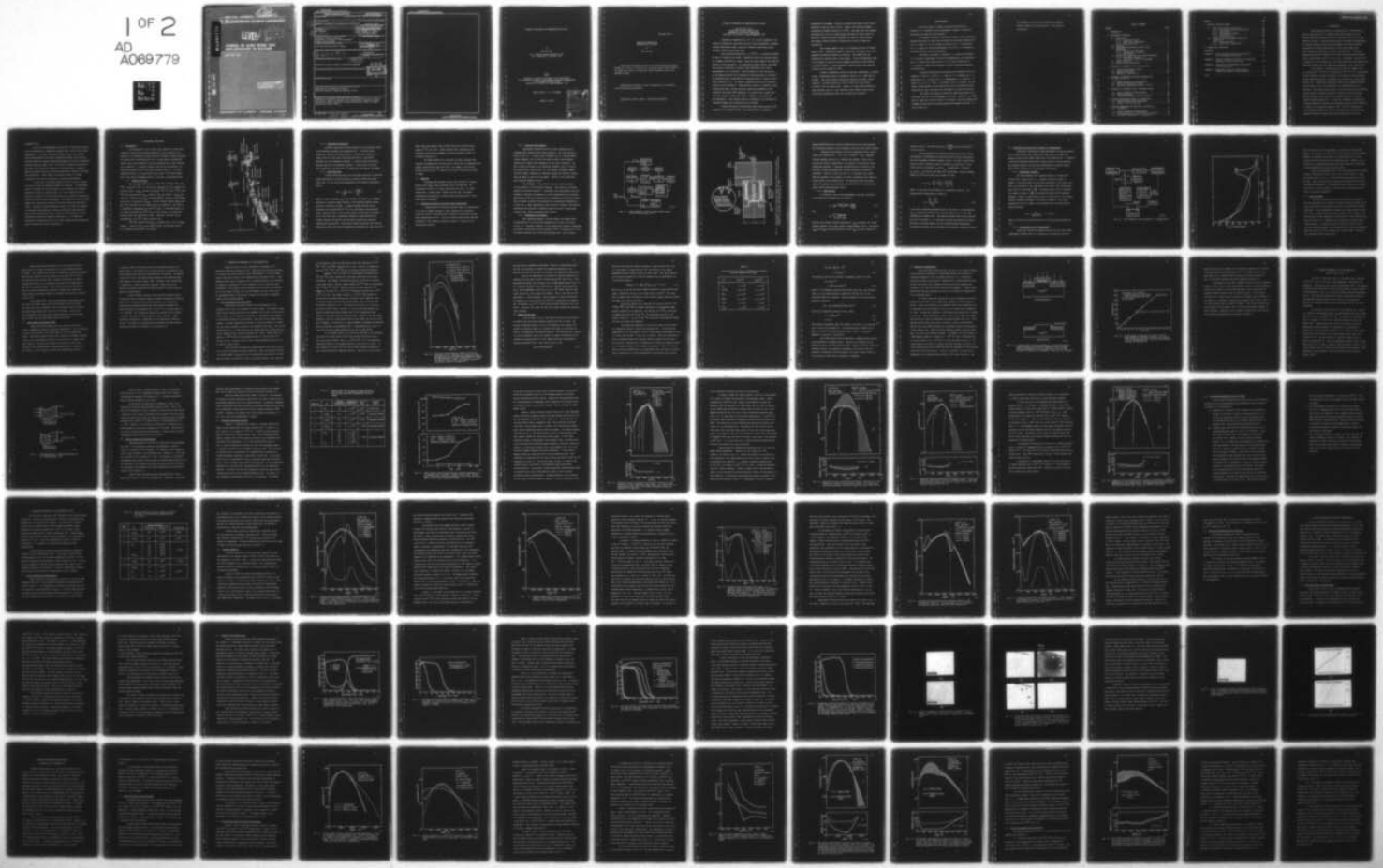

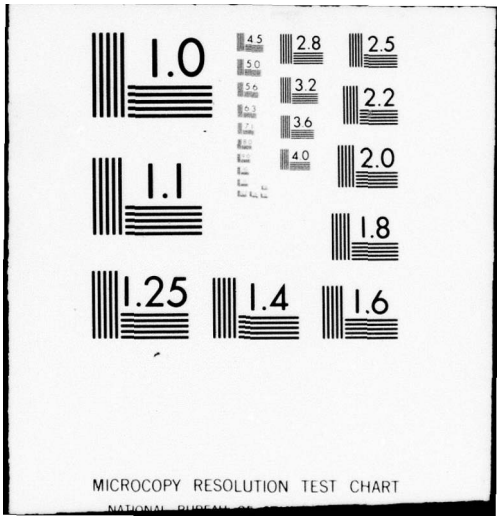
1.0
1.1
1.25
1.4
1.6
1.8
2.0
2.2
2.5
2.8
3.2
3.6
4.0
4.5
5.0
5.6
6.3
7.1
8.0
9.0
MICROCOPY RESOLUTION TEST CHART

REPORT R-824 SEPTEMBER, 1978 DOE/ET/EG 78-2217

CSL COORDINATED SCIENCE LABORATORY

LEVEL II

STUDIES OF HIGH-DOSE ION IMPLANTATION IN SILICON

MON YEN TSAI

UNIVERSITY OF ILLINOIS - URBANA, ILLINOIS

UNCLASSIFIED

SECURITY CLASSIFICATION OF THIS PAGE (When Data Entered)

REPORT DOCUMENTATION PAGE

READ INSTRUCTIONS BEFORE COMPLETING FORM

1. REPORT NUMBER

2. GOVT ACCESSION NO.

3. RECIPIENT'S CATALOG NUMBER

4. TITLE (and Subtitle)

STUDIES OF HIGH-DOSE ION IMPLANTATION IN SILICON.

5. TYPE OF REPORT & PERIOD COVERED

Technical Report

6. PERFORMING ORG. REPORT NUMBER

R-824, UILU-ENG-78-2217

7. AUTHOR(s)

Mon Yen Tsai

8. CONTRACT OR GRANT NUMBER(s)

DAAB-07-72-C-0259
NSF-DMR-77-22228

9. PERFORMING ORGANIZATION NAME AND ADDRESS

Coordinated Science Laboratory
University of Illinois at Urbana-Champaign
Urbana, Illinois 61801

10. PROGRAM ELEMENT, PROJECT, TASK AREA & WORK UNIT NUMBERS

11. CONTROLLING OFFICE NAME AND ADDRESS

Joint Services Electronics Program

12. REPORT DATE

September, 1978

13. NUMBER OF PAGES

135

14. MONITORING AGENCY NAME & ADDRESS (if different from Controlling Office)

9 Doctoral thesis,

15. SECURITY CLASS. (of this report)

UNCLASSIFIED

15a. DECLASSIFICATION/DOWNGRADING SCHEDULE

16. DISTRIBUTION STATEMENT (of this Report)

12 145p.

Approved for public release; distribution unlimited

DDC RECEIVED JUN 12 1979 C

17. DISTRIBUTION STATEMENT (of the abstract entered in Block 20, if different from Report)

18. SUPPLEMENTARY NOTES

19. KEY WORDS (Continue on reverse side if necessary and identify by block number)

High-Dose Ion Implantation in Silicon
Recrystallization of Implanted Amorphous Silicon

20. ABSTRACT (Continue on reverse side if necessary and identify by block number)

Properties of high-dose BF_2^+, $Si^+ + B^+$, and Ga^+ implanted Si are studied by differential resistivity and Hall effect measurements, secondary ion mass spectrometry (SIMS), deep-level transient spectroscopy (DLTS), and Auger electron spectroscopy (AES).

DD FORM 1 JAN 73 1473 EDITION OF 1 NOV 65 IS OBSOLETE

097 700

UNCLASSIFIED

SECURITY CLASSIFICATION OF THIS PAGE (When Data Entered)

STUDIES OF HIGH-DOSE ION IMPLANTATION IN SILICON

BY

MON YEN TSAI

B.S., National Taiwan University, 1972
M.S., University of Illinois, 1975

THESIS

Submitted in partial fulfillment of the requirements
for the degree of Doctor of Philosophy in Electrical Engineering
in the Graduate College of the
University of Illinois at Urbana-Champaign, 1978

Thesis Advisor: B. G. Streetman

Urbana, Illinois

UILU-ENG 78-2217

STUDIES OF HIGH-DOSE ION IMPLANTATION IN SILICON

by

Mon Yen Tsai

This work was supported in part by the Joint Services Electronics Program (U.S. Army, U.S. Navy and U.S. Air Force) under Contract DAAB-07-72-C-0259 and in part by the National Science Foundation under Grant NSF DMR 77-22228.

STUDIES OF HIGH-DOSE ION IMPLANTATION IN SILICON

Mon Yen Tsai, Ph.D.
Coordinated Science Laboratory and
Department of Electrical Engineering
University of Illinois at Urbana-Champaign, 1978

Properties of high-dose BF_2^+, $Si^+ + B^+$, and Ga^+ implanted Si are studied by differential resistivity and Hall effect measurements, secondary ion mass spectrometry (SIMS), deep-level transient spectroscopy (DLTS), and Auger electron spectroscopy (AES).

After high-dose implantation ($\geq 10^{15} cm^{-2}$), a continuous amorphous Si layer is formed on the surface. Immediately below this amorphous region is a damaged crystalline Si region. These two layers dominate the annealing behavior of the implanted Si. By comparing the atomic profile (from SIMS) with acceptor concentration profiles (from differential Hall effect measurements), it is found that $\sim$ 100% activation of boron and gallium in the amorphized layer can be achieved by recrystallization at 550-600°C. The maximum acceptor concentration for implanted boron is limited by the B solid solubility in Si. In contrast, implanted gallium can be activated beyond its solid solubility. Lower mobility, however, is observed in this oversaturated layer, and the electrical activation diminishes to the solubility limit after 900°C annealing. An inactive tail, located just below the originally amorphized region is detected in both BF_2^+ and Ga^+-implanted Si. This inactive region is attributed to the existence of unannealed damage in the crystalline Si at 550-600°C.

Fluorine and gallium redistribution after annealing BF_2^+ or Ga^+-implanted Si is examined by SIMS. The redistribution is apparently

influenced by ion-damage. Inside the recrystallized region, rather normal diffusion is seen for both F and Ga. However, the underlying damaged crystalline Si getters fluorine up to 900°C. This same layer also enhances the diffusivity of Ga to a decade higher than that in normal crystal Si. The Ga or F impurity migrates differently in these two layers causing the commonly observed anomalous diffusion for F and Ga in high-dose implanted Si.

The residual damage in BF_2^+ or Ga^+ implanted silicon is investigated by DLTS. Considerable damage is detected in the region close to the amorphous-crystalline interface in each case. This agrees with our observation of inactive tails in this region. A thick pre-amorphized layer by Si^+ implants is used to move the damaged crystalline Si away from the p-n junction region. A fully activated B profile results from recrystallization of such a region at 550°C.

Surface contamination induced by high-dose implantation is studied by AES. Carbonaceous surface contamination layers up to ~ 100Å thick are observed. Such layers inhibit etching and interfere with ohmic contact formation. No simple methods are found to remove the layer without stripping a thin Si surface layer. However, by using perfluorinated polyether diffusion pump oil in the implanter target chamber vacuum system, we find the contamination layer can be effectively eliminated.

ACKNOWLEDGMENTS

The author wishes to express his deepest appreciation to Professor B. G. Streetmen for his encouragement, guidance, inspiration and support that made this work possible.

He is greatly indebted to the Surface Analysis Group at Materials Research Laboratory for their time and efforts in this work, especially to Dr. C. A. Evans, Jr. for his support and advice; to Dr. P. Williams and Dr. V. R. Deline for the SIMS measurements, and to Mr. R. J. Blattner for the Auger electron spectroscopy analysis.

The author is grateful to Professor G. E. Anner, and Professor G. E. Stillman of Department of Electrical Engineering in this university, Dr. D. V. Lang of Bell Laboratories, Dr. H. W. Conru of IBM, and Dr. T. W. Sigmon of Oregon State University for their inspiring discussions and kindly help.

He greatly appreciates the assistance and friendship of his colleagues D. S. Day, M. J. Helix, K. J. Soda, Dr. W. V. McLevige, Dr. P. K. Chatterjee, Dr. D. R. Myers, Dr. K. V. Vaidyanathan, D. J. Wolford, G. T. Marcyk, T. H. Yu, S. S. Chan, J. D. Oberstar, and B. S. Seymour. He also thanks the many members of the professional staff of Coordinated Science Laboratory for their invaluable help throughout the course of this work.

The author also wishes to express his deepest gratitude to his wife Kelly, for her love, encouragement and concern. Above all, the author wants to thank God, the best friend of all mankind. His daily guidance and strength are the greatest blessing experienced throughout this work. As said in Psalm 111:

For reverence of the Lord is the beginning of wisdom. There is insight in all who observe it. His praise is everlasting.

TABLE OF CONTENTS

1. INTRODUCTION

After extensive studies of ion-implantation in semiconductors over the last decade [1-7], implantation has been accepted as one of the most important techniques for device fabrication as well as for semiconductor research. In microelectronic device processing, ion-implantation as a doping technique [8,9] has many advantages over thermal diffusion, including more accurate doping control, better lateral definition, lower temperature processing, and greater reproducibility. These make implantation especially compatible with other newly developing techniques, such as electron-beam [10,11] or x-ray [12,13] lithography, plasma [14,15] or reactive ion [16] etching, etc., for fabricating future high density microelectronic circuits and very-large-scale-integration (VLSI) devices [17].

Until recently, ion-implantation has been most commonly used for low-dose (10^{11} - 10^{12} cm^{-2}) or medium-dose (10^{13} - 10^{14} cm^{-2}) applications. The most important low-dose applications are threshold-voltage adjustment in MOS transistors [18,19], or potential well formation in charge-coupled devices [20]. Medium dose applications include self-alignment techniques for MOS devices [21,22] and implantation for predepositions prior to diffusion. Most heavily doped regions in silicon devices, such as emitters, contact regions, and buried collectors in bipolar circuits, and source and drain regions in MOS circuits, are commonly doped by conventional thermal diffusion methods [22]. To meet the requirements of geometrical tolerance expected in future device technology, however, thermal diffusion is likely to be replaced by high-dose (10^{15} - 10^{16} cm^{-2}) implantation. Since high-dose implants in Si are very different from lower-dose cases, extensive studies are needed before these applications can be fully

implemented [24].

One of the distinguishing characteristics of high-dose implanted Si is the formation of a continuous amorphous layer at the surface during implantation. Since these continuous amorphous layers play important roles during annealing, the crystal reordering of these layers recently has been studied by aligned backscattering methods [25,26] and transmission electron microscopy (TEM) [27,28]. Our studies of high-dose implanted Si deal mainly with electrical properties of recrystallized Si, impurity migration during annealing, and surface contamination induced by the high-dose implantation. These studies are directly related to problems encountered in the device applications of high-dose implantation.

In this work, two different models [29,30] are used to compute the critical doses for implanted amorphous Si formation. An experimental method is developed to detect amorphous Si and to measure its thickness. Amorphous Si layers are formed by BF_2^+, Si^+, or Ga^+ implants and the electrical properties of the recrystallized Si are studied by differential resistivity and Hall effect measurements. The electrically active residual damage after annealing is examined by deep-level transient spectroscopy (DLTS). Secondary ion mass spectrometry (SIMS) is utilized for studying the anomalous redistribution of fluorine and gallium during annealing. Auger electron spectroscopy (AES) is used for investigating the surface contamination produced by high-dose implantation. It is shown that decreasing the hydrocarbon level in the target chamber during implantation greatly reduces this surface contamination.

2. EXPERIMENTAL PROCEDURES

2.1. Implantation

Ion implantation is now a widely used technique of doping semiconductors, and has been reviewed extensively in the literature [1,2]. Basically, the implantation process consists of forming a plasma containing the desired ions, accelerating the ions to a high energy, selecting the desired ions by mass separation, and then directing the ion beam uniformly onto a substrate. A schematic diagram of the 300 keV Accelerators, Inc. 300-MP ion-implantor used in this work is shown in Fig. 2.1. To avoid channeling effects, all the substrates were tilted 7^{o} from the incident beam. Some special techniques applied in this work are described below:

2.1.1. Generation of Ions

The ions used in this work are $^{11}B^{+}$, $^{19}F^{+}$, $^{11}B^{19}F_2^{+}$, $^{28}Si^{+}$, and $^{69}Ga^{+}$. Except for $^{69}Ga^{+}$, all the ions are generated in a cold cathode [31] from gas source. $BF_{3(g)}$ was used to generate $^{11}B^{+}$, $^{19}F^{+}$, and $^{11}B^{19}F_2^{+}$ ions. $^{28}Si^{+}$ was extracted from $SiF_{4(g)}$ plasma in the cold cathode. $SiH_{4(g)}$ was found to be inferior to $SiF_{4(g)}$ in generating $^{28}Si^{+}$, because the hot filament source [31] is required for $SiH_{4(g)}$. The hot filament cathode induces much more $^{14}N_2^{+}$ than does the cold cathode from the residual air, and $^{14}N_2^{+}$ is an unseparable contamination for the $^{28}Si^{+}$ beam. In SIMS measurements on our samples implanted with $^{28}Si^{+}$ from the cold cathode, no nitrogen was detected within the sensitivity of SIMS. Therefore, less than 10% N_2^{+} contamination in the $^{28}Si^{+}$ beam is assured [32].

$^{69}Ga^{+}$ was obtained from $GaF_{3(s)}$ in powder form in a hot filament cathode. A vapor of $GaF_{3(g)}$ was induced by heat, and was then ionized by a discharge induced with a hot filament.

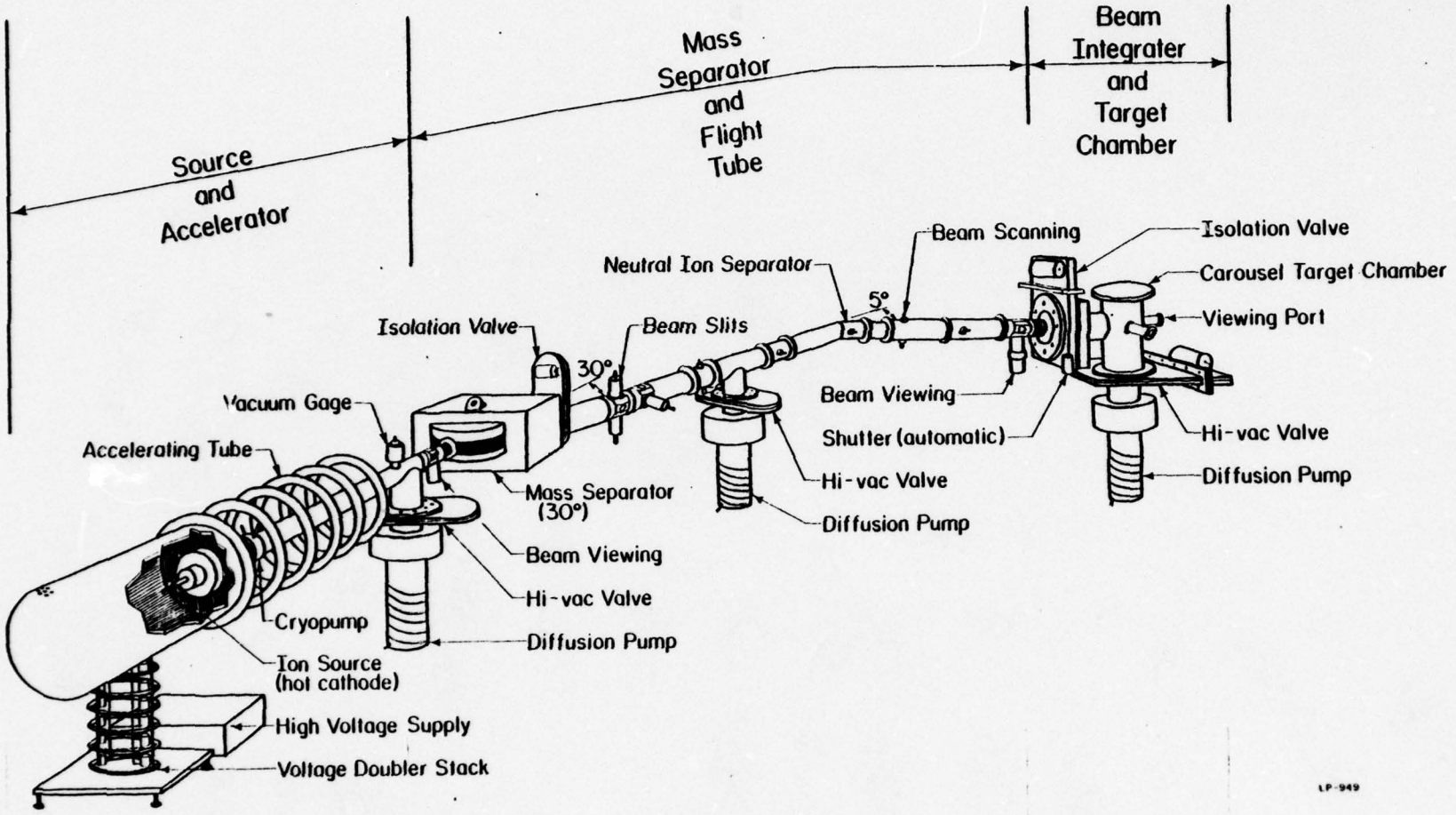

Fig. 2.1. Schematic diagram of the ion implantation system.

2.1.2. Implantation Temperature

Substrate temperature during implantation has substantial effect on the removing of damage during annealing [26]. To achieve better temperature uniformity and heat sinking, Si wafers were attached to a copper plate by silver paint (from Micro-Circuits Co., New Buffalo, Michigan) for room temperature implants. A liquid nitrogen cooled heat sink was used for low temperature implants. In both cases, the actual wafer temperature was monitored by a thermocouple held against the sample.

2.1.3. Range Statistics

A theory describing energy loss and angular deviation of particles during implantation has been developed by Linhard, Scharff and Schiott (LSS) [33]. For the first order approximation, the impurity distribution N(x) is

$$N(x) = \frac{\phi}{\sigma_p\sqrt{2\pi}} \exp\left[- \frac{(x-R_p)^2}{2\sigma_p^2} \right] \qquad (2.1)$$

where ϕ is the ion fluence, R_p is the projected ion range, σ_p is standard deviation in projected range, and N(x) is the implanted impurity concentration as a function of depth. A computer program [34] was used to perform the LSS calculations for ^{19}F in Si, and values of the projected range, standard deviation, and stopping powers are tabulated in Appendix 1. For all the other ions, a tabulated collection of range statistics by Gibbons, Johnson, and Mylroie [35] was used to predict the projected ranges before implantation. These tables include electronic cross sections estimated by Eisen [36] and also appropriate corrections for light ions [37].

These values are generally more accurate than LSS calculation alone, except for ^{19}F in Si [38]. Atomic profiles after implantation were measured in most cases by secondary ion mass spectrometry (SIMS), as discussed in Section 2.5.

The range statistics for molecular ion (BF_2^+) implants were predicted by assuming that the BF_2 molecule splits into its components with energies apportioned by mass ratio [39]. For example, a 150 keV BF_2 molecule results in two ^{19}F with 58 keV and one ^{11}B with 34 keV in the Si sample.

2.2. Annealing

Isothermal and isochronal anneals were performed in furnaces having silica liners, with a continuous flow of forming gas. For temperatures $\leq 900^{\circ}C$, a 24" Trans Temp furnace was used. For higher temperatures, a furnace with a ceramic tube was used. The sample temperature was monitored by a chromel-alumel thermocouple and a Fluke 2100A digital thermometer.

2.3. Differential Resistivity and Hall Effect Measurements

A common method of profiling implanted layers in semiconductors is the use of chemical etching or anodic oxidation and stripping of successive layers in conjunction with differential resistivity and Hall effect measurements [40,41]. Since our studies concern mainly high-dose implanted Si, this method is especially suitable to measure carrier concentration profiles.

2.3.1. Double ac Hall Apparatus

Differential resistivity and Hall effect measurements were performed with a double ac Hall effect apparatus. The block diagram is shown in Fig. 2.2. A sample current frequency (f_1) of 1 kHz and magnet current frequency (f_2) of 250 Hz are chosen to give a wide frequency separation for proper noise suppression by the lock-in amplifier. The Hall voltage is detected at the difference frequency (f_1-f_2) of 750 Hz. The sample holder, shown in Fig. 2.3, fits inside a solenoidal magnet. The Hall voltage is measured as difference between the observed voltages with the sample in and out of the magnet. Details of this system have been discussed elsewhere [42,43].

The advantages of this system is the use of phase sensitive lock-in detection at the hetrodyne frequency. This results in excellent sensitivity and noise rejection. Furthermore, Hall measurements using the standard dc technique are hampered by various thermoelectric and misalignment effects which must be canceled out by permutation of field and current. With the double ac method this permutation is accomplished automatically, so that only a single measurement of Hall voltage is required. This greatly facilitates the profiling of implanted layers in silicon, in which many successive Hall effect measurements must be made.

2.3.2. Processing of the Samples.

After annealing, samples ~ 120 mils square were defined photolithographically in a van der Pauw geometry [44] as shown in the inset of Fig. 2.3. Electrical contacts ~ 20 mils square were formed by evaporating Au through a shadow mask and then sintered at 300°C in flowing H_2 for 15 sec. The central measured area of the resulting sample was ~ 25 mils square.

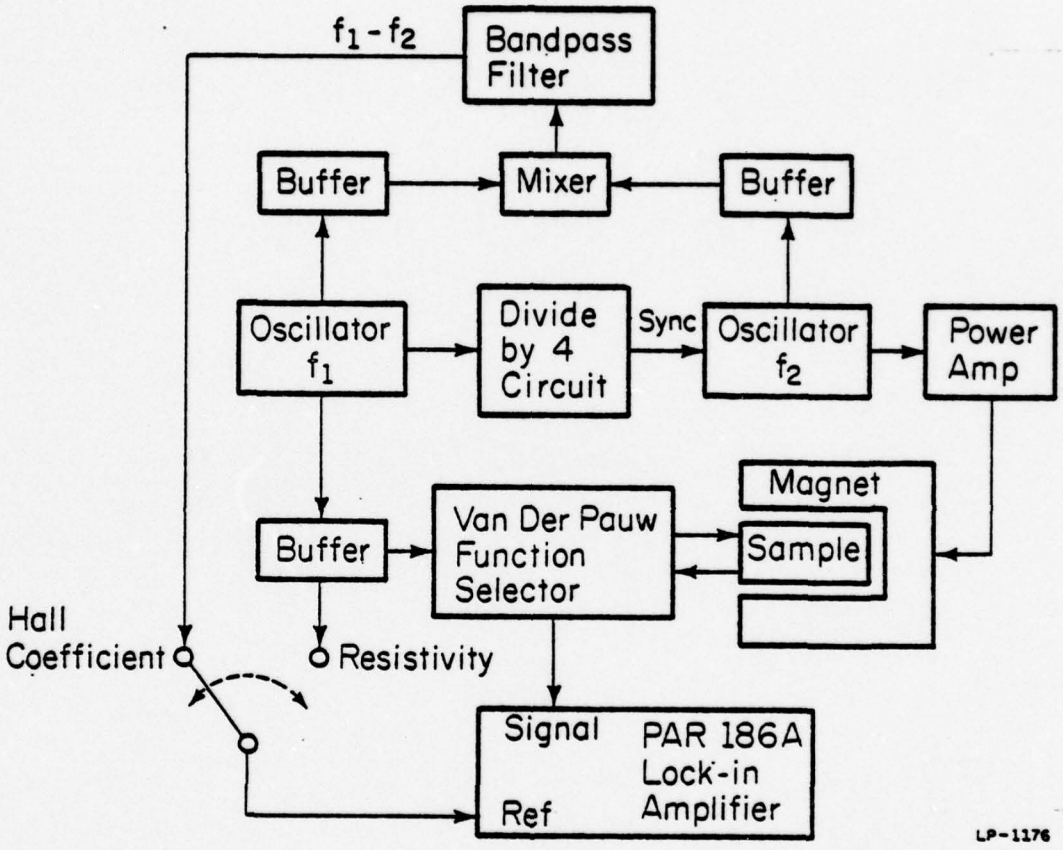

Fig. 2.2. Block diagram of double a-c Hall effect system (after McLevige *et al.* [42]).

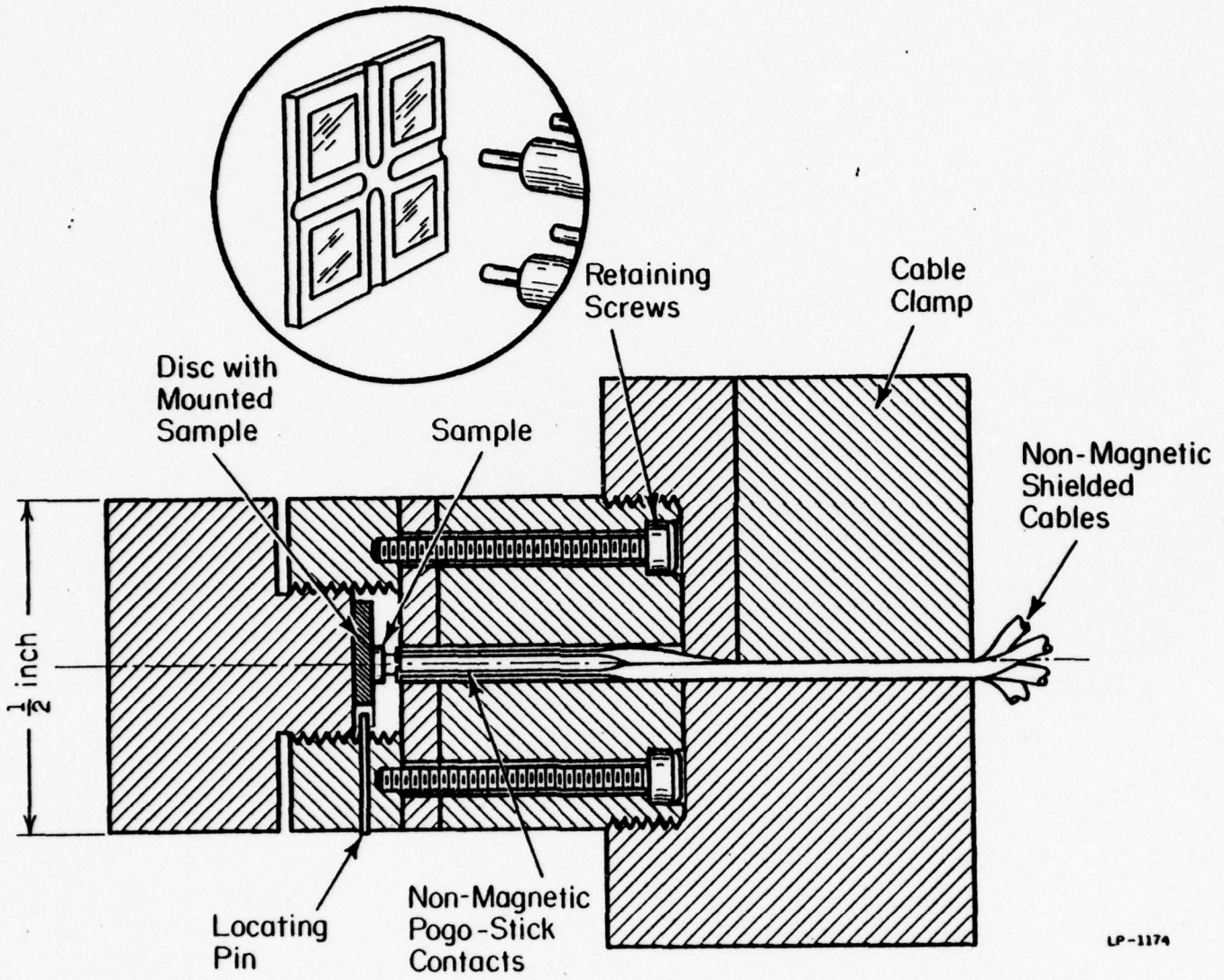

Fig. 2.3. Cross-sectional view of the sample holder used for double a-c Hall effect measurements. The inset shows the sample configuration and the spring-loaded contacts in the holder (after McLevige et al.) [42].

Samples exhibiting good p-n junction characteristics were then separated by cleaving and mounted on 325 mil diameter nylon discs with GE7031 varnish.

Successive layer removal of Si was accomplished using a slow Si planar etch consisting of 1: 750 : 250 by volume HF : HNO_3 : HCH_2COOH. A fairly constant etch rate of ~ 300Å/min was observed. Since this Si etch did not attack Au appreciably, no protection of the contacts during etching was necessary. To minimize uncertainty due to variation in the etch rate, etched step heights were measured periodically during the experiment. Apiezon W (black wax) dots of ~ 1 mm diameter were placed about the periphery of the sample to be used in determining etch depths at various points in the etching cycle. The resulting etched step height under such a masked area was measured every 600-800Å of the etching cycle, using a Sloan Dektak mechanical stylus.

2.3.3. Data Analysis

For double ac van der Pauw measurements, the sheet resistivity ρ_s and sheet Hall coefficient R_s are given by

$$\rho_s = \frac{\pi}{\ln 2} \frac{V_{ABCD} + V_{BCDA}}{2I} f\left(\frac{V_{ABCD}}{V_{BCDA}}\right) \tag{2.2}$$

and

$$R_s = \frac{\sqrt{2}\ \Delta V_{BDAC(rms)}}{B\ (rms)\ I(rms)} \tag{2.3}$$

With the four contacts labeled consecutively, V_{ABCD} represents the voltage between contacts A and B with current I passed between C and D. The symbols V_{BCDA} and ΔV_{BDAC} are defined similarly, with ΔV_{BDAC} the Hall voltage in a

magnetic field B. The correction factor $f\left(\frac{V_{ABCD}}{V_{BCDA}}\right)$ has been tabulated by van der Paw [44].

The interpretation of differential resistivity and Hall effect measurements in determining the electrically active carrier distribution has been thoroughly discussed elsewhere [40,45]. The sheet resistivities before and after stripping a layer of thickness d_j after step j in the etching cycle are denoted by ρ_{s_j} and $\rho_{s_{j-1}}$, respectively. Similarly, R_{s_j} and $R_{s_{j-1}}$ are used for the sheet Hall coefficients. Then the average mobility μ_j of the jth layer can be shown [40] that

$$\gamma \mu_j = \mu_{H_j} = \frac{R_{s_j}}{\rho_{s_j}} + \frac{R_{s_{j-1}}}{\rho_{s_{j-1}}} - \frac{R_{s_{j-1}} - R_{s_j}}{\rho_{s_{j-1}} - \rho_{s_j}} \tag{2.4}$$

where γ is the ratio of Hall mobility to conductivity mobility. The average carrier concentration is given by

$$n_j = \frac{\frac{1}{\rho_{s_j}} - \frac{1}{\rho_{s_{j-1}}}}{ed_j\mu_j} \tag{2.5}$$

In the case of high-dose implanted silicon, the ratio (γ) of Hall mobility (μ_{H_j}) to conductivity mobility (μ_j) has been taken to be 0.73 for high concentration p-regions [46]. The computer programs used for this analysis are given in Appendix 2. All electrical profiles were measured on several identically processed samples, and the variation between measurements was within the system error and is shown on the figures of measured profiles.

2.4. Differential Capacitance and Voltage (C-V) Measurements

Differential capacitance-voltage measurements on Schottky barriers or p-n abrupt junctions have traditionally been used to determine the impurity profile on the lightly doped side of the junction [47]. A versatile C and dC/dV measurement system based on phase sensitive lock-in detection and secondary harmonic principles was constructed for profiling samples with low-dose implantion or low percentage of activation.

2.4.1. Experimental Apparatus

The block diagram of the secondary harmonic C-V system used in this work is shown in Fig. 2.4. Through a calculation shown in Appendix 3, the small signal for the diode current has a first order term, which is proportional to the capacitance of the diode, and a second order term, which is proportional to $\frac{dC}{dV}$. The phase sensitive lock-in amplifier can be made to detect C or $\frac{dC}{dV}$, by adjusting the phase and the reference frequency. Figure 2.5 shows typical plots of C and dC/dV vs. bias voltage. Through a computer calculation, also shown in Appendix 3, the carrier concentration N(x) at a depth x can calculated from C and dC/dV that is, below the surface,

$$N(x) = \frac{C^3}{\epsilon q A(-dC/dV)}, \quad x = \epsilon A/C(V),$$

where A is the area of the junction and ϵ is the electrical permittivity of Si.

2.4.2. Application of the C-V Measurement

Recent work [48-50] has demonstrated that the zero Debye length approximation commonly used in C-V analysis is not strictly valid and

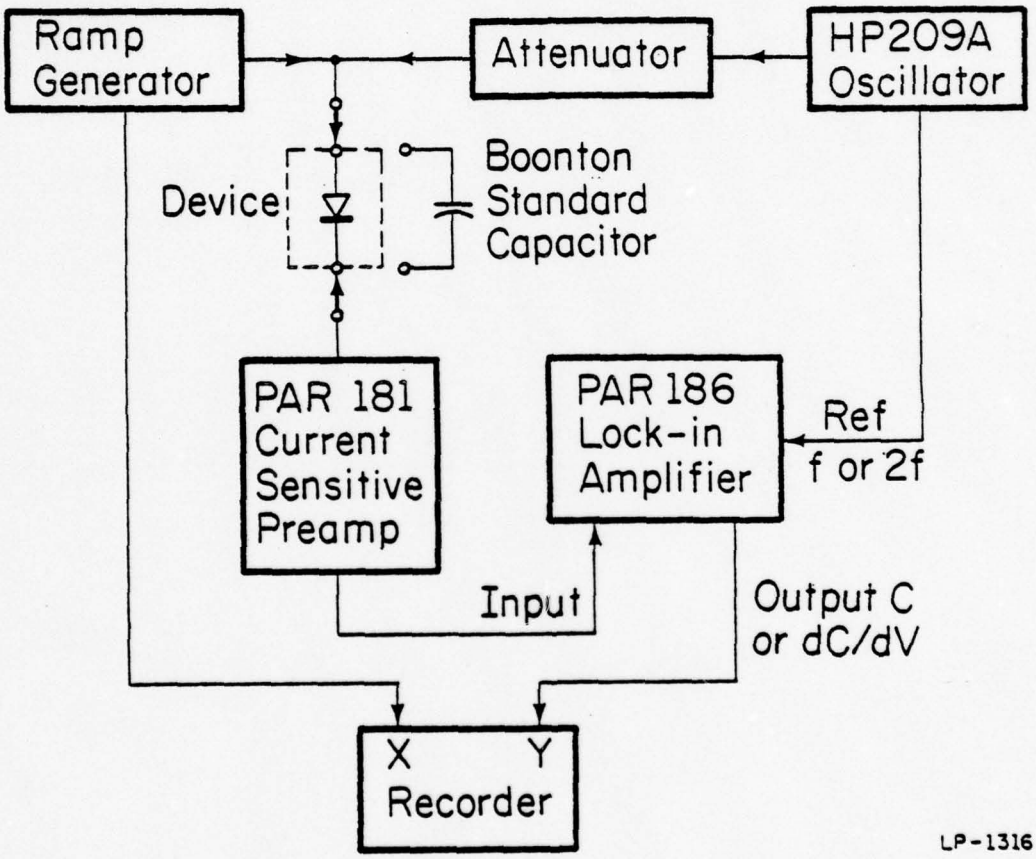

Fig. 2.4. Block diagram of second harmonic C-V and $\frac{dC}{dV}$ system.

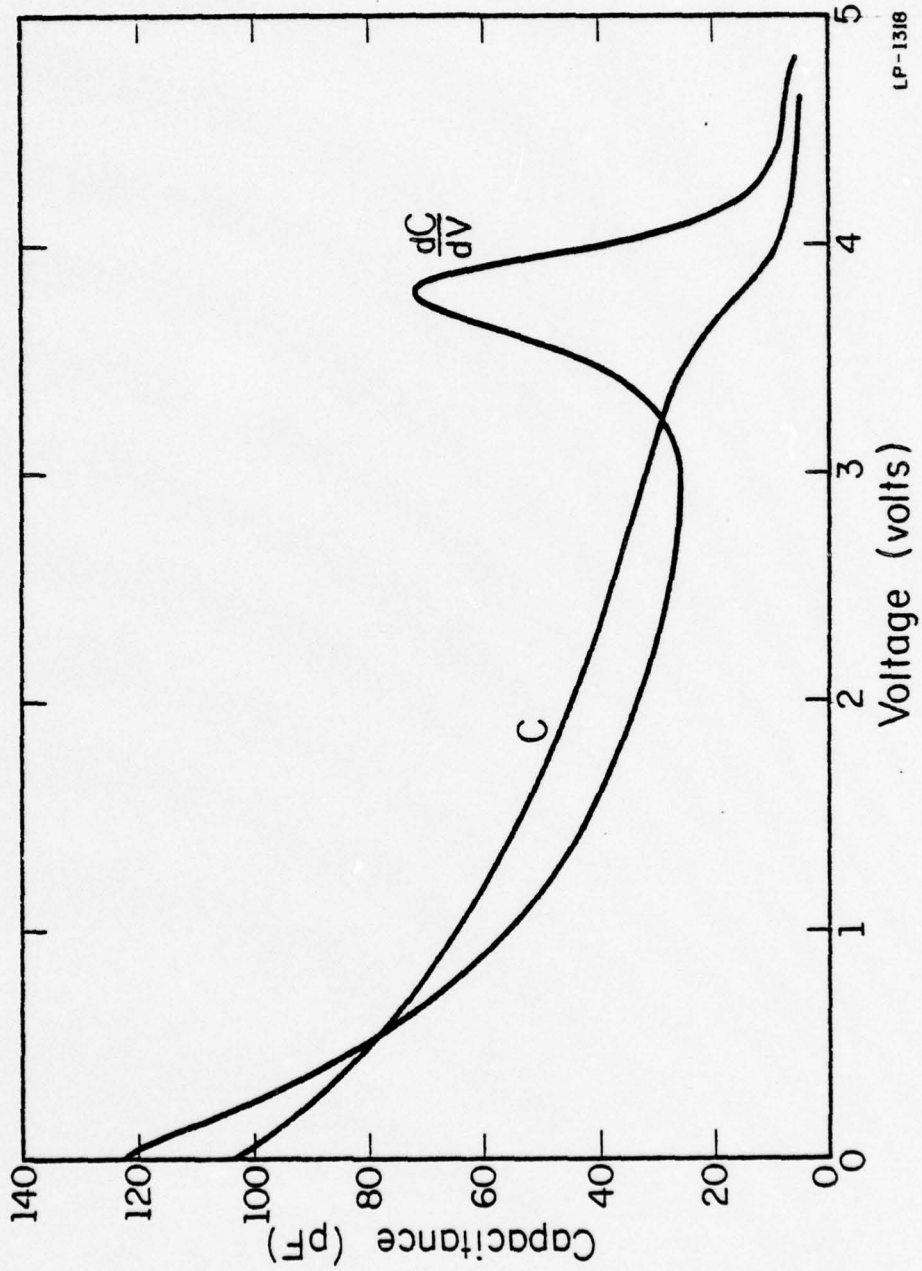

Fig. 2.5. Typical data of C and $\frac{dC}{dV}$ for a varactor (Appendix 4) taken by the second harmonic system.

that the resolution of the measurement is restricted to several Debye lengths. It has also been shown [51] that the presence of sharp impurity gradients in implanted layers makes it extremely difficult to obtain accurate impurity distributions from capacitance data. However, the C-V technique is a nondestructive method which can be used for a quick check of low-concentration electrically active centers.

Most C-V measurements used in this work employed Schottky diodes, formed by evaporating circular Al or Au dots on the Si surface. Using the system shown in Fig. 2.5, C and dC/dV curves were plotted on an X-Y recorder. Then the concentration profile was calculated from these data as described in Appendix 3. This method was used to check the electrical activation of fluorine (Chapter 4) and the carrier concentration distribution of varactors (Appendix 4).

2.5. Atomic Profiling

The boron, fluorine and gallium atomic profiles presented in this work were measured by secondary ion mass spectrometry (SIMS) [52,53] using an AEI-IM20 ion microprobe [54] located in the Materials Research Laboratory. In this measurement technique, the focused primary ion beam (Cs^+, O_2^+) is rastered across the sample surface to erode a square, flat-bottom crater having a maximum size of 256 μm square. The sputtered atoms which are ionized (i.e. secondary ions) are extracted and pass through a mass analyzer. An electronic aperture technique is used to ensure that mass analyzed secondary ions are counted only if they were sputtered from the central 10% of the rastered area, thereby largely eliminating ions sputtered from the crater walls.

Under well-controlled conditions, the ion counts are linearly proportional to the atomic concentration of the investigated species in the sample. This linearity was verified by comparing ion counts for samples which had been implanted with BF_2^+ doses over the range 10^{13} - 10^{15} cm^{-2}. The conversion from ion count ratio to atomic concentration was made by determining the ratio of the integrated ion counts to the implanted ion dose for an as-implanted sample. This conversion ratio was then used to obtain the atomic concentration profiles for samples after annealing. Crater depths were measured using the interference microscope to establish a depth scale.

The secondary $^{30}Si^-$ counts were monitored on some samples while the crater was eroded; these counts were essentially constant except very near the surface (100-200Å). Thus the sputtering rate was constant during SIMS measurement within the bulk of the sample. Since we are only interested in the atomic profile within the bulk, we will not deal with the data from the near-surface region in this work.

2.6. Auger Electron Spectroscopy (AES)

Auger electron spectroscopy [55] was used for studying the surface contamination produced by high-dose implantation. In this technique, a primary electron beam in the energy range of 1-10 keV bombards the sample. This primary electron beam causes a variety of secondary processes to occur, the most important of which is the creation of an atomic inner shell vacancy. This inner shell vacancy is filled by an outer shell electron, and the excess energy is carried away either by a photon or by an electron. If an electron is ejected, this radiationless transfer

of energy is known as the Auger effect and the emitted electron as an Auger electron. The energy of this ejected electron is determined by the atomic energy levels and hence is characteristic of the atom. The emitted electron will retain this characteristic energy only for emitting atoms close enough to the sample surface (20Å). Therefore, Auger spectroscopy is essentially a surface analytical technique. Depth profiles are obtained by gradually sputtering the sample surface to expose successive regions to Auger analysis.

The AES in-depth profiling in this work was performed using a custom built thin film analyser based on a Physical Electronics Industries model 10-155 cylindrical mirror analyser/coaxial 5 kV electron gun. Equipment and procedures employed have been described elsewhere [56]. Depth profiling was accomplished with 1.0 keV Ar^+ at a current density of $\sim 20\ \mu$ amp/cm^2. The ion beam was electrically rastered over the sample to flatten the crater and thereby maximize depth resolution. These conditions correspond to a sputtering rate of approximately 10Å/min in silicon. The depth can be estimated from sputtering time when reliable sputtering rate data is available, as in the case of Si.

3. FORMATION OF AMORPHOUS Si BY ION IMPLANTATION

Crystalline silicon can be transformed into amorphous Si by appropriate high-dose implantation [57]. There have been two models proposed to calculate the critical doses for this transformation: a critical-energy-density (CED) model [29,58], and a damage-overlap (DO) model [30,59]. Since amorphous layers play an important role in annealing behavior, the prediction of formation of amorphous Si is very important, as is its detection after implantation. This chapter briefly discusses these two models and estimates the critical doses for BF_2^+, Si^+, and Ga^+-implanted Si used in this work. An experimental method is developed to measure the thickness of amorphous layers on the implanted samples.

3.1 Critical-Energy-Density (CED) Model

The CED model [29,58-60] assumes that transformation to the amorphous state is due to an increase in lattice energy. This energy increase comes from the energy deposited by the implanted ions in their collisions with lattice atoms. As the implantation proceeds, the implanted energy produces an increasing collection of point defects. Once the critical energy density reached, it becomes energetically favorable for the point defects to coalesce into the tight tetrahedral structure of the amorphous state [60]. The critical energy density, E_c, is then defined as the energy which must be deposited into lattice damage per unit volume to amorphize that volume. Gibbons [59] estimated $E_c = \sim 10^{24}$ eV/cm^3 from low-temperature data of critical doses for a variety of ions. Certainly, this is only a rough estimation [61] but it can be used for certain cases.

Brice [62] has calculated the energy deposited into atomic process for a variety of dopants and target substrates. These calculations are based on a direct method in which one uses the interaction cross sections to determine the amount of energy deposited at a particular position, then sums over

the distribution. Such calculated results have been tabulated for $^{11}B^+$, $^{31}P^+$, $^{75}As^+$, and $^{121}Sb^+$ implanted into Si [62]. However, the damage profiles for $^{19}F^+$, $^{28}Si^+$, and $^{69}Ga^+$ must be obtained through approximation.

Damage by $^{28}Si^+$ and $^{69}Ga^+$ can be approximately estimated from $^{31}P^+$ and $^{75}As^+$ tables respectively, with minor modification due to mass differences. For example, the projected range R_p can easily be adjusted to the right values. However, damage profiles for $^{19}F^+$ must be interpolated from $^{11}B^+$ and $^{31}P^+$ tables. Figure 3.1 shows the energy deposition (or damage) by a fluence of 1×10^{15} cm^{-2} B^+ implanted at 34 keV and 2×10^{15} cm^{-2} F^+ at 58 keV. The damage created by $1 \times 10^{15} cm^{-2}$ BF_2^+ implanted at 150 keV can be estimated from the sum of these B^+ and F^+ implants. This is possible because a 150 keV BF_2 molecule splits into one 34 keV B and two 58 keV F (Section 2.1.3). The dotted curve in Fig. 3.1 is the sum of these B^+ and F^+ curves. However, it is well known that molecular ion implants produce much greater damage than do the corresponding atomic implants of equivalent dose and energy [63-65]. Therefore, the true energy deposition curve for a BF_2^+ implant should be much higher than the sum of B^+ and F^+ implants. A factor of $\gtrsim 1.5$ greater damage is estimated from previous work for molecular ion implantation [63]. A dash-dotted curve in Fig. 3.1 shows this corrected energy deposition curve for the BF_2^+ implant.

We can roughly predict the location and thickness of the amorphous layer from the energy density profile and critical energy density (E_c). The value given by Gibbons [59], $E_c = \sim 10^{24}$ eV/cm^3, is for low temperature implantation where all the damage produced by a projectile is stable. It was recognized very early that the critical dose increased substantially with rising implantation temperature [66,67]. Obviously, E_c should follow

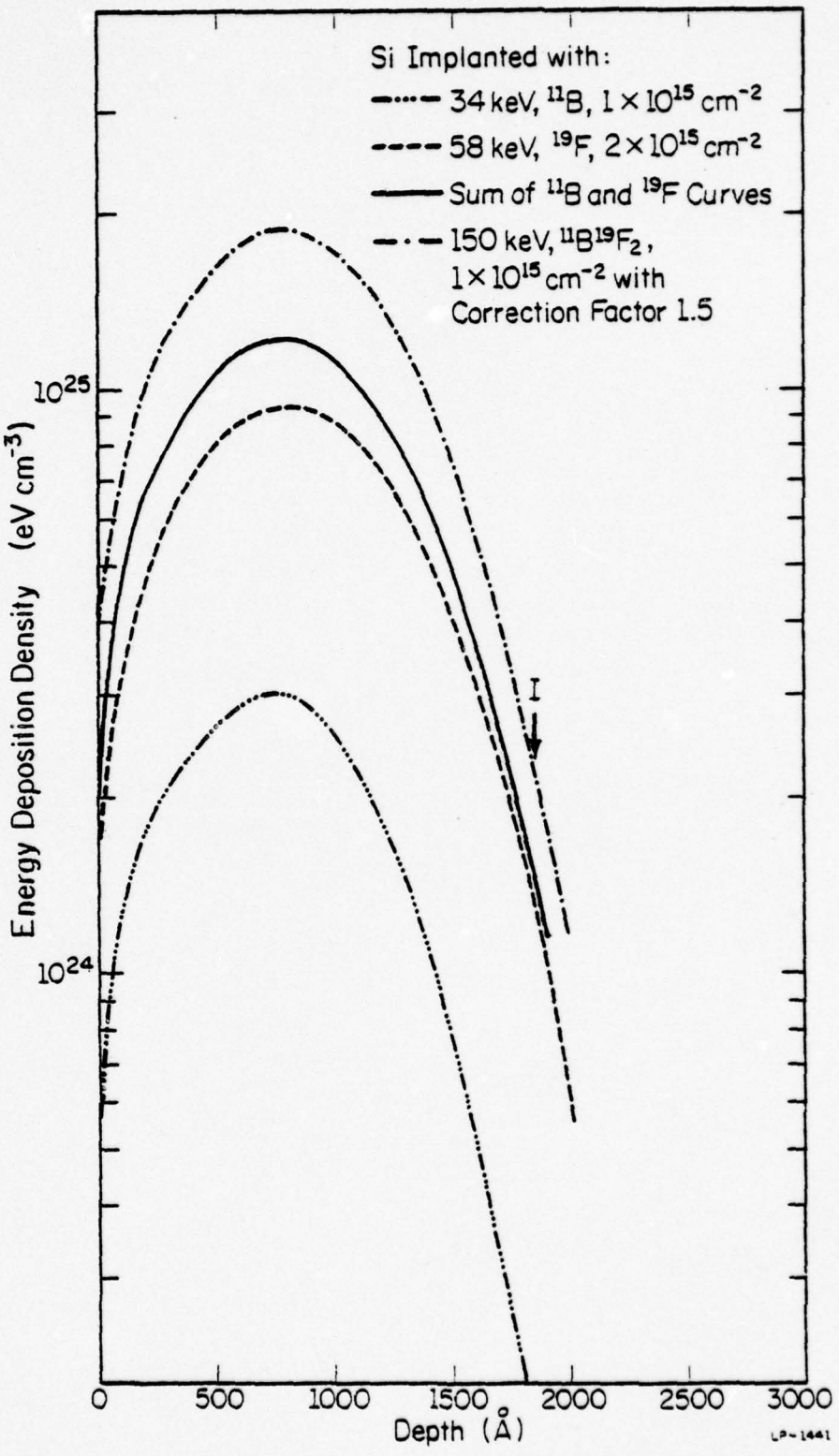

Fig. 3.1. Calculated energy deposition density for the ion implanted into Si at energies and fluences as shown. The dash-dot curve shows the energy deposition density for BF_2^+ implanted Si, which is estimated as 1.5 times the sum of B and F curves. The measured amorphous-crystalline interface is denoted by I.

the same trend in temperature dependence. However, no satisfactory model has ever been proposed to estimate the temperature dependence of E_c. Therefore, the use of this model is limited to low temperature implantation.

Even at low temperature, the validity of available prediction is limited by the accuracy of Brice's calculations and the value of E_c. From experiments described later (Section 3.3), the BF_2^+ implant shown in Fig. 3.1 has a measured amorphous layer ~1850 Å thick. From the energy deposition curve, the corresponding value of E_c is $\sim 2.2 \times 10^{24}$ eV/Cm^3, which is much higher than the E_c value predicted by Gibbons. This is also true for Si^+-implanted Si. A thick amorphous layer created by a series of 50-200 keV Si^+ implants to a total dose of 7.6×10^{15} cm^{-2} is measured to be ~3600 Å. This corresponds to $E_c \approx 10^{25}$ eV/cm^3 from the energy deposition curve (not shown). Therefore, this model can only very roughly estimate the amorphous layer thickness.

3.2 Damage-Overlap Model

As an ion comes to rest in the sample it produces silicon knock-ons which cause substantial radiation damage around the ion track. The buildup of amorphous material is due to overlapping of this damage [30]. Assume the disordered region is a cylinder with radius R_0 around the ion path at low temperature (no vacancy-diffusion). The dose $D_0 (\propto R_0^{-2})$ required to yield an amorphous layer in the absence of vacancy outdiffusion can be estimated by assuming that all of the target atoms must be displaced to produce an amorphous layer. This critical dose is [30]

$$D_0 = \bar{E}\, n_2 (dE/dx)_0^{-1} \text{cm}^{-2} , \qquad (3.1)$$

where $\bar{E}$ is the effective energy to displace a target lattice atom in eV. n_2 is the number of target atoms per cm^3, and $(dE/dx)_0$ is the energy-independent nuclear energy loss per unit path length. The latter quantity can be quickly estimated for practical purposes from an approximation [1] to the Nielson equation

$$(dE/dx)_0 \cong 7 \times 10^8 g_2 \, Z_1^{2/3} M_1 (M_1 + M_2)^{-1} \text{ eV cm}^{-1} \qquad (3.2)$$

Here Z_1, Z_2, M_1, M_2 are the atomic numbers and masses of the projectile and target, respectively and g_2 is the target density in gm/cm^3. $\bar{E}$ is taken here as roughly twice the estimate of the threshold energy required to break all bonds, i.e., for Si, $\bar{E} \tilde{=} 25$ eV.

Using this formula we can calculate the critical doses for $^{11}B^+$, $^{11}B^{19}F_2^+$, $^{28}Si^+$, and $^{69}Ga^+$ for samples implanted at low temperature where vacancy diffusion can be neglected. The $(dE/dx)_0$ for $^{11}B^{19}F_2$ is obtained by adding the values for ^{11}B and ^{19}F. The resulting values for D_0 are listed in Table 3.1. D_0 for ^{31}P and ^{75}As calculated by Morehead and Crowder [30] are also listed for comparison.

The temperature dependence of the critical dose can be accounted for through the concept of vacancy out-diffusion [30]. If the substrate temperature is not low enough ($\gtrsim$ -100°C), various atomic rearrangements occur, in a short time interval (τ) after the ion passes. This can be described in terms of thermal diffusion of vacancies radially outward from the core of the ion track. Therefore the low temperature (no diffusion) amorphous radius R_0 is decreased an amount δR by vacancy out-diffusion. Since the critical dose is inversely proportional to the amorphized area, the ratio of critical dose at temperature T to the low-temperature critical dose can be written

TABLE 3.1

Calculated Critical Doses for Amorphous Si Formation
Using the Damaged Overlap Model

Ion	$D_0(cm^{-2})$	$D_{300}(cm^{-2})$
^{11}B	9×10^{14}	4×10^{17}
$^{11}B^{19}F_2$	1.8×10^{14}	5.5×10^{14}
^{28}Si	2.6×10^{14}	1.1×10^{15}
$^{69}Ga^+$	1.1×10^{14}	2.5×10^{14}
$^{31}P^+$	2×10^{14}	8×10^{14}
$^{75}As^+$	1×10^{14}	2×10^{14}

$$D(T)/D_0 = R_0^2/(R_0 - \delta R)^2$$

$$= [1-(\delta R/R_0)]^{-2} \qquad (3.3)$$

The expression used for the decrease in amorphous radius δR is [30]

$$\delta R = 2(D_v \tau)^{1/2}$$

$$= 2(D_v^0 \tau \exp(-E/kT))]^{1/2} \qquad (3.4)$$

where τ is the amorphous restructuring interval and, hence, the diffusion time; D_v is the vacancy-diffusion coefficient with D_v^0; and E is the activation energy for diffusion. Therefore equation (3.3) can be written using (3.1) and (3.4)

$$D(T) = D_0[1-K(dE/dx)_0^{-1/2}\exp(-V/kT)]^{-2} \qquad (3.5)$$

with the two adjustable constants K and V, where

$$K = 2(\tau D_v^0 \bar{E} n_2)^{1/2} \qquad (3.6)$$

$$V = E/2 \quad . \qquad (3.7)$$

The available experimental data fits equation (3.5) when $K = 115\ (keV/\mu m)^{-1/2}$ and $V = 0.06$ eV are assigned [1]. By using these data, $D(300°K)$ for B^+, BF_2^+, Si^+, and Ga^+ were calculated and listed in Table 3.1 along with Morehead's values for P^+ and As^+[30].

This model neglects the non-uniformity of damage profiles and the energy dependence of damage creation. Therefore, the thickness of the amorphous layer is not defined in this model. However, with the vacancy out-diffusion concept, the temperature dependence of the critical dose for amorphous transformation can be estimated. The values listed in Table 3.1 can be used as a lower limit of amorphous Si formation.

3.3 Detection of Amorphous Si

Since both models discussed above only give a very rough estimation of the formation of amorphous Si, experimental methods are necessary to distinguish amorphous Si from disordered crystalline Si. Transmission electron microscopy [27,68], optical absorption [29], aligned backscattering [25,26], and electron spin resonance [57,69] are the most commonly used techniques. All these need fairly sophisticated equipment. A simple experimental method has been developed for this work to examine the amorphization of the implanted layers.

It is well known that crystalline Si has a negligible etch rate in hydrofluoric acid (HF). On the other hand, amorphous Si can be etched by HF [70]. Hence, the thickness of the amorphous layer after implantation can be determined from the difference in etch rate of crystalline and amorphous Si in HF. To study this difference, etched depths were measured as a function of etch time. During implantation a small portion of the sample was masked from the beam to retain an unimplanted crystalline region (Fig. 3.2). After implantation the sample was etched in 49% HF for various time intervals. Then the etch step between implanted and unimplanted regions was measured by a Sloan Dektak stylus. After the entire amorphous silicon layer was etched away, the etched step remained unchanged. For example, the etched depths of a BF_2^+-implanted sample to a fluence of 1×10^{15} cm^{-2} and a Si^+-implanted Si to a total fluence of 7.6×10^{15} cm^{-2} at -110°C are shown in Fig. 3.3. The energy deposition of these two implants have been discussed in Section 3.1. A well-defined etch rate of 33 Å/hr was found for amorphous Si, with negligible etching of crystalline material. As Fig. 3.3 indicates, the etch rate is independent of the implanted species (BF_2^+ or Si^+) used in this work. One

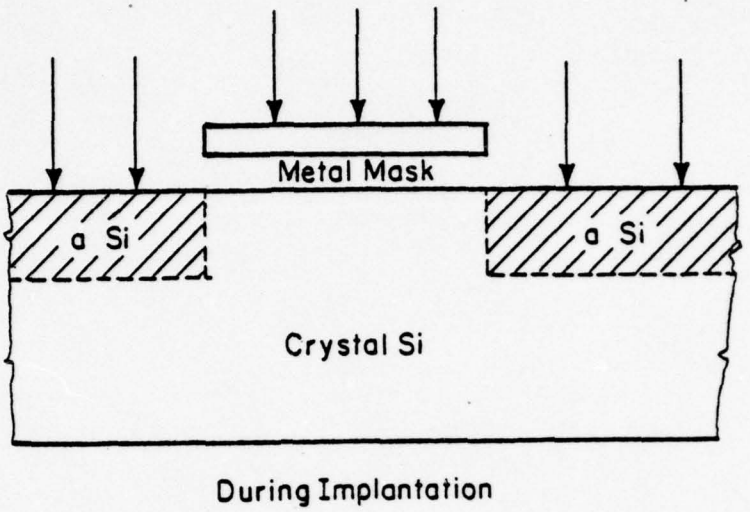

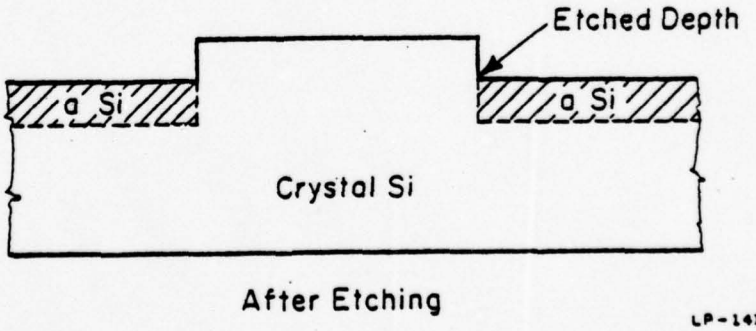

Fig. 3.2. A simple method to detect amorphous Si. During implantation, a small portion of Si crystal is masked from the ion beam. Since only amorphous Si can be etched away, the etch depth indicates the existence of amorphous Si layer and its thickness.

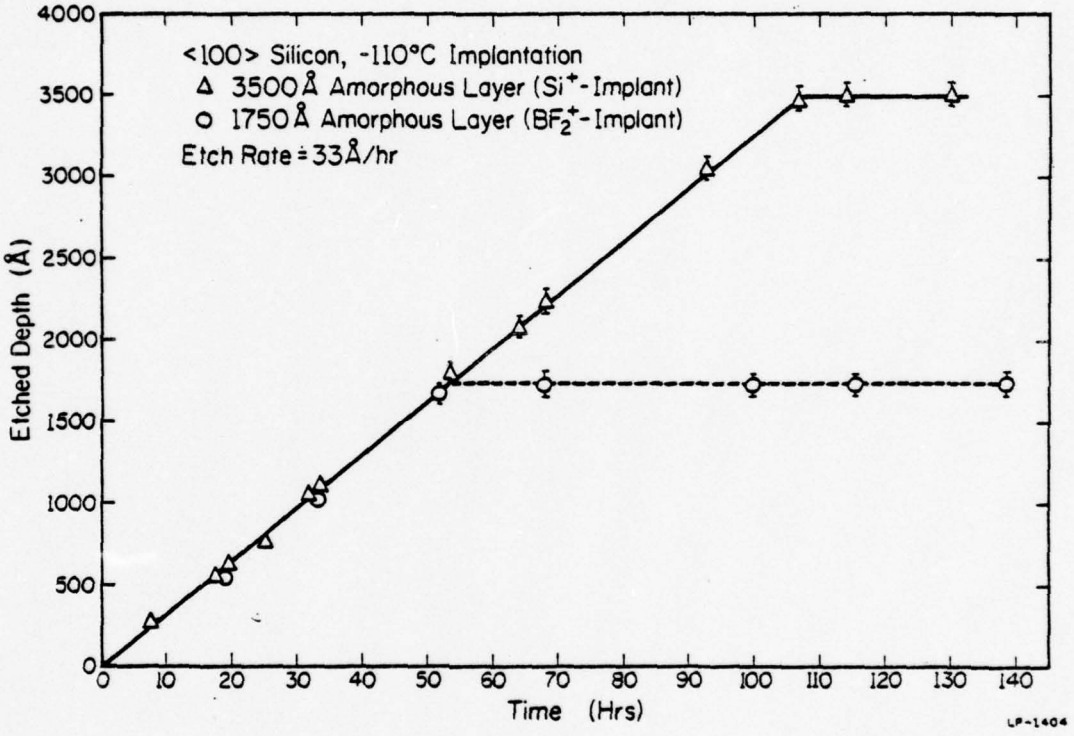

Fig. 3.3. Etched depths for amorphous Si etched in 49% HF. These amorphous layers were formed by a BF_2^+ implant or by Si^+ multiple implants. An etch rate of 33 Å/hr is found for amorphous Si.

sample was very heavily damaged but not completely amorphized, as indicated by aligned backscattering measurements [61]. This sample did not etch appreciably in HF, indicating that the etch rate difference apparent in Fig. 3.3 delineates amorphous and heavily damaged crystalline Si.

An anomalous surface layer, sometimes observed on heavily implanted samples [71,72], causes a rough etched surface, as will be shown in Chapter 6. To avoid this problem in the etching experiments, this surface layer was removed by anodic oxidation prior to chemical etching. In this process ~100 Å of the Si surface was also removed, as estimated from measurement of the anodic oxide thickness. Therefore the amorphous layers shown in Fig. 3.3 are ~100 Å thinner than the original thickness. This surface treatment was also performed on some samples used in electrical measurements (Chapter 4) after annealing. Properties of this anomalous surface layer often observed after high-dose implantation are discussed in Chapter 6.

4. ELECTRICAL PROPERTIES OF SILICON IMPLANTED WITH B^+, BF_2^+, OR $Si^+ + B^+$

As Table 3.1 indicates, after Si is implanted with a high dose ($\geq 10^{15}$ cm^{-2}) of P^+, As^+ or Ga^+ at room temperature, crystalline Si is amorphized. This has also been verified experimentally [30]. The annealing of such high-dose implanted Si layers involves primarily recrystallization of the amorphous Si (Fig. 4.1) as shown by aligned backscattering methods [25,73]. Some early work measured the carrier concentration profiles of recrystallized amorphous layers [74,75]; however, the mechanism of activation of implanted dopants inside the amorphous layer is not fully understood.

In this work, we first study B^+ or BF_2^+-implanted Si. Since B^+ is a light ion, B^+-implanted silicon is normally crystalline (the critical dose for B^+ in Si is $> 2 \times 10^{16}$ cm^{-2}) [30]. In contrast, Si implanted with BF_2^+ to a fluence $\geq 10^{15}$ cm^{-2} has a continuous amorphous layer on the surface [39]. Comparing these two cases, we can study the different mechanisms for boron activation in crystalline Si and amorphous Si. Besides the interesting annealing behavior, p^+-n junctions formed by BF_2^+ implants have been reported to have lower leakage current than for B^+ implants [76,77]. For the fabrication of shallow p-regions, BF_2^+ is easier to implant than B^+. Since the implantation energy for BF_2^+ is much higher than for B^+ to form an identical boron distribution (Section 2.1.3), larger and more stable ion beams can be obtained for BF_2^+ implants. These advantages of BF_2^+-implanted Si motivate the study of this molecular implant [78,79].

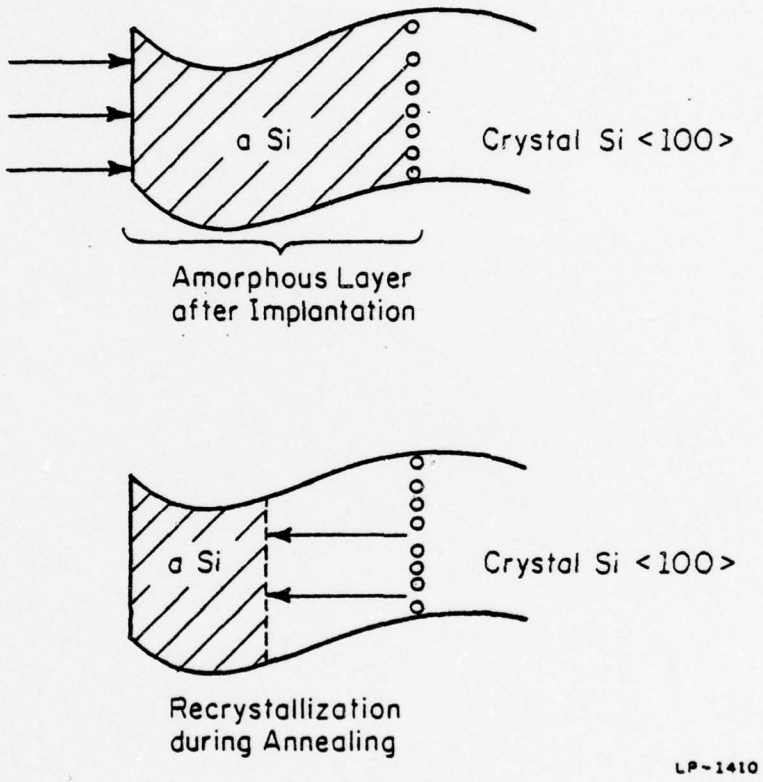

Fig. 4.1. Recrystallization of implanted amorphous Si. (L. Csepregi et al. [73])

Another method of creating amorphous layers in B^+-implanted silicon is the use of Si^+ predamaging implants before the B^+ implant. By adjusting the energies and fluences of Si^+, a continuous amorphous Si layer of desired thickness can be created.

In this study, we find that B in amorphous Si layers can be electrically activated during recrystallization at 550°C. This is not true for B^+-implanted Si, which is normally crystalline after implantation. A comparison of the atomic B distribution with electrical carrier profiles reveals an inactive tail below the originally amorphized layer for samples implanted with a 1×10^{15} cm^{-2} fluence of BF_2^+ at room temperature or at $\sim$ - 110°C. However, full activation is achieved for B^+ implanted into a thick amorphous silicon layer predamaged by Si^+ implants. The mobility is also fully recovered during recrystallization. An upper limit of carrier concentration is also found for B in Si at 550°C.

4.1. Sample Preparation and Measurements

Phosphorus-doped 4-6 Ω-cm ⟨100⟩ Si crystals were used throughout this study. The implantation schedules and temperatures, listed in Table 4.1, consisted of four categories: B^+ implants at room temperature ($\lesssim 30°$); BF_2^+ implants at room temperature; BF_2^+ implants at $\sim$ -110°C; and B^+ in addition to Si^+ implants at $\sim$ -110°C. The energies of B^+ and BF_2^+-implantations were chosen to give the same B projected range (Section 2.1.3). The implantation and annealing techniques have been discussed in Chapter 2. The thickness of the amorphous layer after implantation was determined by etching in HF (Section 3.3).

Sheet carrier concentrations were obtained from Hall effect measurements using a van der Pauw configuration. Differential resistivity

and Hall effect measurements in conjunction with successive layer removal were used to obtain the electrical carrier distributions (Section 2.3).

The boron atomic profiles for sample 2 of Table 4.1 were measured by secondary ion mass spectrometry (SIMS) with an O_2^+ source primary beam on as-implanted samples as well as on annealed samples. The measured unannealed profile agreed well with that calculated from projected range statistics [35], and no appreciable boron diffusion was found in samples annealed at 500°C or 600°C. Therefore, the assumed boron atomic profiles for samples 3, 4, and 5 were based on the measurements of sample 2.

4.2. Electrical Activation of Boron

Figure 4.2. illustrates the effects of isothermal annealing on sheet carrier concentration for samples implanted with B^+ (sample 1) or BF_2^+ (sample 2) to a fluence of 1×10^{15} cm^2. At 900°C the BF_2^+-implanted sample is almost fully activated within 2 min. The B^+-implanted sample, however, exhibits only ~ 83% electrical activation of the implanted boron even after 100 min annealing. It is clear from the 900°C curves of Fig. 4.2 that the electrical activation of boron in an amorphized sample is completely different from the damaged crystalline case. The activation of implanted boron in crystalline Si is apparently due to migration of thermally-generated vacancies to interstitial B atoms [80]. On the other hand, boron in an amorphized Si layer is activated during the recrystallization. This is evident from the 550°C annealing data. At this temperature, amorphous Si is recrystallized, regrowing epitaxially on the underlying substrate. The 550°C curve for BF_2^+-implanted Si shows the sheet carrier concentration builds up with increasing annealing time. In contrast, at this temperature B^+-implanted Si has only $\lesssim$ 7% activation. The buildup

Table 4.1. Implant sequences for various samples studied in this chapter. The implantation temperatures and crystal conditions after implantation are also listed.

Sample No.	Ion	Implant Parameters		Implant Temp.	Implanted Layer
		Energy(keV)	Dose(cm^{-2})		
1	^{11}B	34	1×10^{15}	$\lesssim 30^{o}C$	Crystalline
2	$^{11}B^{19}F_2$	150	1×10^{15}	$\lesssim 30^{o}C$	Amorphous (~1325Å)
3	$^{11}B^{19}F_2$	150	3×10^{15}	$\lesssim 30^{o}C$	Amorphous (~1850Å)
4	$^{11}B^{19}F_2$	150	1×10^{15}	$\sim -110^{o}C$	Amorphous (~1850Å)
5	^{28}Si	50	6×10^{14}	$\sim -110^{o}C$	Amorphous (~3600Å)
		100	1×10^{15}		
		150	2×10^{15}		
		200	4×10^{15}		
	^{11}B	34	1×10^{15}		

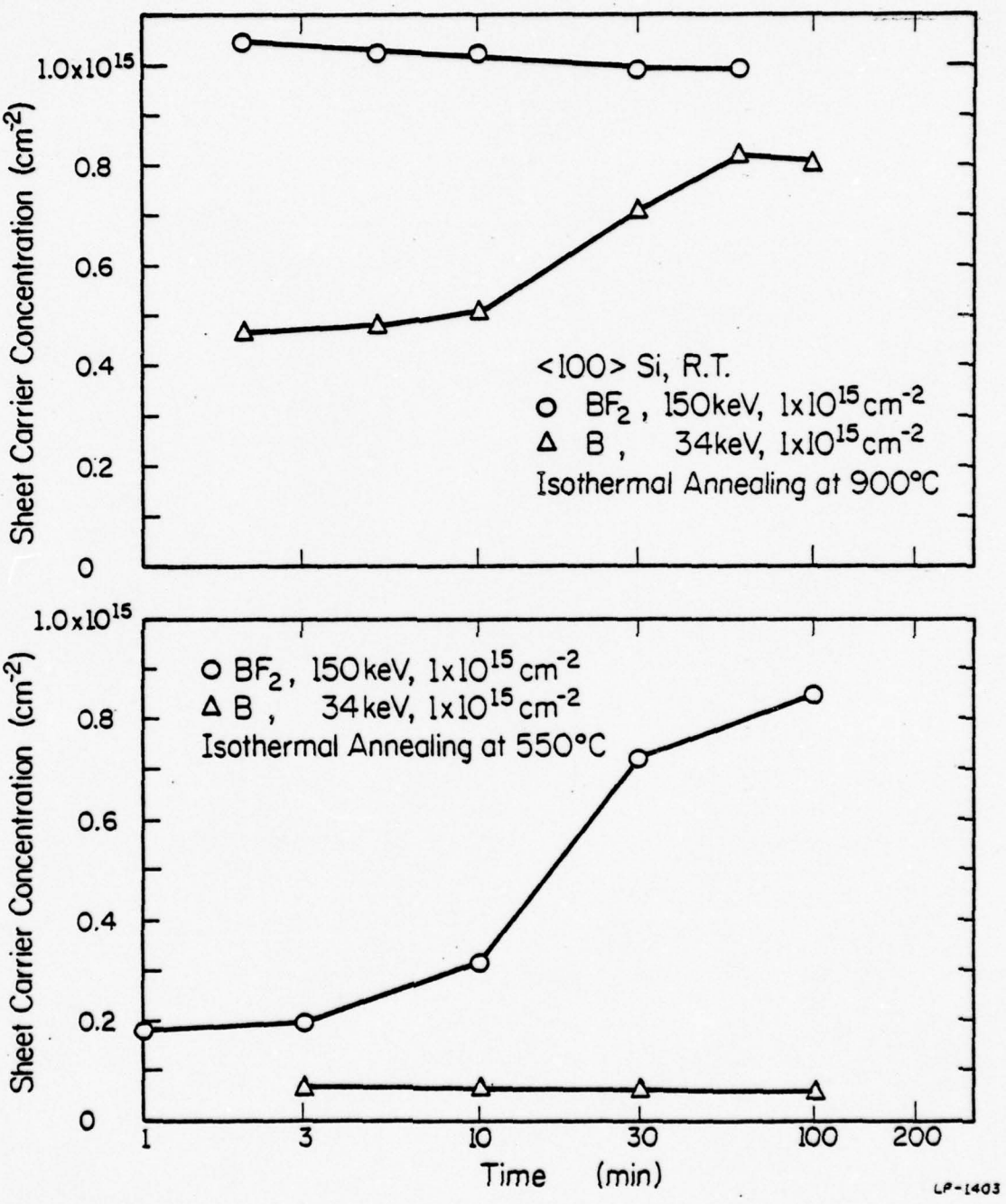

Fig. 4.2. Sheet carrier concentrations obtained from Hall measurements for Si implanted with a $1x10^{15}cm^{-2}$ fluence of B^+ or BF_2^+. The top panel illustrates isothermal annealing at 900°C, and the bottom panel is for a sample annealed at 550°C.

of acceptor activity in the BF_2^+ case is directly related to recrystallization of the amorphous layer, as the following studies of electrical carrier distribution profiles confirm. Because the recrystallization rate is a strong function of temperature [25], essentially all the boron atoms are activated within 2 min at 900°C, whereas ~ 85% are activated at 550°C within 100 min.

Figure 4.3 shows electrical carrier profiles for a BF_2^+-implanted sample after 550°C isothermal anneals over time periods from 10 min to 100 min (corresponding to the 550°C curve in Fig. 4.2). The dotted curve is the boron atomic profile, measured by SIMS. The electrically activated layer after a given anneal, which we relate to the recrystallized region, grows from the underlying crystal toward the surface. For samples annealed less than 100 min, a very high-resistivity layer is observed before the layer removal reaches the electrically active region. In this high-resistivity region, corresponding to the amorphous layer, the sheet resistivity and sheet Hall coefficient remain constant as successive layers are removed. An electrically inactive tail (shown shaded in Fig. 4.3), lies below the original amorphous-crystalline interface I. In this heavily damaged crystalline region the boron is not activated at 550°C. This observation is consistent with the lack of boron activation at 550°C for B^+-implanted Si in Fig. 4.2. On the other hand, in Fig. 4.3 ~ 100% of the implanted boron is activated in the amorphized region during 550°C recrystallization. The mobility of holes inside this recrystallized region is consistent with Irvin's [81] mobility values for bulk Si having equivalent acceptor concentrations. Although fluorine is still retained in this region at 550°C as shown in Chapter 5, it has no measurable effect

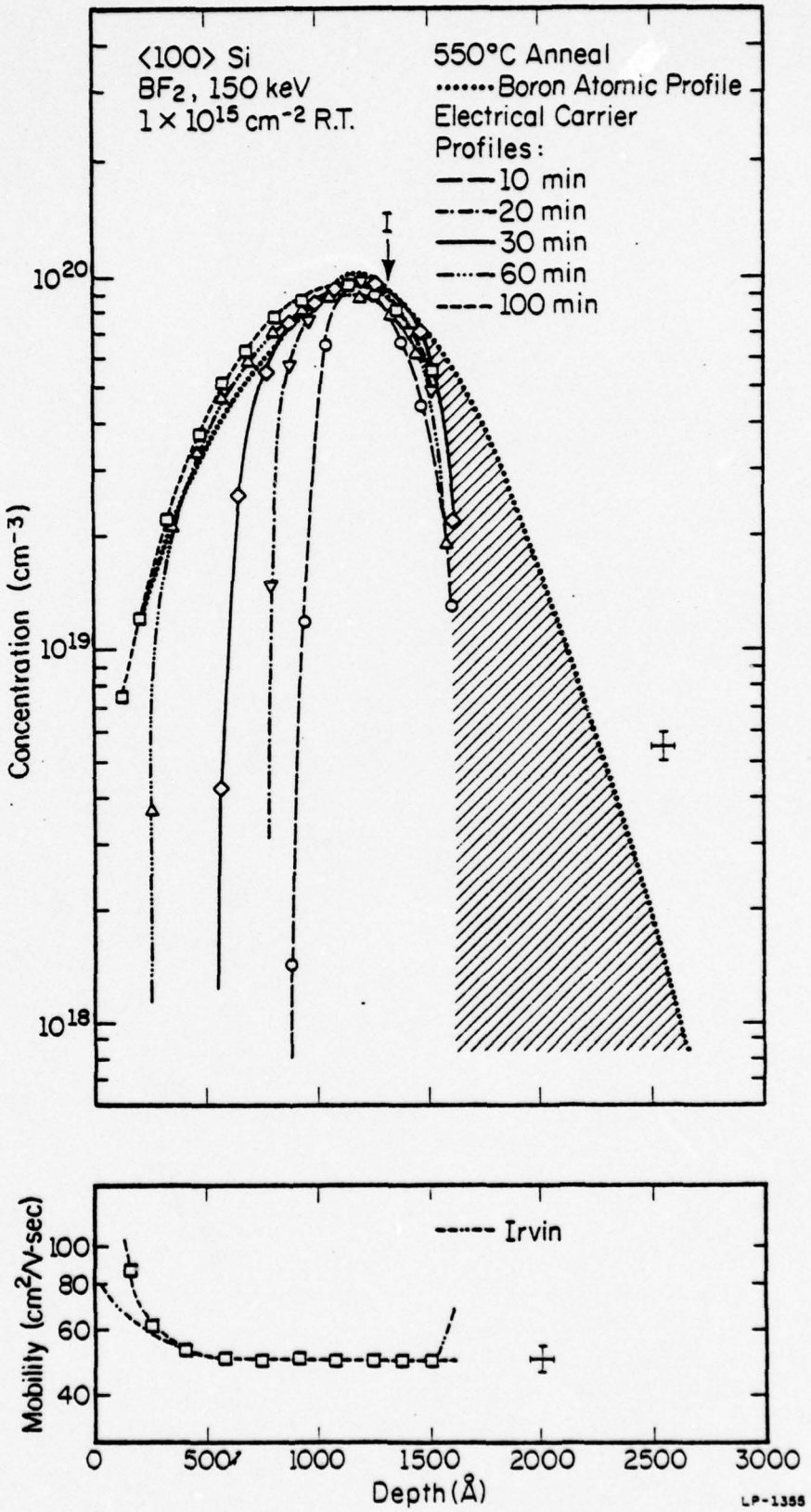

Fig. 4.3. Electrical carrier concentration and mobility profiles for BF_2^+ implanted Si after isothermal anneals shown. The dotted curve is atomic profile from SIMS. The original amorphous-crystalline interface is denoted by I.

on the electrical activation of boron or on the mobility.

In order to reduce the inactive region in the tail of the implant, it is useful to increase the thickness of the amorphous region. Samples implanted with 3×10^{15} cm^{-2} BF_2^+ (sample 3) were studied, in which the amorphous layer was measured to be 1850Å rather than the 1325Å of sample 2. At this higher dose, electrically inactive boron is found not only in the damaged crystalline tail, but also in the recrystallized amorphous layer (Fig. 4.4). An upper limit for the carrier concentration ($\sim 1.2\times10^{20}$ cm^{-3}) is observed, which apparently corresponds to the boron solid solubility at 550°C. The excess boron in the recrystallized region may be either interstitial or in a precipitate form. The mobility of holes in this case is lower than Irvin's mobility values, which is likely due to the excess boron atoms. An approximate value for solid solubility obtained from extrapolation of Trumbore's [82] curve for boron in silicon is very close to the observed 1.2×10^{20} cm^{-3}. It is clear from Fig. 4.3 that high-dose implantation does not achieve the goal of full boron activation.

Another method for extending the amorphized layer is to cool the sample during implantation. Results for a BF_2^+ implant at -110°C (sample 4) are shown in Fig. 4.5. Because the defects are less mobile at this temperature, less energy deposition per unit volume is needed to form an amorphous layer (Section 3.1). Therefore in samples implanted with 150 keV BF_2^+ to a fluence of 1×10^{15} cm^{-2} at -110°C, a continuous amorphous layer of $\sim$ 1850Å is measured. Figure 4.5 shows boron in the amorphous Si region is fully activated by recrystallization at 550°C, and the mobility is also recovered. A much smaller unactivated tail region is achieved in this sample than was observed in Fig. 4.5. Additionally, we show in Chapter 5

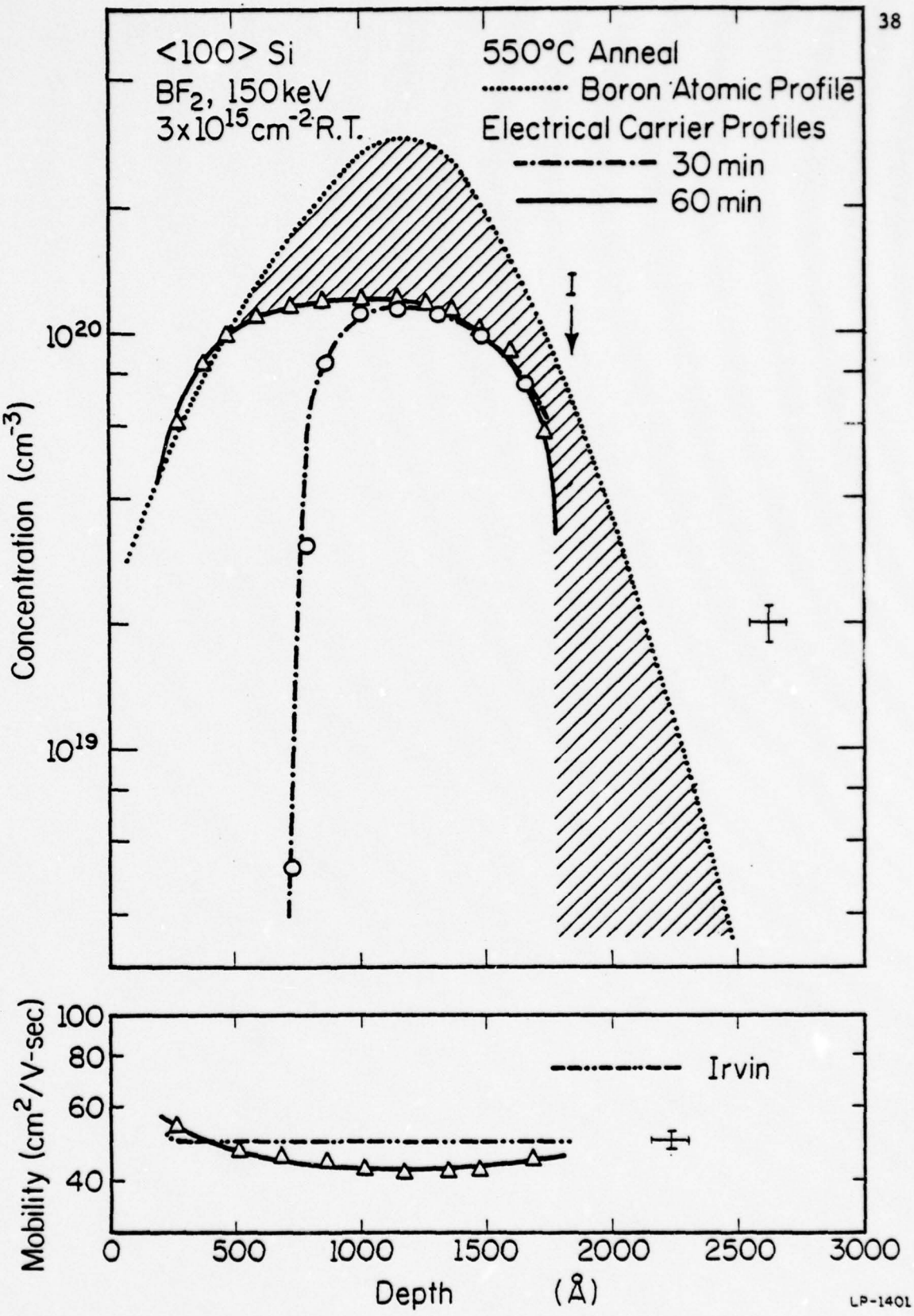

Fig. 4.4. Electrical carrier concentration and mobility profiles for a high-fluence BF_2^+ - implant and isothermal anneals. The shaded area indicates electrically inactive B atoms over much of the profile.

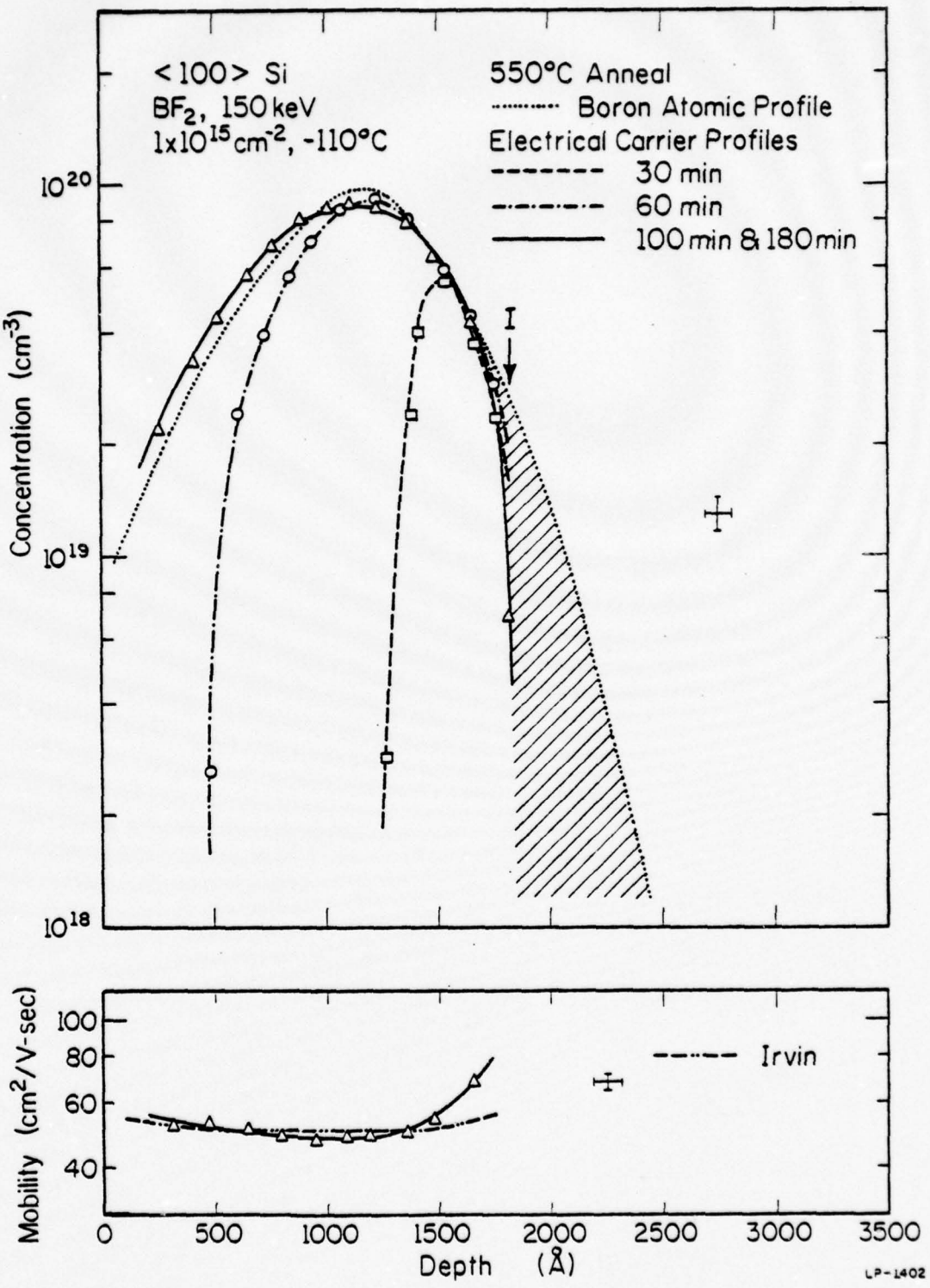

Fig. 4.5. Electrical carrier concentration and mobility profiles after a low temperature BF_2^+ implant and 550°C isothermal anneals. The shaded area indicates a smaller electrically inactive tail of the B distribution compared with Fig. 4.3.

that the retention of fluorine in samples implanted at low temperature ($\sim -110^{o}C$) is much less severe than for room temperature implants.

In order to have all the implanted boron distributed in an amorphous layer, it is necessary to predamage the sample using another implant species. In this work we used four Si^{+} implants chosen to achieve a uniform amorphous layer to $\sim 3600\text{Å}$ (as shown in Fig. 3.3). After amorphization, this sample was implanted with a $1x10^{15}$ cm^{-2} fluence of B^{+} at 34 keV (sample 5). Since all the implanted B atoms are located in the amorphized layer, a $550^{o}C$ anneal for 60 min results in 100% activation (Fig. 4.6). Good agreement between the boron atomic distribution and the electrical carrier distribution suggests that all the measured acceptors are due to boron. The mobility of this region is slightly higher than Irvin's value indicating a good quality crystal resulting from this low temperature recrystallization.

To illustrate the versatility of the use of a uniform amorphous layer, a similar Si^{+} predamaged sample was implanted with a $1x10^{13}$ cm^{-2} fluence of B^{+}. This dose level is two orders of magnitude lower than the previous case. After $550^{o}C$ annealing for 180 min, $\sim$ 100% activation was found for this case also.

Differential C-V measurements (Section 2.4) have been made on Si samples implanted with a $2x10^{15}$ cm^{-2} fluence of F^{+}, then annealed at various temperatures higher than $550^{o}C$. Negligible electrical carriers due to fluorine have been observed.

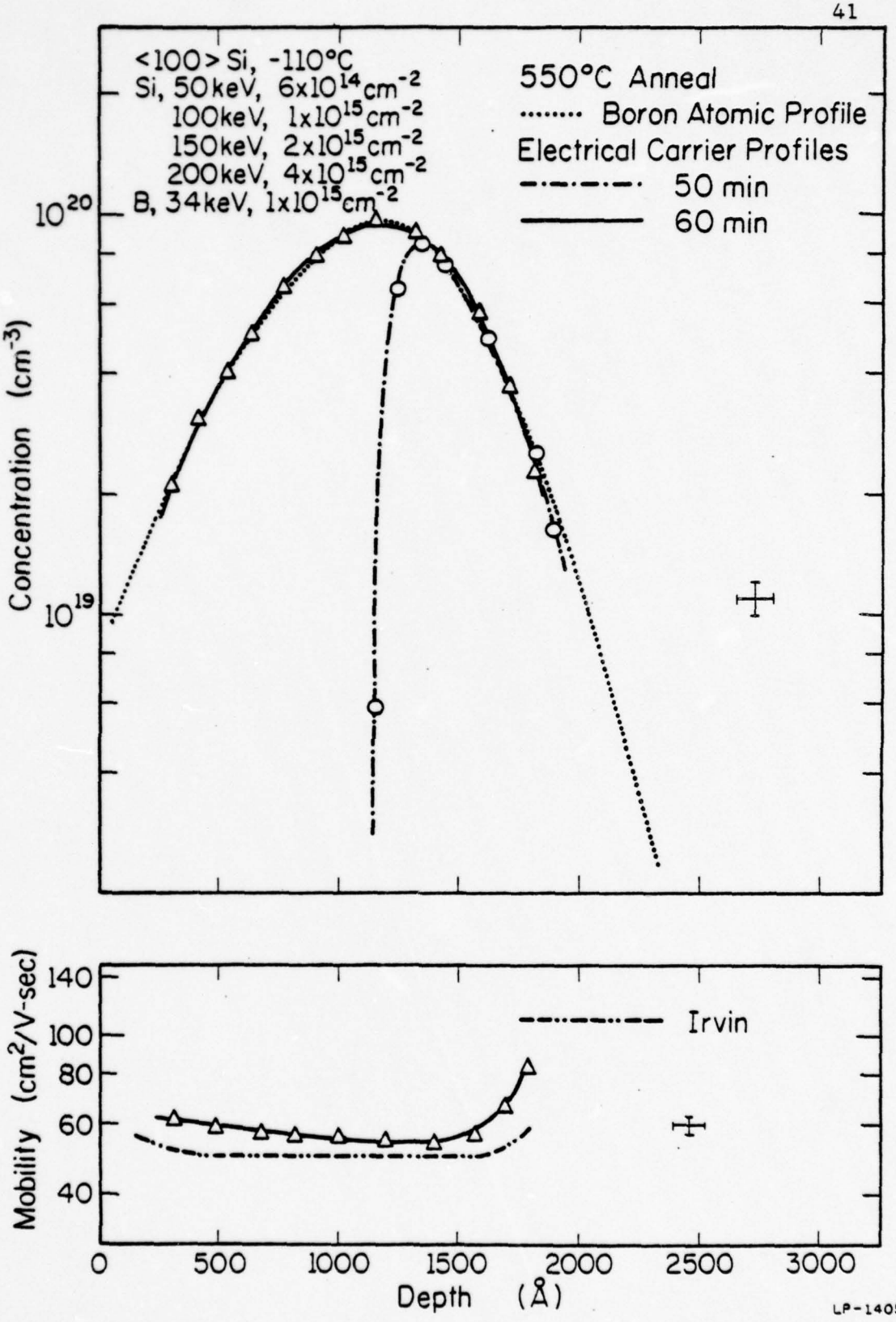

Fig. 4.6. Electrical carrier concentration and mobility profiles for a sample pre-damaged at ~ - 110°C with four Si^+ implants and then implanted with B^+, with the doses and energies shown. The amorphous-crystalline interface after the Si^+ implants was located at ~ 3600 Å in this case.

4.3. Conclusions Regarding Activation of Boron

From the results presented in the above section, some important conclusions can be drawn regarding recrystallization and the electrical activation of B in amorphized Si:

(1) Implanted B is activated at 550°C through a recrystallization process, if the boron is located in an amorphized layer. All our data are consistent with the view that recrystallization of an amorphized Si layer is an epitaxial regrowth process, in agreement with aligned backscattering observations [25].

(2) Csepregi et al. [25] found the recrystallization rate for Si^+-implanted amorphous layers on ⟨100⟩ Si to be 80Å/min. It was also found [73] that boron in the amorphous layer enhances the regrowth rate. However, for the three BF_2^+-implanted samples (2, 3, 4) studied here, the regrowth rate is always much lower than 80Å/min. From the thickness of the recrystallized region as a function of annealing time, we estimate a growth rate in the range 10-50Å/min. Since both B and F distribution are nonuniform, no exact regrowth rate can be calculated from these experiments. We conclude, however, that fluorine reduces the regrowth rate of amorphous Si. Figure 4.6 shows the entire B profile is activated after the 60 min anneal. This sample had no appreciable sheet carrier concentration after 40 min annealing because the recrystallization had barely reached the boron profile. Therefore we conclude that most of the B profile is recrystallized in the final 20 min. The estimated regrowth

rate in the region containing B is larger than 100Å/min. This recrystallization rate is much higher than the case when fluorine is present.

(3) All BF_2^+-implanted Si samples have an inactive tail region. Only the Si^+ predamaged sample has a fully activated profile. This verifies the suggestion that a damaged crystalline silicon region exists near the original amorphous-crystalline interface after the 550°C recrystallization. Further studies are necessary to understand the nature of this damaged region. However, fluorine data presented in Chapter 5 provide some insight into the severity of the damage.

(4) Full electrical activation is possible for boron implanted into samples predamaged by deeper Si^+ implants. This indicates low temperature (~ 550°C) annealing is possible for boron implantation if the entire boron profile is located in an amorphized layer and the boron concentration does not exceed the solid solubility.

5. MIGRATION OF FLUORINE IN BF_2^+-IMPLANTED SILICON

The electrical properties of BF_2^+-implanted Si have been discussed in Chapter 4. However, the distribution of fluorine in such samples after annealing has not previously been studied. In a preliminary discussion of this study, we reported that fluorine migrates anomalously during annealing in Si samples implanted with a $1x10^{15}$ cm^{-2} fluence of BF_2^+, resulting in double peaks in fluorine distribution [78]. Dietrich et al. [83,84] observed similar anomalous impurity migration in Si implanted with high-dose Al^+ or Ga^+. Since this redistribution relates to high-dose implantation, it is important to understand the mechanism of this redistribution.

In this chapter, we discuss fluorine distributions measured by secondary ion mass spectrometry (SIMS). A wide range of implant doses and temperatures, as well as annealing temperatures and times, have been studied to understand the mechanisms of fluorine migration in Si. We find that the formation of fluorine multiple peaks and other effects can be explained reasonably and consistently in terms of outdiffusion, redistribution during recrystallization, and gettering by the ion damage.

5.1. Sample Preparation and Measurements

Single crystal 4-6 Ω-cm phosphorus doped ⟨100⟩ silicon was used throughout this study. The implantation schedules and temperatures are listed in Table 5.1. The implantation and annealing techniques used here are identical to those described in Chapter 4. To obtain annealing data, a separate sample from the implanted wafer was annealed at a particular time and temperature in the isothermal or isochronal annealing schedule.

Table 5.1. Implant sequences for various samples studied in this work. The implantation temperatures are also listed.

Sample No.	Ion	Implant Parameters		Implant Temp.
		Energy(keV)	Dose(cm^{-2})	
A	$^{11}B^{19}F_2$	150	$1x10^{15}$	$\lesssim 30^{o}C$
B	$^{11}B^{19}F_2$	150	$1x10^{13}$	$\lesssim 30^{o}C$
C	^{28}Si	50	$6x10^{14}$	$\sim -110^{o}C$
		100	$1x10^{15}$	
		150	$2x10^{15}$	
		200	$4x10^{15}$	
	$^{11}B^{19}F_2$	150	$1x10^{15}$	
D	$^{11}B^{19}F_2$	150	$1x10^{15}$	$\sim -110^{o}C$
E	$^{11}B^{19}F_2$	150	$1x10^{15}$	$\lesssim 30^{o}C$
	^{11}B	25	$1x10^{15}$	
	^{11}B	85	$1x10^{15}$	

The thickness of the amorphous layer after implantation was measured by a Sloan Dektak stylus over an etched step formed by the HF etching technique. An interference microscope (also used for SIMS crater depth measurement) was used as a cross-calibration on some etched steps, and negligible differences were found for the two measurements.

Chemical depth profiles of fluorine were determined with an ion microprobe mass spectrometer (AEI Model IM20). Fluorine profiles were obtained by monitoring the $^{19}F^-$ secondary ions produced by Cs^+ primary ion bombardment. The SIMS technique and conversion from ion counts to atomic profiles have been discussed in Section 2.5.

5.2. Fluorine Migration

Fluorine distribution profiles have been obtained from SIMS measurements of the samples listed in Table 5.1 after 30 min anneals in the temperature range 400° - 1100°C. In most cases measurements were made for 100°C increments in the isochronal anneals. Only representative fluorine profiles are presented here to illustrate salient features of the migration phenomena.

Figure 5.1 shows the fluorine distribution profiles of Si samples implanted at room temperature with a $1x10^{15}$ cm^{-2} fluence of BF_2^+ (sample A of Table 5.1) and then isochronally annealed for 30 min. After annealing at temperatures above 500°C, the fluorine is redistributed drastically, and the migration is clearly influenced by lattice damage. Finally, after 1100°C annealing, most of the fluorine atoms diffuse out. A continuous amorphous layer ~ 1325Å thick was found on the surface of this sample after implantation. The dashed line I in Fig. 5.1 represents

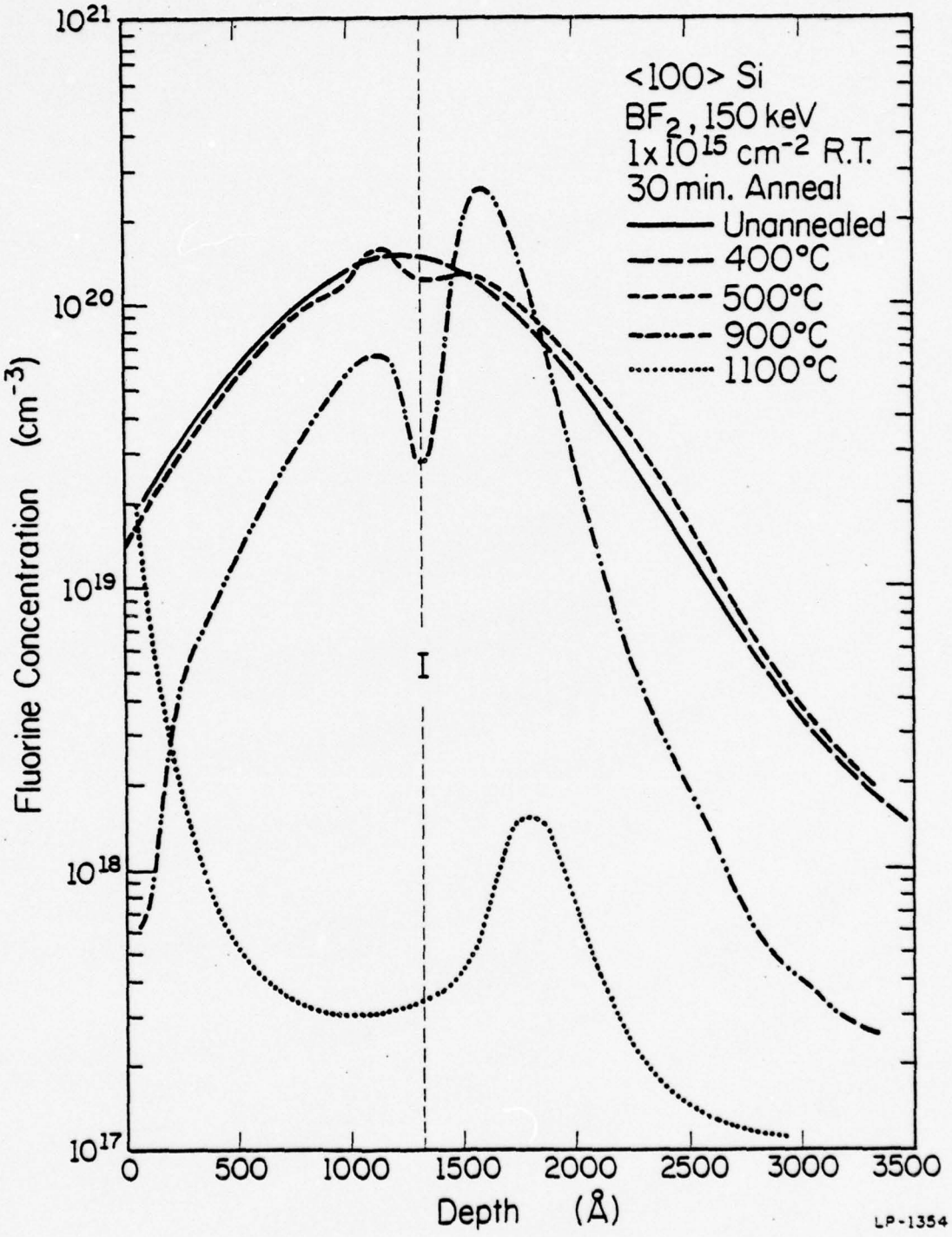

Fig. 5.1. Fluorine atomic profiles obtained from SIMS measurements on ⟨100⟩ Si implanted at room temperature with a $1x10^{15}cm^{-2}$ fluence of BF_2^+ (sample A of Table 5.1) and annealed for 30 min at the temperatures shown. A thin dashed line (I) represents the amorphous-crystalline interface after implantation.

the interface between amorphous and crystalline Si. Underneath this interface, a damaged region was detected from electrical measurements discussed in Chapter 4.

The amorphous layer and damaged crystalline region strongly influence the fluorine redistribution during annealing. Fluorine in the amorphous layer does not redistribute until recrystallization occurs near 500°C. During recrystallization fluorine is pushed ahead of the moving amorphous-crystalline interface, as discussed below. The 900°C curve of Fig. 5.1 shows the fluorine distribution after the amorphous region is completely recrystallized. The shallower peak near 1200Å corresponds to the implantation peak after outdiffusion at this temperature. The pronounced deeper peak occurs in the region below I which was heavily damaged but not amorphized by the implantation. This damaged region attracts fluorine atoms, which are relatively mobile at this temperature. It is interesting to note that the fluorine concentration in this region is greater after the 900°C anneal than it was after the implantation. This preferential migration to a defect-rich region is similar to the ion-damage gettering discussed by Seidel et al. [85]. The damaged region responsible for fluorine gettering in Fig. 5.1 also gives rise to the electrically inactive tail of the boron distribution in Fig. 4.3 of Chapter 4. When the sample is annealed at 1100°C, the fluorine peaks of Fig. 5.1 diminish and most of the fluorine atoms diffuse out.

Figure 5.2 illustrates fluorine migration in a Si sample implanted with 1×10^{13} cm^{-2} BF_2^+ at room temperature (sample B of Table 5.1). Since a fluence of 1×10^{13} cm^{-2} is well below the critical dose needed to form an amorphous layer in Si [30], the implanted fluorine is distributed in

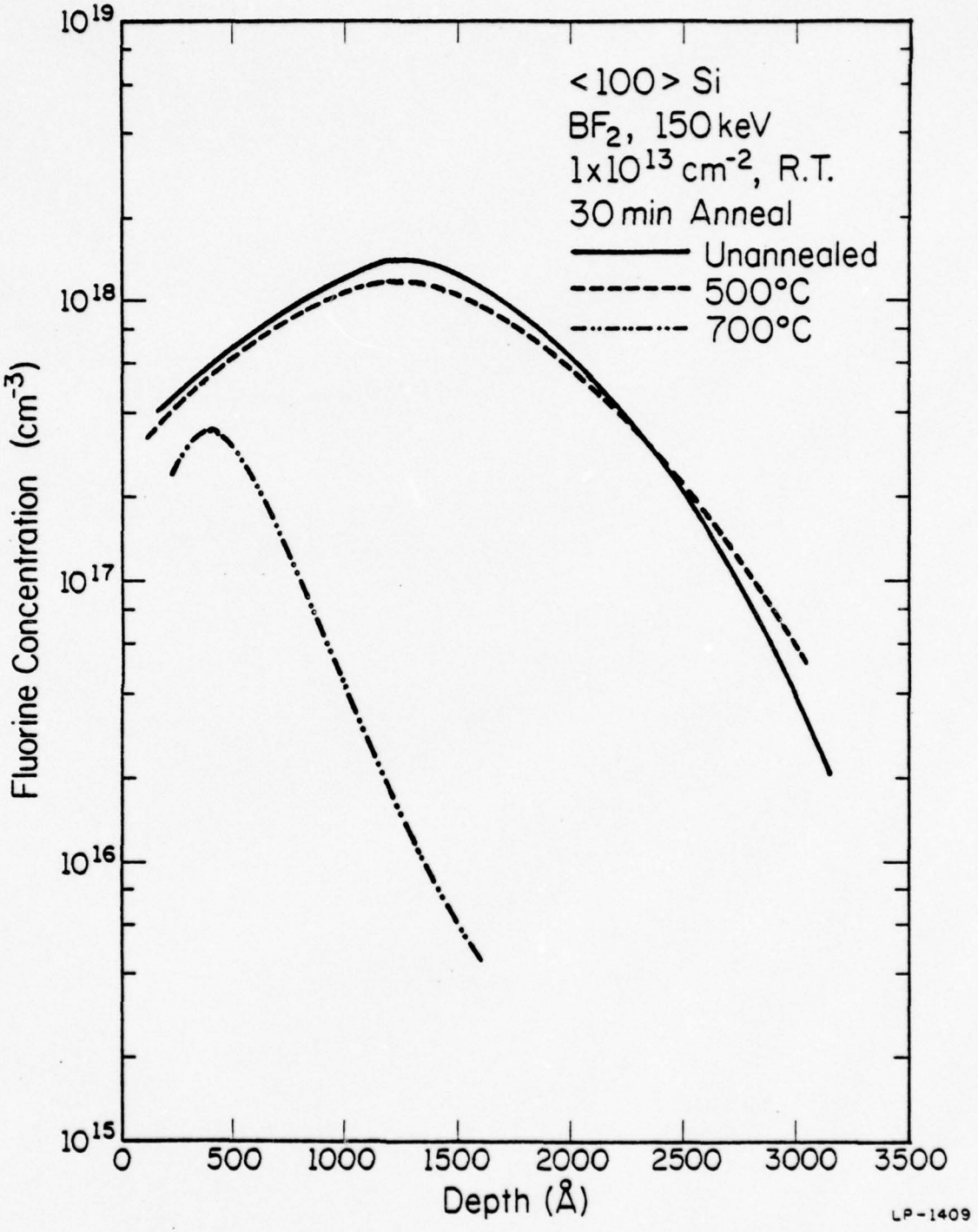

Fig. 5.2. Fluorine profiles for a relatively light (1×10^{13} cm^{-2}) fluence of BF_2^+ (sample B) after implantation and after annealing at the indicated temperatures.

crystalline silicon. As a result, the migration of fluorine during annealing is quite different from Fig. 5.1. In Fig. 5.2 fluorine diffuses to the surface with no evidence of the multiple-peak structure seen before. After 900°C annealing, no fluorine retention was detected, within the sensitivity of the SIMS measurement. In relatively lightly damaged crystalline Si, fluorine migration during annealing is apparently due to a simple outdiffusion process.

In sample C a continuous amorphous Si layer (~ 3600Å) was created by four Si^+ implants. A $1x10^{15}$ cm^{-2} fluence of BF_2^+ was then implanted, such that the implanted fluorine atoms were distributed within the amorphous layer. To ensure a uniform amorphous layer, both the Si^+ and the BF_2^+ implants were done at ~ -110°C. Representative fluorine distribution profiles for sample C annealed isochronally in the range 500° - 1100°C are shown in Fig. 5.3. No multiple peaks are observed for fluorine in the amorphized layer. The 500°C curve is identical to the as-implanted profile, since recrystallization from the ~ 3600Å deep interface has not reached the fluorine during the 30 min 500°C anneal (the regrowth rate on ⟨100⟩ Si is ~ 9Å/min at 500°C) [25]. The 700°C and 900°C curves illustrate that after the amorphous layer is recrystallized, some of the fluorine atoms migrate to the surface and diffuse out. It is interesting to note, however, that much of the fluorine remains near the implanted peak at these temperatures, in contrast with the more lightly damaged case (Fig. 5.2). The most dramatic result of Fig. 5.3 is the appearance of a new fluorine peak near 4100Å after the 900°C anneal. This peak occurs in the damaged crystalline region just below the original amorphous layer (marked by I) formed by the Si^+ implants. It is clear in

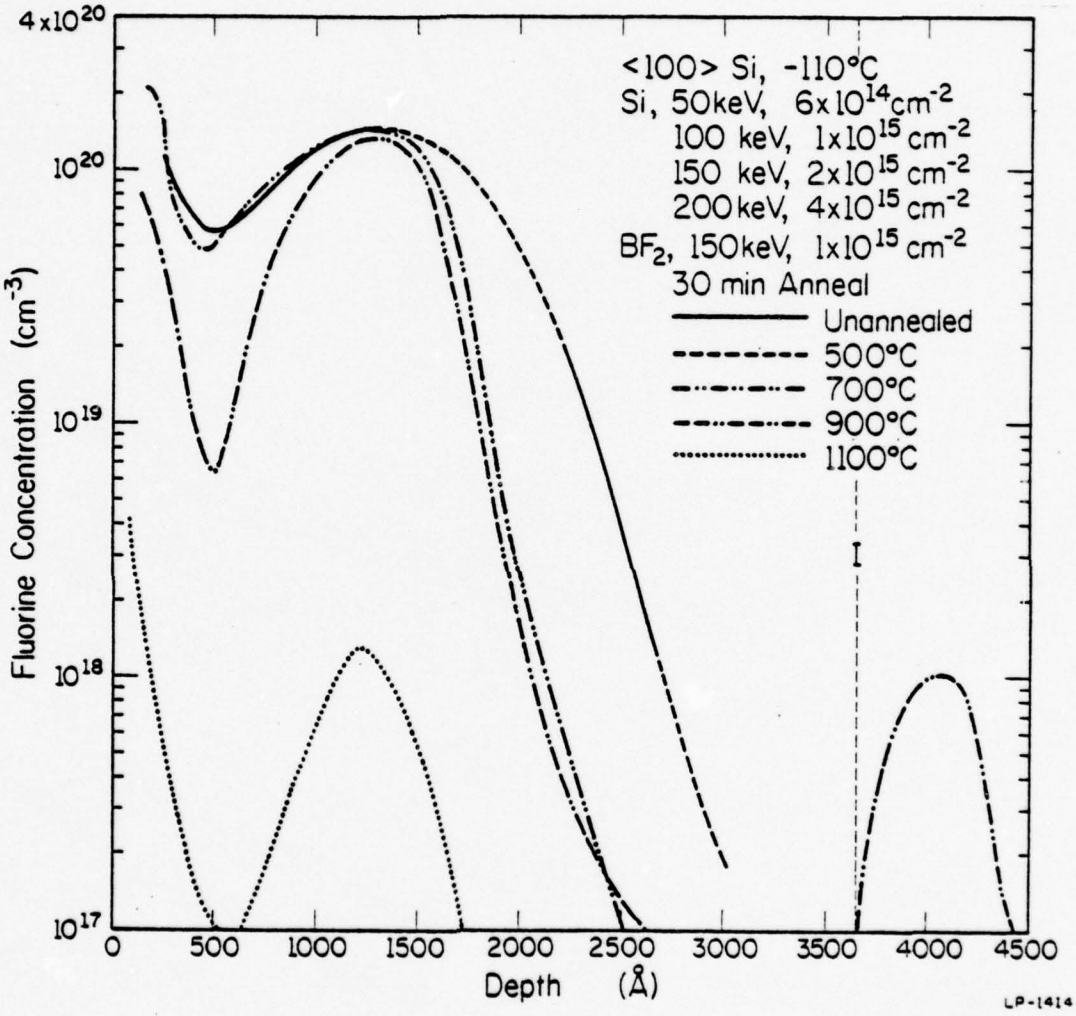

Fig. 5.3. Fluorine profiles following a BF_2^+ implant into an amorphous layer, and subsequent annealing. The amorphous layer was formed by four Si^+ implants with doses and energies shown (sample C). All implants were performed at - 110°C. The amorphous-crystalline interface after the Si^+ implantations is marked by I.

this case that the peak is due to gettering of fluorine by the damage, since there was no fluorine implanted into this region of the crystal. This observation confirms our proposal that damage gettering causes the second peak in the 900°C curve of Fig. 5.1.

To investigate the fluorine redistribution occurring during recrystallization, Si implanted with a $1x10^{15}$ cm^{-2} fluence of BF_2^+ at $\sim$ -110°C (sample D) was annealed at 550°C for 10, 30, and 100 min. Figure 5.4 shows how the fluorine is redistributed during this 550°C recrystallization. Since the fluorine is not very mobile at this temperature, the redistribution is due almost entirely to accumulation at the amorphous-crystalline interface as it moves from I to the surface. The "spike" in the fluorine profile moving toward the surface as the recrystallization proceeds is reminiscent of zone refining effects. The corresponding spike in the 500°C profile of Fig. 5.1 is apparently due to this same mechanism, since the amorphous-crystalline interface should move to about that point in 30 min at 500°C. The positions of the fluorine spikes in Fig. 5.4 are in fairly good agreement with the edge of the recrystallized region for corresponding times obtained from electrical measurement in Fig. 4.5 of Chapter 4. For higher temperatures ($\geq$ 700°C), the recrystallization is completed in less than 30 min. Therefore such spikes are not observed in the high temperature curves in Figs. 5.1 and 5.3. There is, however, a dip in the fluorine distribution at I in all cases for which the implanted amorphous-crystalline interface occurs within the fluorine profile (Figs. 5.1, 4, and 5).

Representative fluorine distribution curves are plotted in Fig. 5.5 for sample D annealed for 30 min in the range 500° - 1100°C. The difference

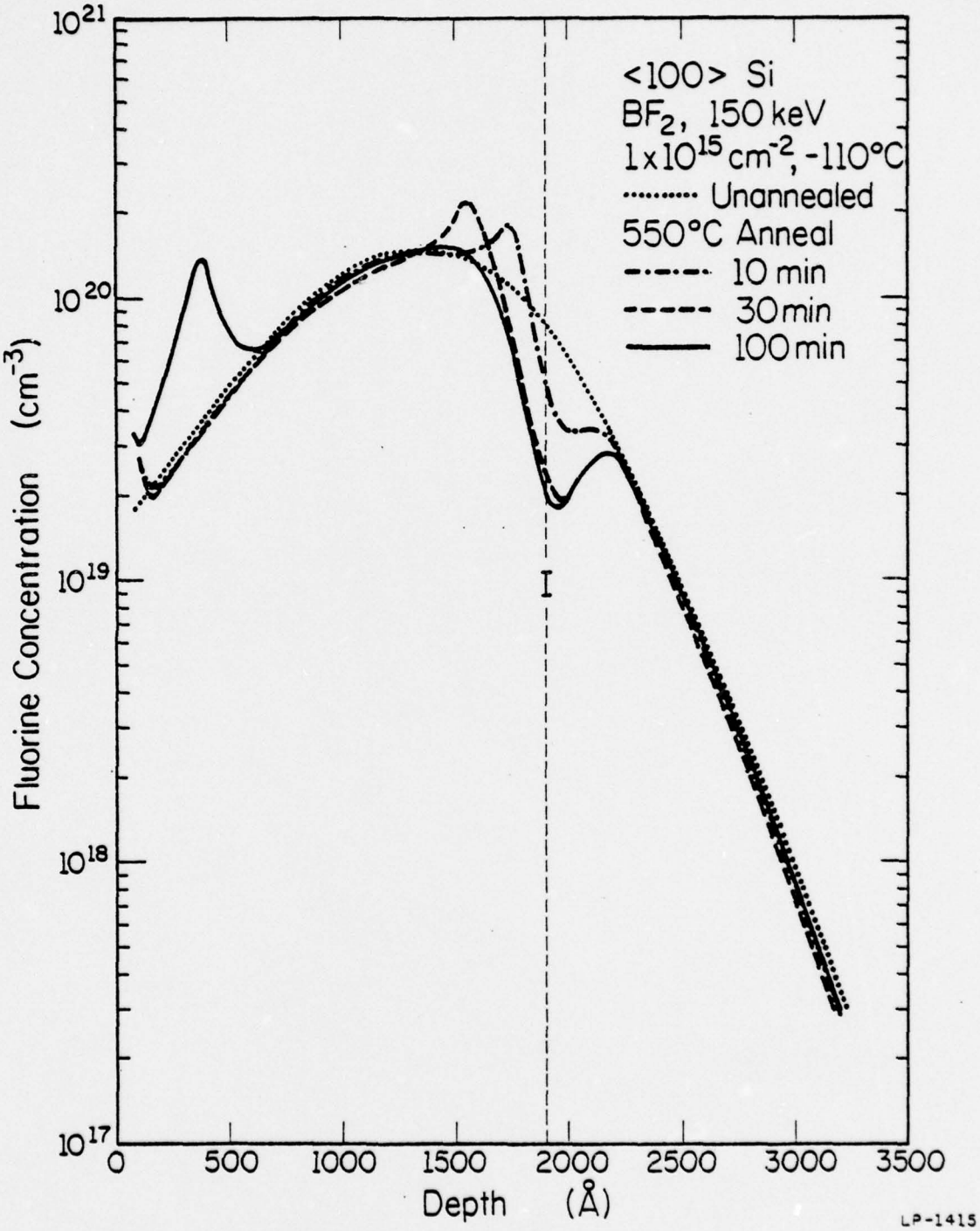

Fig. 5.4. Fluorine profiles resulting from isothermal anneals of BF_2^+ - implanted Si (sample D). The thin dashed line (I) represents the amorphous-crystalline interface after implantation.

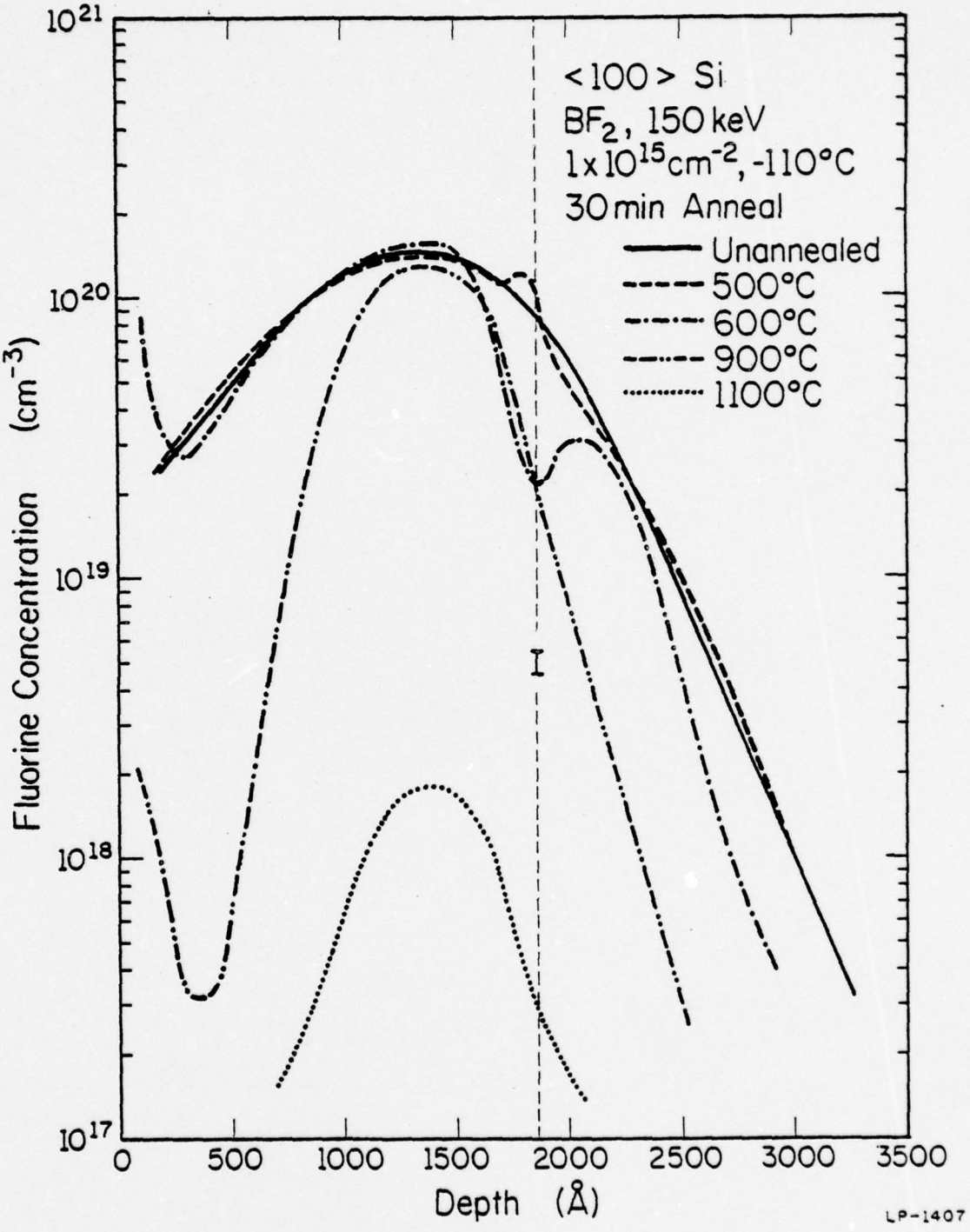

Fig. 5.5. Fluorine profiles for Si implanted with BF_2^+ at - 110°C (sample D) and annealed is ochronally. The amorphous-crystalline interface after implantation is indicated (I).

between samples A and D is the lower implantation temperature for sample D, resulting in a much thicker amorphized layer ($\sim$ 1850Å). As was the case for sample A, the redistribution begins with the 500°C anneal, and a small spike is observed in the 500°C curve corresponding approximately to the expected amorphous-crystalline interface position for 30 min at 500°C. The dip in the 500°C and 600°C curves at I is also similar to effects observed in Fig. 5.1. After sample D is annealed at a higher temperature ($\geq$ 700°C), however, the peak below I starts to diminish. The 900°C curve has only a single peak, corresponding to the original fluorine peak. The absence of a second peak below I after the 900°C anneal is in sharp contrast with Fig. 5.1, and illustrates that the damage underlying the amorphous region is much less in the case of the low temperature BF_2^+ implant.

To examine possible influence of boron on the fluorine redistribution in BF_2^+-implanted samples, sample A was implanted with two additional boron fluences (sample E of Table 5.1). The two energies used provide boron peaks at 825Å (within the amorphous region) and 2600Å (below I). After annealing at 700°C and 1000°C for 30 min, the fluorine distributions exhibited the same double peaks observed for sample A.

The as-implanted projected range (R_p) of fluorine for 150 keV BF_2^+-implants into Si is measured to be $\sim$ 1300Å for all samples studied here. Assuming that the BF_2 molecule splits into its components with energies apportioned by mass ratio, ^{19}F has 58 keV in these implants. SIMS measurements on a Si sample implanted with 58 keV $^{19}F^+$ to a fluence of 2×10^{15} cm^{-2} agrees well with the F profile observed in BF_2^+-implanted samples, confirming the energy apportioning assumption. However, the value for R_p measured here is significantly less than predicted by the

usual range statistics [35], even after the third moment correction (calculated R_p = 1504Å). This observation is in agreement with other work for $^{19}F^+$-implanted silicon [38].

5.3. Conclusions Regarding Fluorine Migration

The results presented here lead us to conclude that the existence of an amorphous Si layer and a damaged crystalline layer dominates the anomalous fluorine migration in BF_2^+-implanted Si during annealing. The sweeping out of fluorine during recrystallization (Fig. 5.4) and the gettering of fluorine by residual defects (Figs. 5.1 and 5.3) are the major causes of anomalous migration. These effects may also occur in high-dose Al- or Ga-implanted silicon [83].

The property of fluorine gettering by defects suggests the use of fluorine as a decorator for identifying damaged regions. For example, the damaged region below I in Fig. 5.3 is dramatically decorated by fluorine during annealing. Furthermore, by comparing the second peak of Fig. 5.1 with that of Fig. 5.5, it is clear that after recrystallization much less damage is left below the amorphized layer in the sample implanted at low temperature.

6. SURFACE CONTAMINATION DURING ION IMPLANTATION

Surface contamination produced by ion implantation is a troublesome problem commonly associated with high-dose implantation. It is known that ion-beam induced polymerization of adsorbed hydrocarbons leads to the formation of a carbonaceous surface contamination layer on ion-implanted samples [71,72]. The primary source of hydrocarbon molecules is the implanter residual vacuum. The thickness of this contamination layer increases with dose such that heavily implanted Si exhibits noticeable contamination problems (Section 3.3). Recoiled carbon may produce structural damage affecting the reverse current of a shallow p-n junction [86], and silicon carbide may be formed during post-implantation annealing [87].

In an effort to better understand this contamination problem and thereby elucidate a solution, we have used Auger electron spectroscopy (AES) to examine the surface layers of high-dose implanted silicon prepared under a variety of implantation conditions. Various layer removal techniques were evaluated. The effects of implantation temperature and type of diffusion pump oil in the implanter vacuum system have also been investigated. Finally, the effects of surface contamination on chemical etching and ohmic contact formation have been assessed.

6.1. Sample Preparation and Measurements

Single crystal ⟨100⟩ Si, used as starting material throughout this study, was cleaned successively in organic solvents, peroxide solution (defined below), and buffered HF, and was rinsed in deionized water prior to implantation. A portion of the unimplanted wafer was retained as a control specimen. Two samples were implanted with Si^+ to a total fluence of

$\sim 8x10^{15}$ cm^{-2}, one at $\sim -110^{o}C$ (sample A) and the other at $\sim 30^{o}C$ (sample A'). Four energies of Si^{+} were used in the range of 50 to 200 keV to produce a uniform amorphous Si layer (See sample 5 of Table 4.1.). Room temperature BF_2^{+} implants were performed on two other samples, with fluences of $1x10^{15}$ and $3x10^{15}$ cm^{-2} at 150 keV. The target chamber was pumped to $\leq 10^{-6}$ torr during these implantations by an NRC diffusion pump with a water baffle and liquid nitrogen cold trap. The ion beam current density was maintained at $\sim 0.1 - 0.2$ $\mu A/cm^2$. The target chamber vacuum system was subsequently modified by replacing the silicone based diffusion pump oil (methylphenylpolysiloxane) [88] with Fomblin^{TM} perfluorinated polyether fluid [89] and installing a liquid nitrogen cold trap between the roughing pump and the target chamber. The latter change is expected to have a minimal effect for typically short roughing cycles, due to the small mean free path for oil molecules at the minimum roughing pressure of ~ 80 μm [90]. This modified chamber was pumped by the new fluid for 20 hrs to remove residue of the original pump oil. Sample B was then implanted with Si^{+} using the same energy and fluence combination as for sample A.

The following contamination removal techniques were applied to specimens of sample A to determine their relative removal efficiency:

1) Solvent cleaning - samples were immersed sequentially in trichloroethylene, acetone, and methanol for 2 min each with ultrasonic agitation.

2) Peroxide solution cleaning - samples were immersed in a solution composed of 6:1:1 by volume $H_2O:H_2O_2:NH_4OH$ at $80 \pm 5^{o}C$ for 10 min [91], followed by a rinse in deionized water.

3) Anodic oxidation and stripping - samples were anodized at 100V in an electrolyte consisting by volume of 2% aqueous KNO_3 and 98% ethylene glycol [92]. Oxide stripping was performed in buffered HF solution. Typically 100-150Å of silicon is removed from the surface of a clean Si sample by this procedure.

4) Heat treatment - after implantation samples were annealed at 550°C for 100 min under flowing forming gas.

All AES depth profiling studies were performed using the custom built thin-film analyzer described in Section 2.6. Depth profiling was accomplished with 1.0 keV Ar^+ at a current density of ~ 20 μamp/cm^2. These conditions correspond to a sputtering rate of approximately 10Å/min in silicon. The sputtering rate of pure carbon is somewhat slower [93].

Etching studies were conducted using a slow etch (1:750:250 by volume $HF:HNO_3:HCH_2COOH$) or a fast etch (1:3:12 by volume $HF:HNO_3:HCH_2COOH$). Etched samples were observed using conventional optical microscopy, and also with Auger elemental mapping using a Physical Electronics Model 545 scanning Auger microprobe.

The effect of surface contamination on ohmic contact formation was investigated by measuring the current-voltage characteristics between Au metal contacts formed on the implanted layers. These Au pads, 25 mils square and separated by 31 mils, were applied by evaporation through a grid mask. To study contact formation on samples A and B, a B^+ implantation to a fluence of $1x10^{13}$ cm^{-2} was performed in addition to the Si^+ implants, and then the samples were annealed at 900°C for 30 min.

6.2. Studies of the Surface Layer

Figure 6.1 shows the AES depth profile obtained from sample A. The presence of a carbonaceous overlayer is apparent for this sample, which was implanted while the target chamber was pumped using conventional diffusion pump oil. The native oxide, present on the sample prior to implantation, serves to locate the original sample surface. Silicon was detected throughout the carbon layer, but does not appear in the depth profile due to the method of background subtraction used [56]. The thickness of the carbon layer is estimated to be about 100Å. A duplicate profile of a separate specimen from sample A, using the same analytical conditions, reproduced this thickness within 3%. The effect of sample temperature during implantation is illustrated in Fig. 6.2. The carbon thickness of sample A (implanted at -110°C) is considerably thicker than that of sample A' (implanted to the same fluence at room temperature). Sputtering conditions were held constant for the two analyses, and therefore the sputtering times of Fig. 6.2 are representative of relative thickness. The thicker contamination layer for the lower temperature implant is consistent with a physisorption model in which the absorption probability increases with decreasing temperature. However, even though a thinner contamination layer was observed on sample A', this sample did exhibit uneven etch characteristics and relatively poor ohmic contact formation.

Depth profiles from samples implanted with various fluences of BF_2^+ indicate that the contamination layer thickness increases roughly linearly with dose in the range $1\text{-}10\times10^{15}$ cm^{-2}, in good agreement with the observation by Naehring *et al*. [94]. This implies that the contamination reported here is a general problem not limited to Si^+ implants.

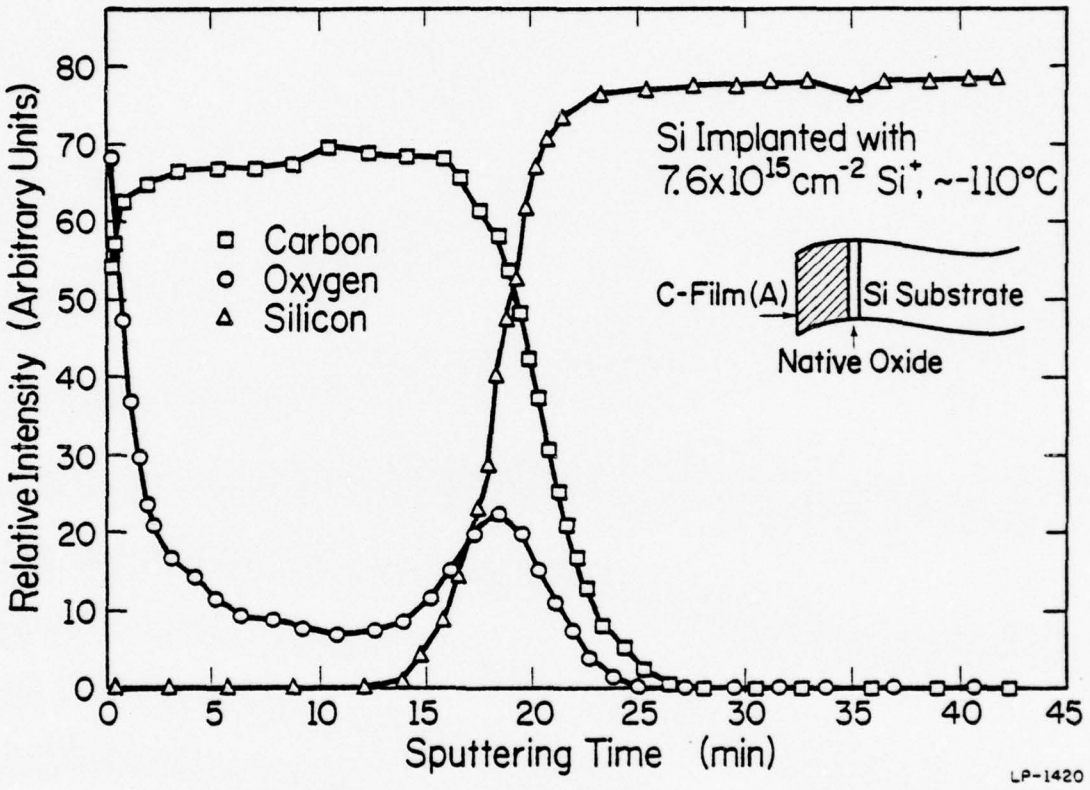

Fig. 6.1. Auger electron spectroscopy (AES) depth profile for Si implanted with $\sim 8 \times 10^{15} cm^{-2}$ Si^+ at $\sim$ - 100°C in a target chamber pumped with standard diffusion pump oil (sample A). The carbonaceous contamination layer is shown by the carbon signal, and the native oxide by the oxygen signal.

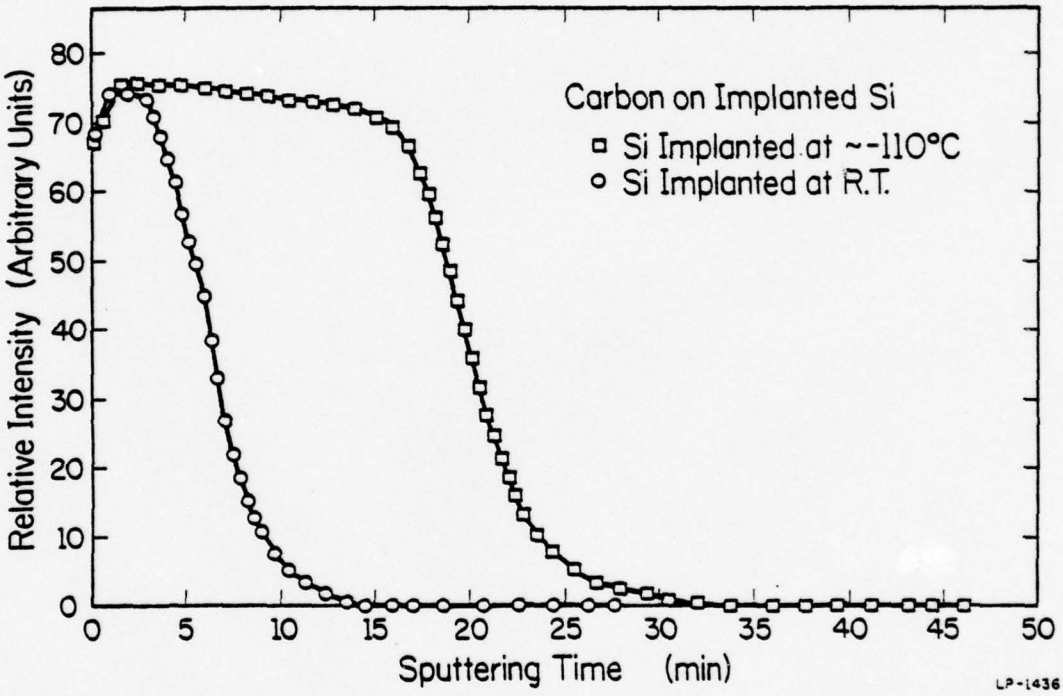

Fig. 6.2. AES depth profiles of carbon for sample A (implanted at ~ - 100°C) and sample A′ (implanted at room temperature). Both samples received a fluence of ~ 8×10^{15} cm^{-2} at four energies in the range 50 - 200 keV.

Figure 6.3 shows AES depth profiles obtained from different pieces of sample A after cleaning using the various techniques described above. These data show that for the methods studied only anodic oxidation and stripping is capable of completely removing the contamination. The other procedures are able to remove only a small fraction of the carbonaceous layer. The annealing result is in agreement with the observations of Yamaguchi and Hirayama [72] that heat treatment is ineffective once the layer is formed. Although anodic oxidation and stripping do effectively remove the contamination layer, it is not a procedure which might readily be adapted as a device fabrication processing step.

Clearly, it is more desirable to eliminate the contamination mechanism rather than attempting to remove layers such as those shown in Figs. 6.1-6.3. Two methods have been proposed previously [71]: (1) heating the sample during implantation, and (2) installing a liquid nitrogen shroud around the sample holder. However, it has been demonstrated that high temperature implantation can lead to poor electrical activation [95] and high damage levels after annealing [26]. The cold trap method leads to implanter design difficulties and will not completely eliminate the problem when the sample is also liquid nitrogen cooled, which is sometimes useful for high-dose implantation [26,96].

The surface contamination problem encountered in ion implantation is essentially the same as that observed in electron beam systems [88,97]. Without a major modification, Conru et al. [98] were able to eliminate carbon contamination by using Fomblin^{TM} perfluorinated polyether diffusion pump fluid. The improvement results from a significant reduction in polymerization

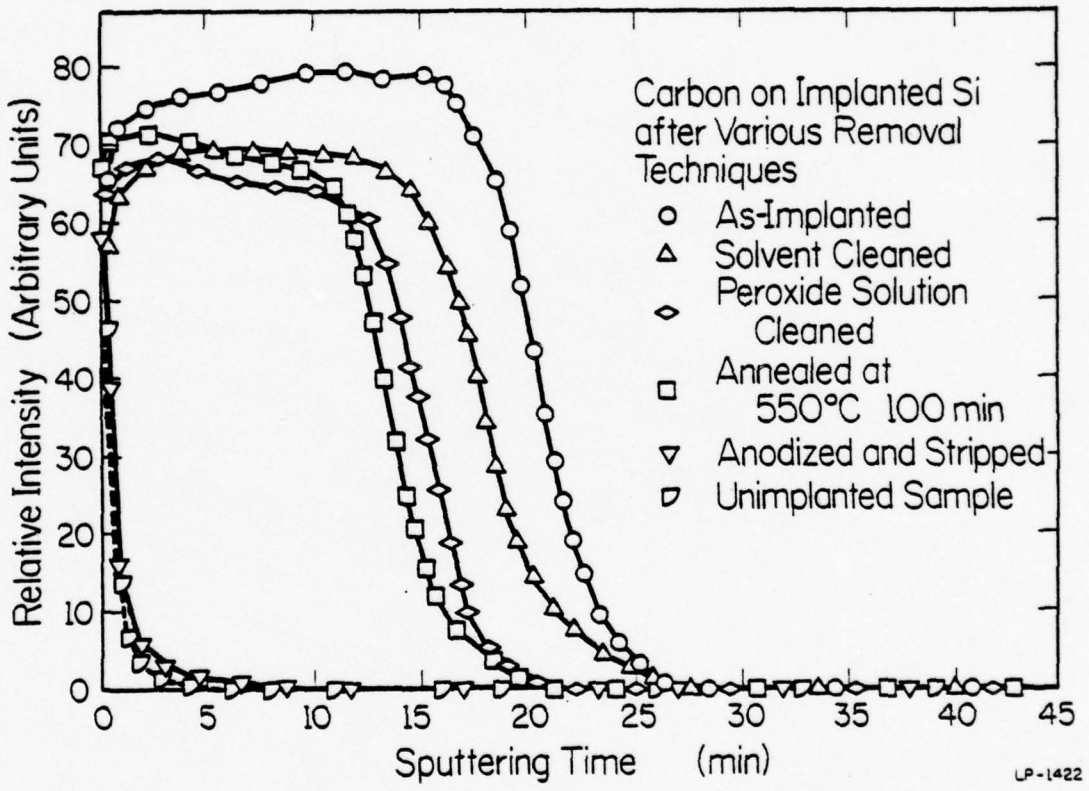

Fig. 6.3. AES depth profiles of sample A after various surface contamination removal techniques. The as-implanted and unimplanted samples are shown for comparison.

of this compound during electron beam irradiation [99]. Figure 6.4 shows the AES depth profile obtained for sample B, implanted under the same conditions as sample A but with the Fomblin fluid used in the diffusion pump of the target chamber vacuum system. It is clear that a significant imporvement is made by replacing the diffusion pump fluid.

In device fabrication or when characterizing an implanted Si wafer it is sometimes necessary to uniformly etch part of the sample. It has been reported that after a high-dose implant, nonuniform etching can result [100]. Samples A and A' could not be etched by the slow etchant described above. When the fast etchant was employed for 30 min, circular etch pits were observed on the surface of samples A and A' as shown in the optical micrographs of Figure 6.5. No step could be detected between the etched surface and the masked area. However, after anodic oxidation and stripping, both samples A and A' etched in the normal manner, i.e., rapidly and uniformly. This result is a clear indication that the Si etch is inhibited by the presence of the surface contamination layer. The correlation between the carbonaceous layer and etch inhibition is further illustrated by the Auger elemental maps shown in Figure 6.6. An absorbed current micrograph (Fig. 6.6a) serves to indicate the location of etch pits such as those shown in Fig. 6.5. The edge of the speciment is indicated by the bright line across the upper right hand region of the photograph. Figure 6.6b shows a carbon Auger image taken after a 1 min sputter cleaning, sufficient to remove surface carbon contamination arising from exposure to air. Dark areas correspond to regions where carbon is absent from the surface being analyzed. Figure 6.6c shows a silicon Auger image for the same region shown in Figs. 6.6a and b. Silicon is visible in the etch

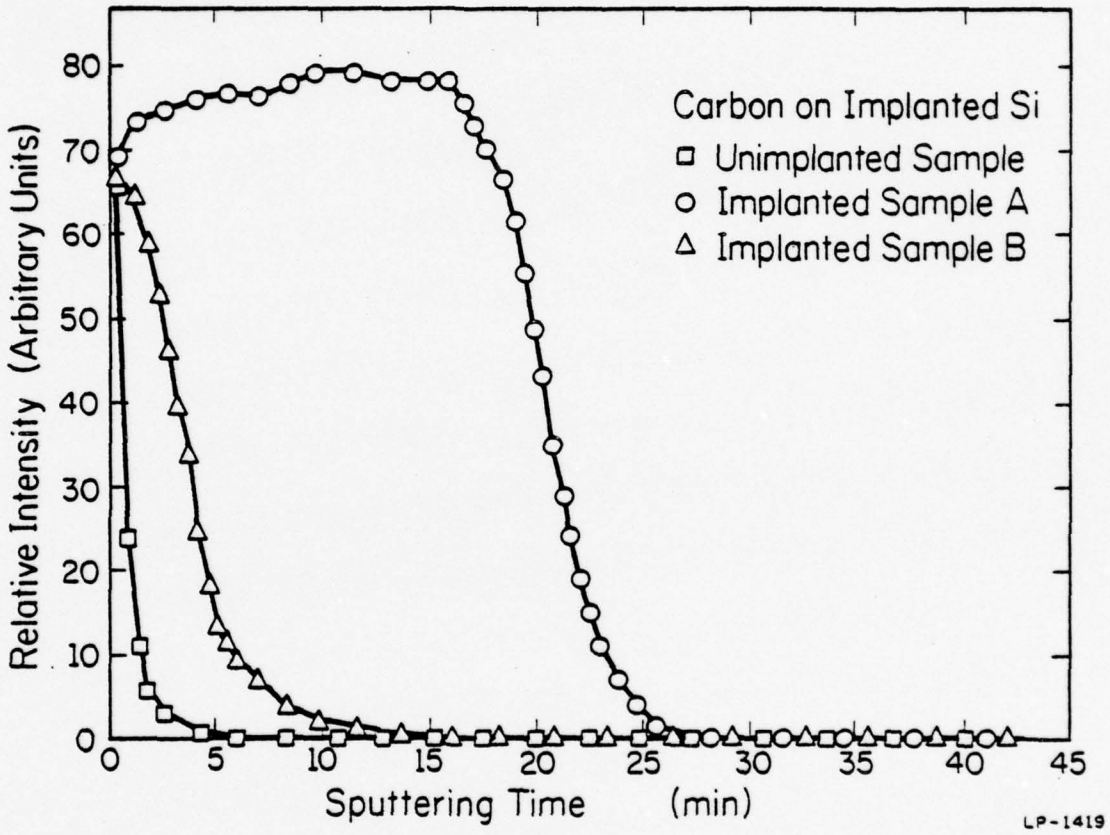

Fig. 6.4. Comparison of AES depth profiles for samples implanted with different diffusion pump fluids used in the target chamber vacuum system. Si^+ implantation at ~ -110°C was performed to a total fluence of ~ 8×10^{15} cm^{-2} for both samples. However, sample A was implanted using conventional diffusion pump oil and sample B was implanted after perfluorinated polyether fluid was substituted in the target chamber vacuum system.

(a)

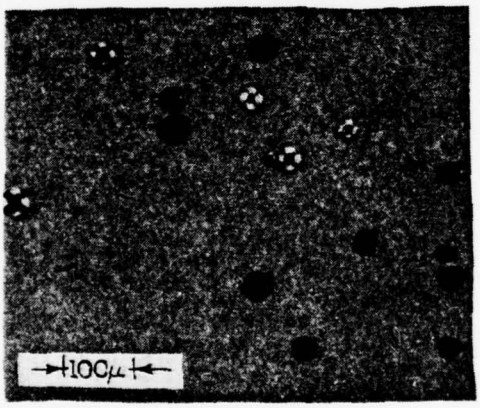

(b)

Fig. 6.5. Optical micrographs of circular etch pits on samples A and A′ etched in fast planar silicon etchant for 30 min: (a) sample A (implanted at ~ -100°C) (b) sample A′ (implanted at room temperature).

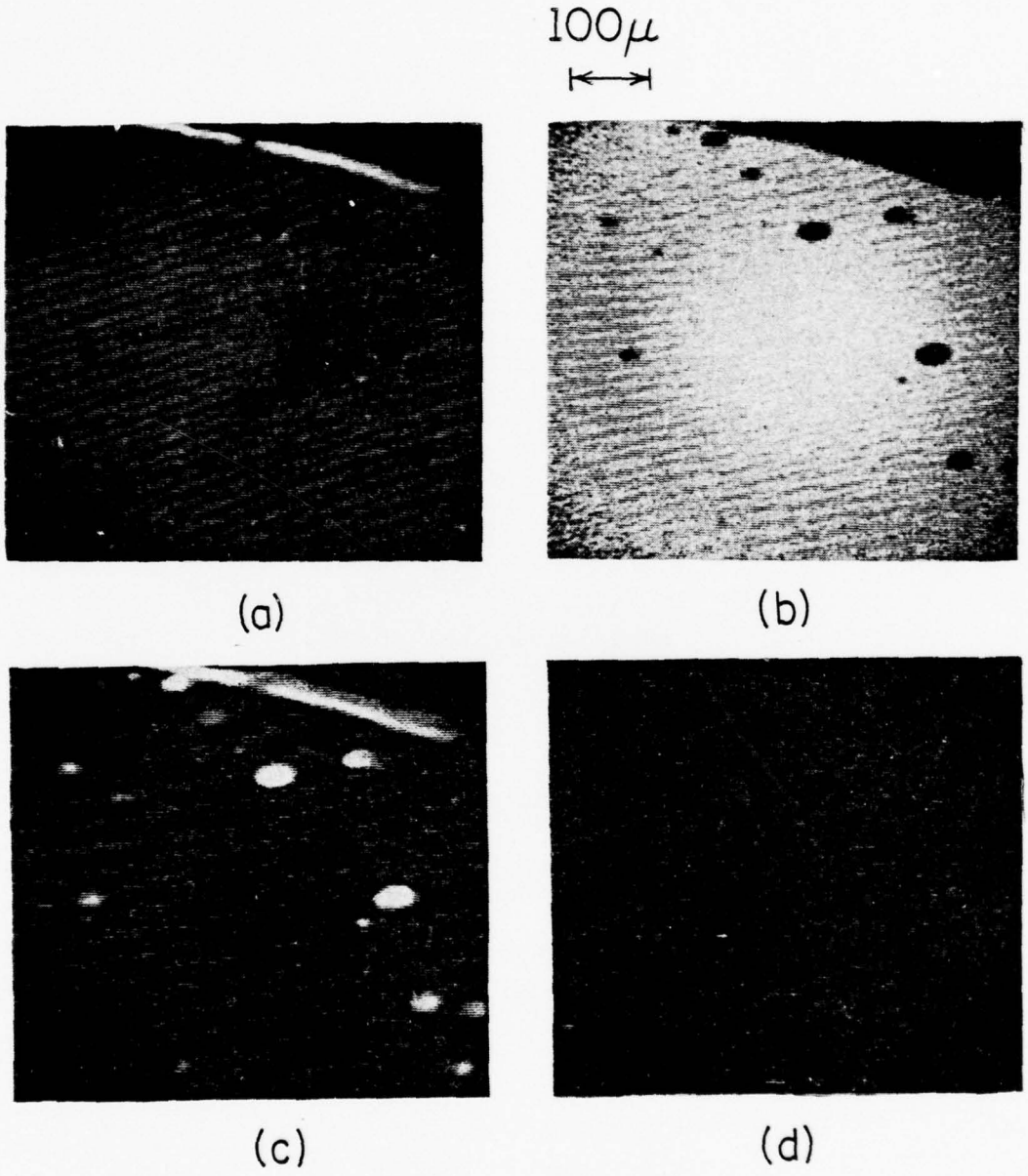

Fig. 6.6. Micrographs taken from sample A using the scanning Auger microprobe in the following Z-modulation modes: (a) absorbed current; (b) carbon Auger signal (272 eV); (c) silicon Auger signal (92 eV); (d) carbon Auger signal (272 eV), after sputter removal of the contamination layer. The magnification is 100X and the primary electron incident angle is 30°.

pits and along the cleaved edge of the sample. This sample was depth profiled through the carbon layer in the usual manner, giving results similar to those shown in Fig. 6.1. After the carbon layer was sputtered away, another carbon image (Fig. 6.6d) was taken from the same area shown in Fig. 6.6b. No carbon was detected in this case, although the pits could still be seen in an absorbed current micrograph (not shown). Only those regions where the contamination layer is sufficiently thin or porous will be penetrated by the etch solution. For this reason the number of etch pits is greater on sample A' than on sample A. Figure 6.7 shows an optical micrograph of sample B after a 10 min partially masked etch in the slow Si etch solution. The presence of a clear etch step at the mask edge and a uniformly etched surface illustrate the elimination of the contamination problem.

Additional evidence of pump oil polymerization and its elimination is found from I-V curves measured between electrical contacts evaporated onto sample A and sample B with the additional B^+ implants described in the previous section. It is clear (Fig. 6.8) that the contamination layer on sample A has an adverse effect on ohmic contact formation. Even after sample A had been sintered under flowing hydrogen at $300^{\circ}C$ for 1 min, the I-V characteristics did not improve. In contrast, sample B, without any heat treatment, exhibits good ohmic behavior.

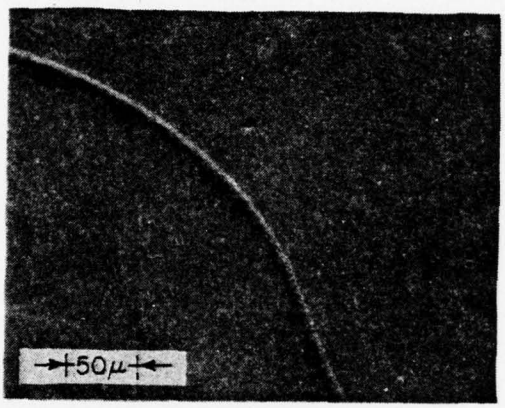

Fig. 6.7. Optical micrograph of sample B etched in slow silicon etchant for 10 min. An etched step between the uniformly etched area (upper right) and the masked area (lower left) illustrates the uniformity of the etching.

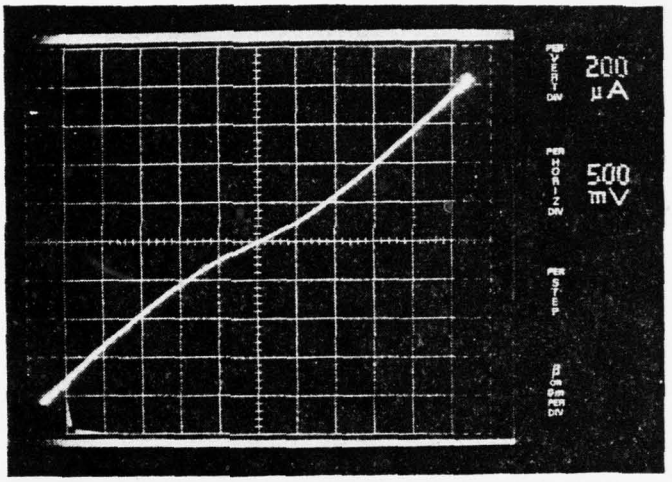

(a)

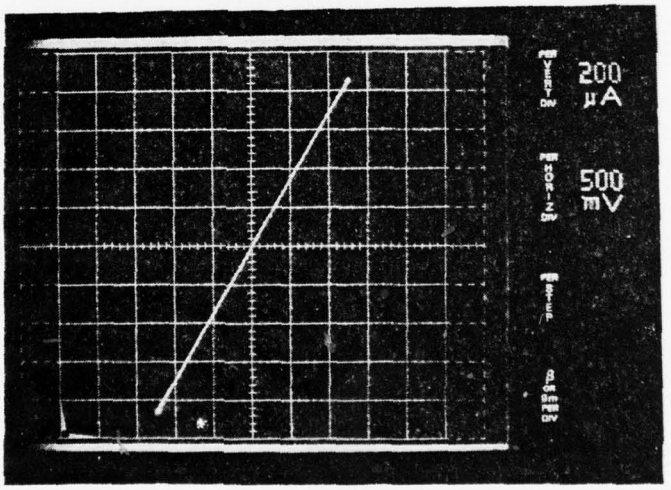

(b)

Fig. 6.8. Current-voltage measurements between Au pads on (a) sample A and (b) sample B, after an additional B^+ implant and anneal.

7. GALLIUM DISTRIBUTION AND ELECTRICAL ACTIVATION IN Ga^+-IMPLANTED Si

Although diffused gallium has been used successfully as an acceptor dopant in various silicon devices [101], its usefulness has been limited by its high diffusivity in SiO_2. This problem is avoided by using ion implantation, however, and gallium is now an attractive alternative to boron as a p-type dopant in a variety of Si devices. Ga^+-implanted resistors [102,103] and p^+n junctions [103,104] have previously been discussed; however, the understanding of Ga^+-implanted Si is rather limited. Early studies have led to contradictions over the existence of a penetrating tail after implantation [105,106,75]. Anomalous redistribution of Ga after annealing has also been observed [83]. These results make the acceptor distribution in Ga-implanted Si difficult to predict. The electrical activation of Ga has been discussed briefly in several early papers [40,75,107], but carrier concentration profiles have not been studied in detail.

Since boron inside an implanted amorphous layer is fully activated by recrystallization at low temperature ($\sim 550^{\circ}C$, Chapter 4), it is interesting to know whether Ga can also be activated fully by recrystallization at these temperatures. The critical dose of Ga^+ to form an amorphous Si layer at room temperature is $\sim 2.5 \times 10^{14}$ cm^{-2} (Table 3.1), which is much lower than for B^+ implants ($> 2 \times 10^{16}$ cm^{-2}) [30]. Hence, Ga^+ implantation can result in an amorphous Si layer at room temperature with practical doses. No additional amorphizing F^+ or Si^+ implants are necessary, as in the case of B^+-implanted Si. In this respect,

Ga^+ implantation of Si is superior to B^+ implants when amorphization is required.

In this chapter, we have studied atomic Ga distributions by secondary ion mass spectrometry (SIMS) for as-implanted and annealed samples. We find no pronounced tail in as-implanted samples for Ga^+ fluences either below ($1x10^{14}cm^{-2}$) or above ($1x10^{15}cm^{-2}$) the critical fluence for amorphization. By comparing electrical carrier profiles with the SIMS atomic profiles, we find that redistribution and electrical activation of implanted Ga is affected by recrystallization, solid solubility, and ion damage.

7.1. Sample Preparation and Measurements

Phosphorus-doped 4-6Ω-cm ⟨100⟩ Si crystals were used throughout this work. Samples were implanted at room temperature with 200 keV $^{69}Ga^+$ to a fluence of $1x10^{15}$ cm^{-2} (sample 1) or $1x10^{14}$ cm^{-2} (sample 2) at room temperature. During implantation samples were tilted $\sim 7^{\circ}$ from the beam to minimize channeling effects. A copper heat sink was used to prevent heating of the samples. After implantation, anneals were performed under a continuous flow of forming gas.

Gallium atomic profiles were determined with an ion microprobe mass spectrometer (AEI Model IM 20). The Ga profiles were obtained by monitoring $^{69}Ga^+$ secondary ions produced by O^- primary ion bombardment. Details of the SIMS technique have been discussed in Section 2.5. The conversion from ion intensity ratio to gallium concentration was made by determining the ratio of the integrated $^{69}Ga^+$ signal to the implanted ion dose for an as-implanted sample. This conversion ratio was then used

to obtain gallium concentration profiles for samples after annealing. Crater depths were measured using an interference microscope to establish the sputtering rate and depth scale.

Sheet resistivity was measured by a four-point in-line probe for samples isochronally annealed from 400°C to 900°C with 10 minute annealing intervals. Differential resistivity and Hall effect measurements in conjunction with successive layer removal were used to obtain the detailed electrical carrier distribution. The double a.c. Hall effect system (using a van der Pauw configuration) and the layer removal techniques employed in this work have been discussed in Section 2.3. The ratio of Hall mobility to drift mobility was taken to be unity, for the convenience of comparing our results with other work [40,75,107].

The thickness of the amorphous layer in sample 1 was determined from the difference in etch rate of crystalline and amorphous Si in HF. From this etching experiment, an amorphous layer thickness of ~ 2050 Å was found on the surface of sample 1. In contrast, sample 2 (not amorphized by the implant) did not measurably etch in HF.

7.2. Gallium Distribution and Electrical Activation

Figures 7.1 and 7.2 show gallium atomic profiles for sample 1 ($1\times10^{15}cm^{-2}$) and sample 2 ($1\times10^{14}cm^{-2}$) respectively. Profiles for as-implanted samples and for samples annealed at 600°C or 900°C are shown on the same figure to illustrate the thermal diffusion during annealing. Both as-implanted samples (1 and 2) have profiles close to a perfect Gaussian distribution; no pronounced tails are observed. After these samples are annealed at 600°C, only a small amount of broadening due to

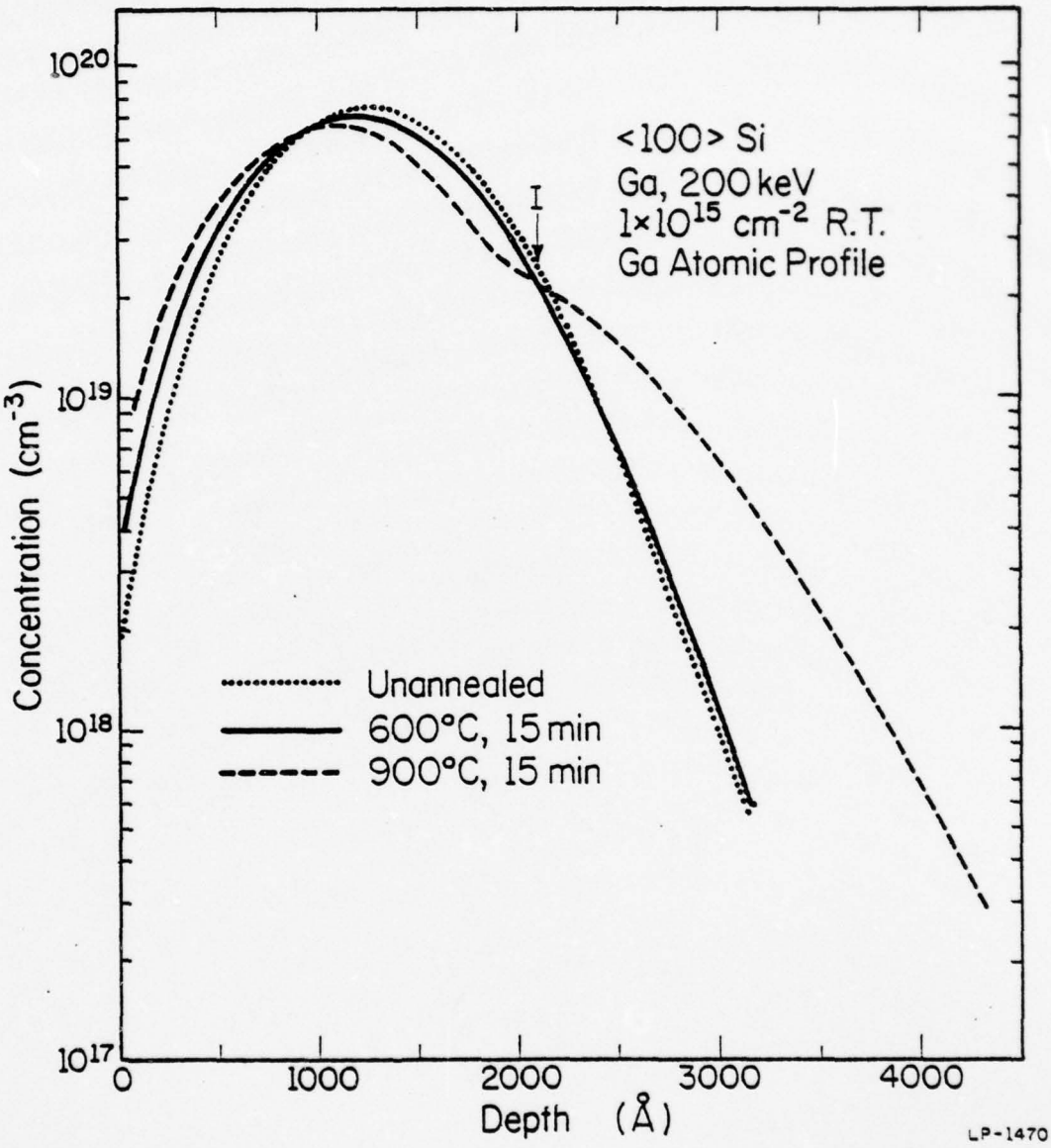

Fig. 7.1. Gallium atomic profiles obtained from SIMS measurements on ⟨100⟩ Si implanted at room temperature with a 1×10^{15} cm^{-2} fluence of Ga^+ (sample 1) and annealed for 15 minutes at the temperatures shown. The depth marked "I" represents the measured amorphous-crystalline interface after implantation.

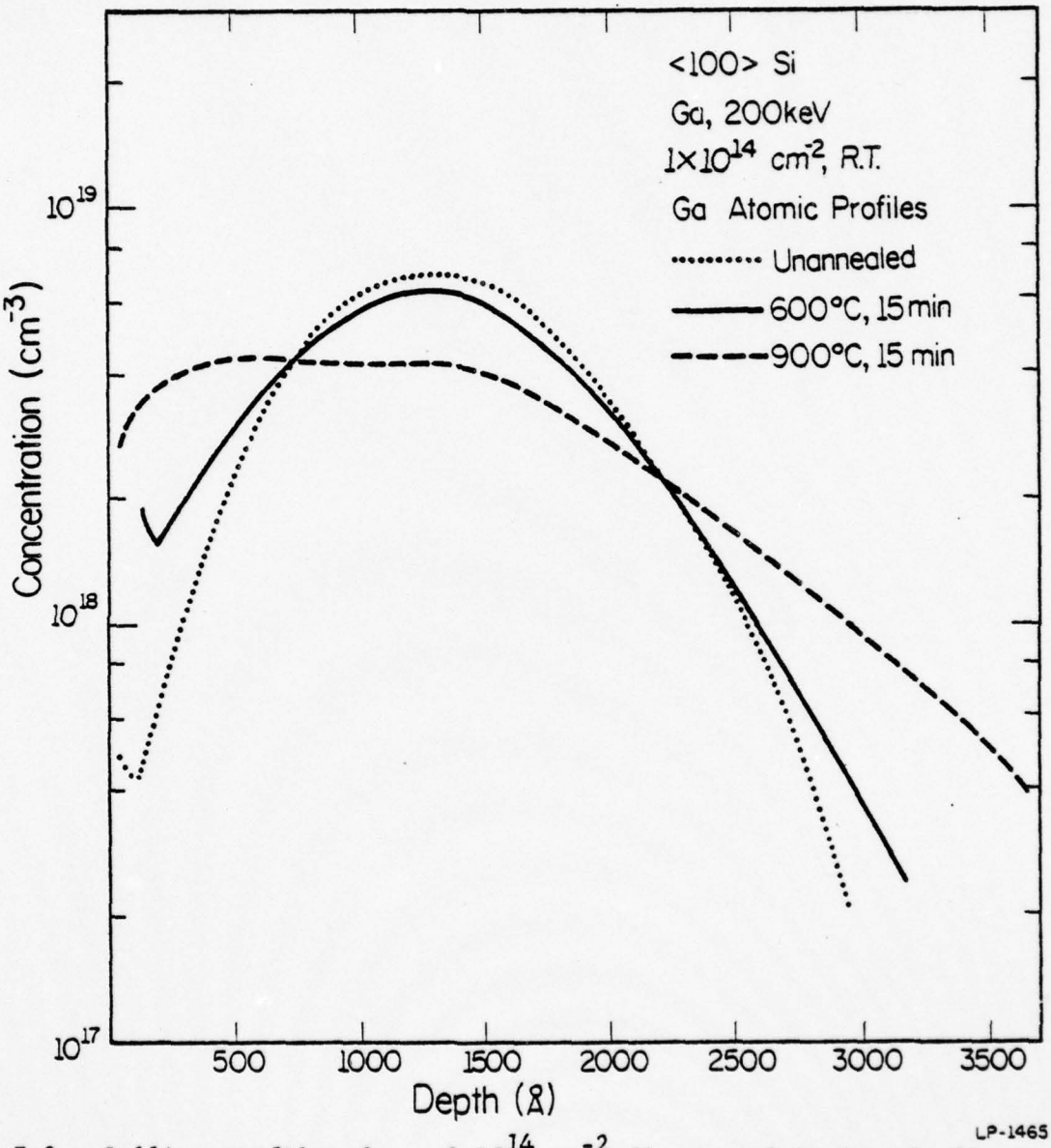

Fig. 7.2. Gallium profiles for a $1x10^{14}$ cm^{-2} fluence of Ga (sample 2) after implantation and after annealing at the indicated temperatures.

thermal diffusion is observed. However, samples 1 and 2 differ greatly in their Ga distribution after the 900°C anneal.

There is an amorphous layer on the surface of sample 1 after implantation. The amorphous-crystalline interface at 2050 Å is denoted by I in Fig. 7.1. There is also a heavily damaged crystalline Si region below I, which is commonly observed in samples having an implanted amorphized layer [27,78]. The measured Ga profile after 900°C anneal clearly indicates the diffusion in the recrystallized amorphous layer (above I) is different from that in the damaged crystalline Si (below I). The diffusivity for Ga in Si at 900°C is $\sim 4\times10^{-15}$ cm^2sec^{-1} [108]. If a normal thermal diffusion of the implanted distribution were to occur in sample 1, the 900°C diffused Gaussian would have a standard deviation only about 10% larger than the as-implanted profile. The measured 900°C profile within the recrystallized region (Fig. 7.1) appears to be the result of such moderate diffusion. However, in the tail region of the profile (below I) the diffusion of Ga is much more pronounced, resulting in a shoulder on the distribution. The Ga diffusivity in the tail region is estimated to be $\sim 4\times10^{-14}$ cm^2sec^{-1}, a decade larger than expected in undamaged Si. This increase is apparently due to defect-enhanced diffusion in the heavily damaged region below I.

In sample 2 (Fig. 7.2), the implanted dose is below that required for formation of an amorphous Si layer. Therefore, the most heavily damaged region exists between the surface and the implanted peak, as indicated by an energy deposition (or damage) calculation [62]. The defect-enhanced diffusion observed in Fig. 7.1 apparently accounts also for the deep diffused tail and the accumulation of Ga in the damaged region near the surface after the 900°C anneal in Fig. 7.2.

To examine the electrical activation of the implanted gallium, the results of sheet resistivity (R_s) measurements for samples 1 and 2 are shown in Fig. 7.3 as a function of isochronal annealing. Similar results for a sample implanted with relatively low dose ($2x10^{13}cm^{-2}$) is also included. The sheet resistivity of the low-dose ($2x10^{13}cm^{-2}$) and medium-dose ($1x10^{14}cm^{-2}$) samples decreases monotonically with increasing anneal temperature. Similar sheet resistivity curves have been observed for P^+ or As^+-implanted Si with doses below the critical dose for amorphous Si layer formation [109]. The high-dose ($1x10^{15}cm^{-2}$) sample 1 has a sharp annealing stage at 500°-600°C which is characteristic of implanted amorphous Si [1,74]. The reverse annealing stage (R_s increasing with annealing temperature) for sample 1 annealed at 700°C is evidence of a decrease in Ga activation (to be discussed below).

Figure 7.4 shows the electrical carrier and mobility profiles of sample 1 after recrystallization at 600°C. The corresponding atomic profile from Fig. 7.1 is also superimposed for comparison. Evidently, recrystallization of the amorphized layer almost fully activates Ga atoms inside the regrown region (outside I). However, the mobility inside the recrystallized layer is much lower than typical values given by Irvin [81] for bulk Si with equivalent concentrations. This degradation of mobility indicates that some damage still exists inside the recrystallized layer. In the heavily damaged crystalline region (below I), an unactivated tail is observed (shown as a shaded area in Fig. 7.4). This result is similar to the inactive tail reported by BF_2^+-implanted silicon in Chapter 3.

The carrier and mobility profiles for sample 1 annealed at 900°C for 15 minutes are shown in Fig. 7.5. The peak concentration of carriers

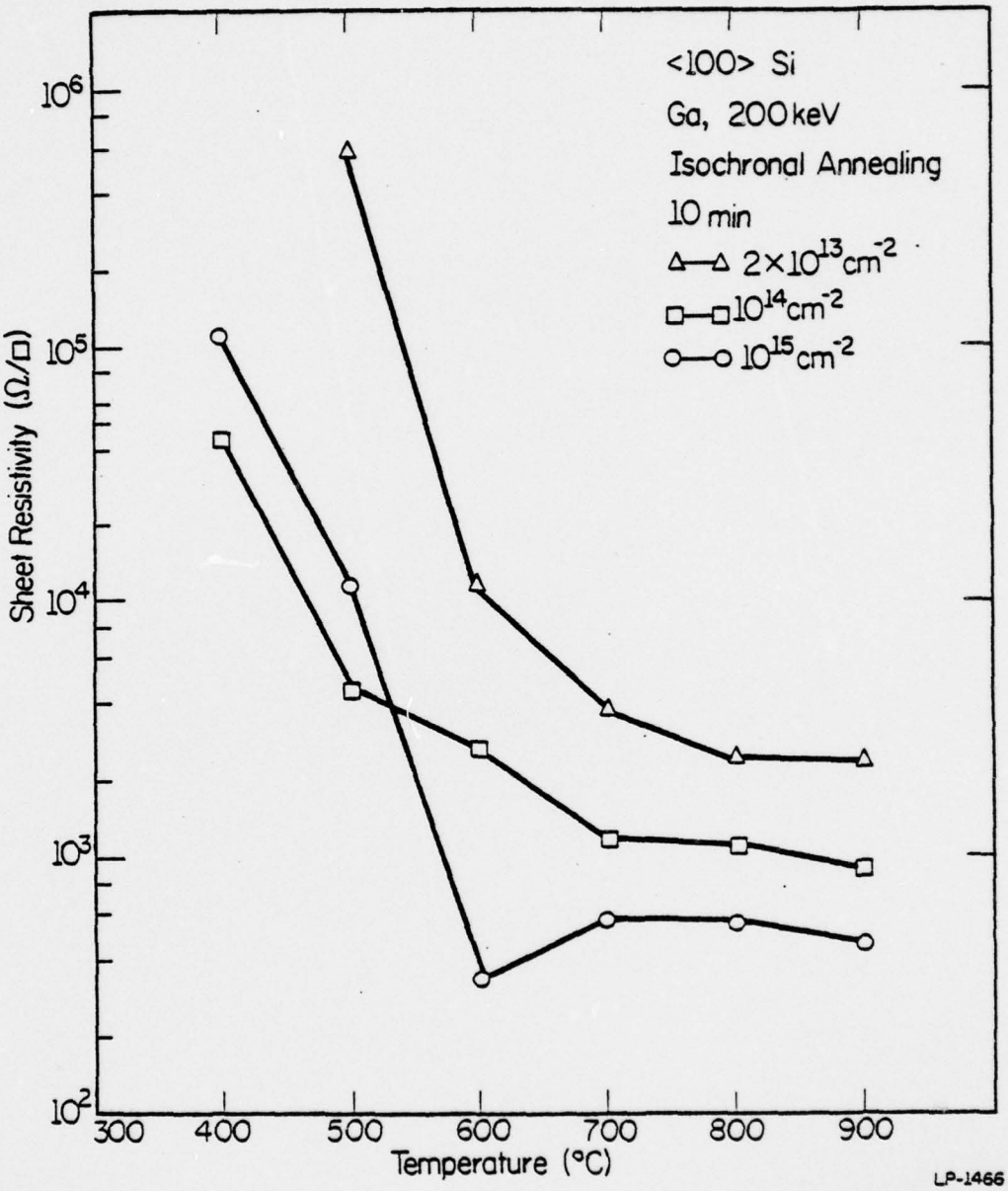

Fig. 7.3. Sheet resistivity measured by 4-point probe on sample 1, sample 2, and a lightly implanted (2×10^{13} cm^{-2}) sample, isochronally annealed for 10 minute intervals at the temperatures shown.

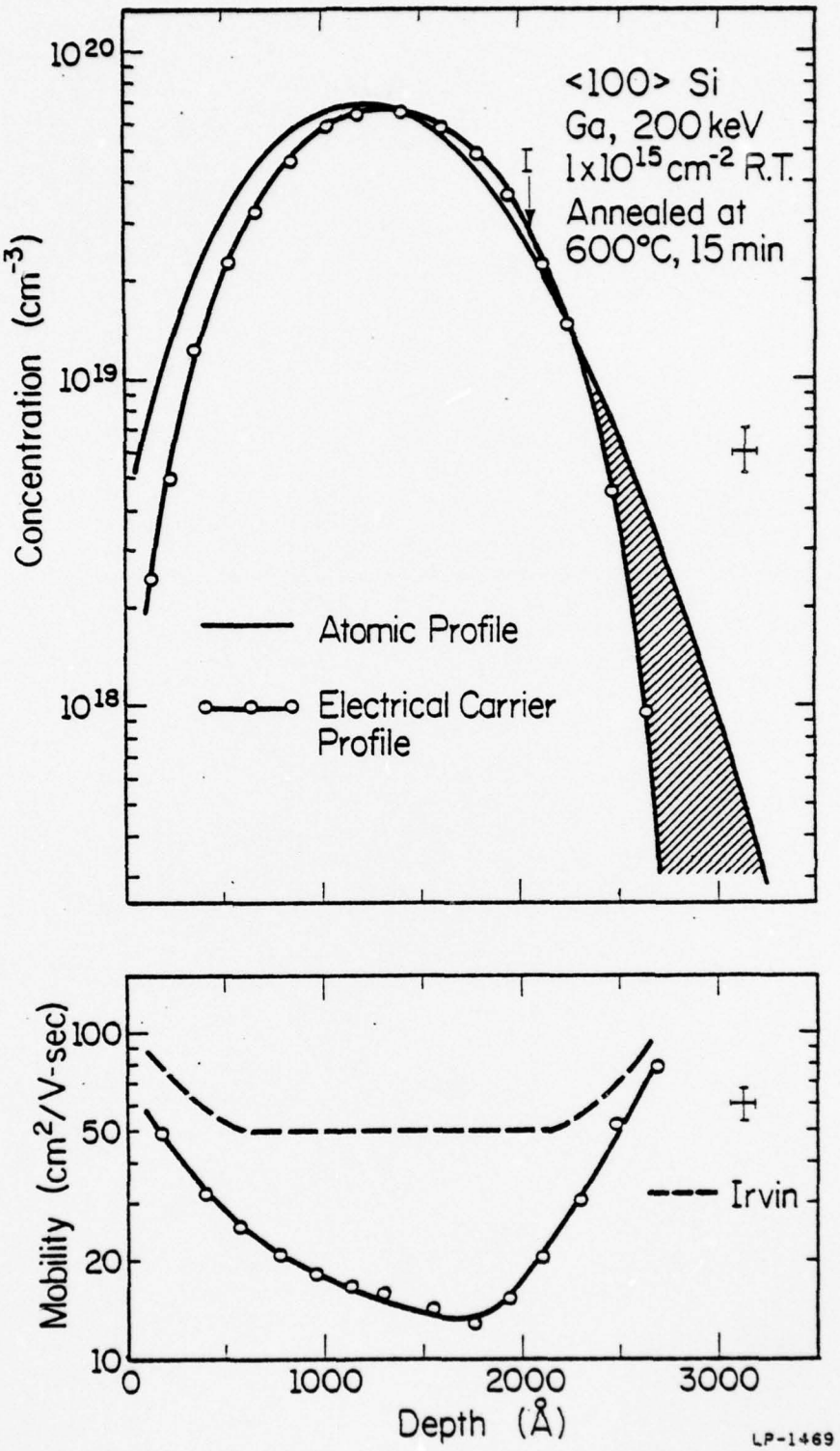

Fig. 7.4. Net acceptor concentration and mobility profiles for sample 1 ($1x10^{15}$ cm^{-2} Ga^{+}) after an anneal at 600°C for 15 minutes. The corresponding atomic profile (from Fig.7.1)is also shown. The shaded area indicates the electrically inactive tail of the Ga distribution below the original amorphous-crystalline interface I. The mobility data are compared with typical mobility values for bulk Si from Irvin [81].

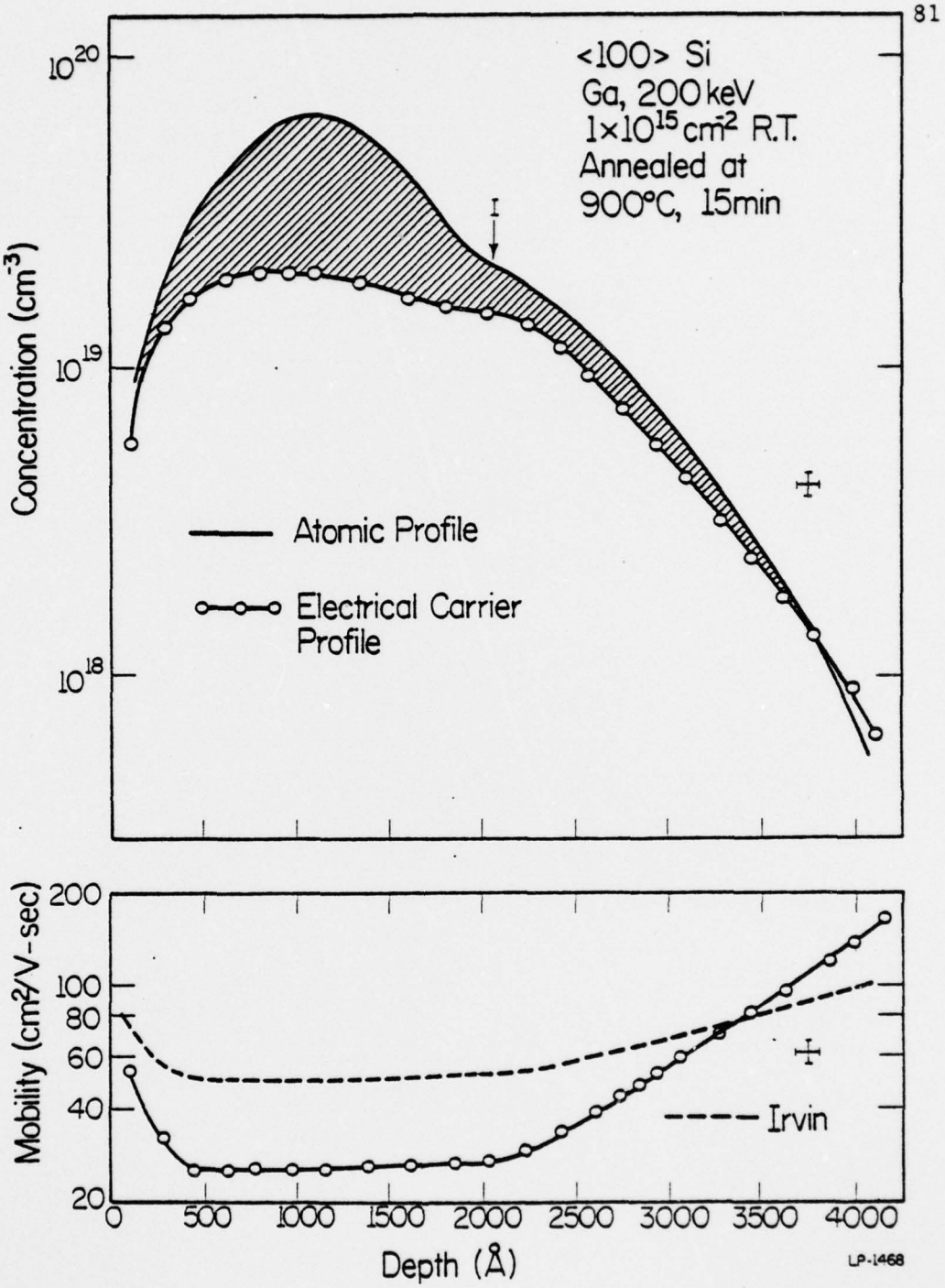

Fig. 7.5. Net acceptor concentration and mobility profiles for sample 1 ($1x10^{15}$ cm^{-2} Ga^+) annealed at 900°C for 15 minutes. The atomic profile (from Fig.7.1)is also shown. The shaded area indicates electrically inactive Ga over much of the profile. Mobility data are compared with Irvin's bulk silicon mobility values.

is 2×10^{19} cm^{-3}, which is much lower than the Ga atomic concentration and represents a pronounced drop in the Ga activation as compared to the 600°C anneal (Fig. 7.4). Interestingly, the solid solubility of Ga in Si at 900°C is also approximately 2×10^{19} cm^{-3} [82]. Thus, the solid solubility appears to limit the activation of Ga, and the excess gallium seems to lower the mobility. Except for some carrier compensation near the original amorphous-crystalline interface (I), the diffused tail region is fully activated and exhibits good mobility.

It is also interesting to examine the carrier concentration after 900°C annealing for sample 2, which was not amorphized by the implant (Fig. 7.6). A shaded region indicates the difference between the measured atomic Ga profile and the acceptor distribution. The discrepancy in this case is not due to the solid solubility limitation, which is $\sim 2 \times 10^{19}$ cm^{-3}. Instead, there is apparently considerable residual damage which prevents full activation of the Ga. It is clear that good electrical activation over most of the profile is obtained by recrystallization of an amorphous layer (Fig. 7.4), but that much of the damage in a non-amorphizing implant is not annealed even at 900°C (Fig. 7.6).

7.3. Conclusions Regarding Ga^+-Implanted Si

The results presented here lead us to some interesting conclusions regarding Ga-implanted Si:

(1) Within the limitation of the $^{69}Ga^+$ detection by our ion microprobe, no penetrating tails are observed prior to annealing for either amorphizing ($10^{15} cm^{-2}$) or non-amorphizing ($10^{14} cm^{-2}$) implants. This result agrees with the observation by Gamo et al. [105] that implanted Ga

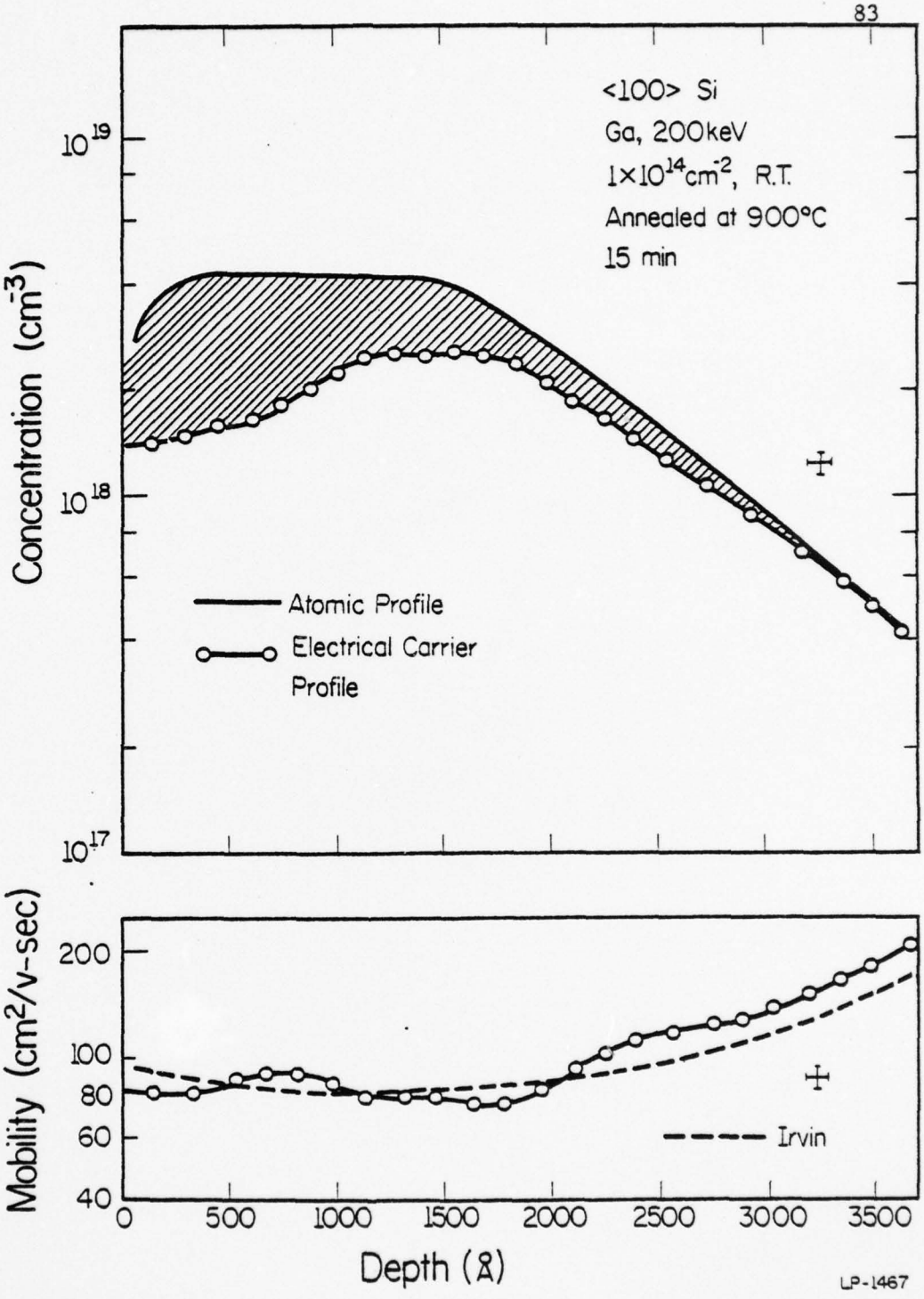

Fig. 7.6. Net acceptor and mobility profiles for sample 2 ($1x10^{14}$ cm^{-2} Ga^+) after annealing at 900°C for 15 minutes. The atomic profile (from Fig. 2) is also shown. The shaded area indicates electrically inactive Ga atoms over much of the profile. Mobility data are compared with bulk silicon mobility values.

profiles are essentially Gaussian. The tail observed by Crowder [75] in a sample corresponding to our sample 1 was apparently due to other effects, as suggested in his paper. Dearnaley et al. [106] have argued that the channeling effect will cause a tail in low-dose ($1x10^{13}cm^{-2}$) Ga^+ implants. Our results indicate, however, that doses of 10^{14} cm^{-2} or higher result in essentially Gaussian distributions before annealing. Perhaps the disorder created by a 10^{14} cm^{-2} Ga implant is sufficient to prevent significant channeling. Our results do not address the question of whether the enhanced diffusion mechanism [105] or the channeling effect [106] is responsible for penetrating tails observed in high temperature Ga^+ implantation [105]. Such high-temperature implantation has been found to create considerable damage which is resistant to annealing [26,95]. It is therefore not likely to be used in common applications.

(2) Anomalous gallium diffusion in Ga^+-implanted Si is related to recrystallization of the amorphous layer and ion damage in crystalline Si (Figs. 7.1 and 7.2). We speculate that defect-enhanced diffusion at 900^oC is the cause of pronounced tails in samples 1 and 2, and accumulation near the surface in sample 2.

(3) Using an amorphizing Ga implant, it is possible to achieve electrically active acceptor concentrations above the Ga solubility limit by recrystallization at 600^oC. The solid solubility of Ga in Si at 600^oC is not shown in Trumbore's [82] curve, but it should be lower than the 700^oC value of 10^{19} cm^{-2}. The active carrier concentration for sample 1 annealed at 600^oC is obviously higher than this value (Fig. 7.4). Similar oversaturation has been observed for Sb^+-implanted Si annealed at 600^oC [107]. Although the advantage of high carrier concentration in Fig. 7.4 is

compensated somewhat by low mobility, a significantly improved sheet resistance is achieved (Fig. 7.3). It is important to note that this oversaturation is related to recrystallization of the amorphous layer. For a Si sample implanted with 10^{15} cm^{-2} Ga^{+} at 500°C (where no amorphized layer is formed), the reported [110] activation of Ga at 600°C is only about 5% of that shown in Fig. 7.4.

(4) After sample 1 is annealed at 900°C, the peak carrier concentration drops to $\sim 2x10^{19}$ cm^{-3}, which is the solid solubility value at 900° [82]. This level of electrical activity agrees with previous observations in Ga-implanted Si annealed at this temperature [40]. The decrease in Ga activation upon annealing above the recrystallization temperature is reflected also in the sheet resistance as a reverse annealing stage (Fig. 7.3).

(5) Even when the Ga atomic concentration is lower than the solid solubility, full activation of the Ga atoms is not achieved after 900°C annealing. This is evident from comparison of the acceptor concentration profile with the atomic Ga distribution in Fig. 7.6. There is also reduced Ga activation near I in Fig. 7.5, in which the net acceptor concentration falls below the $2x10^{19}$ cm^{-3} value expected from the solid solubility effect. These cases of reduced activation reflect regions of residual damage after annealing, and are undoubtedly due to a combination of non-substitutional Ga (including Ga-defect complexes) and compensation of Ga acceptors by other defects. The diffused tails in Figs. 7.5 and 7.6 are outside the regions of implantation-induced damage and exhibit good activation and high mobility.

AD-A069 779 ILLINOIS UNIV AT URBANA-CHAMPAIGN COORDINATED SCIENCE LAB F/G 20/2
STUDIES OF HIGH-DOSE ION IMPLANTATION IN SILICON.(U)
SEP 78 M Y TSAI DAAB07-72-C-0259
UNCLASSIFIED R-824 NL

2 OF 2
AD
A069779

END
DATE
FILMED
7-79
DDC

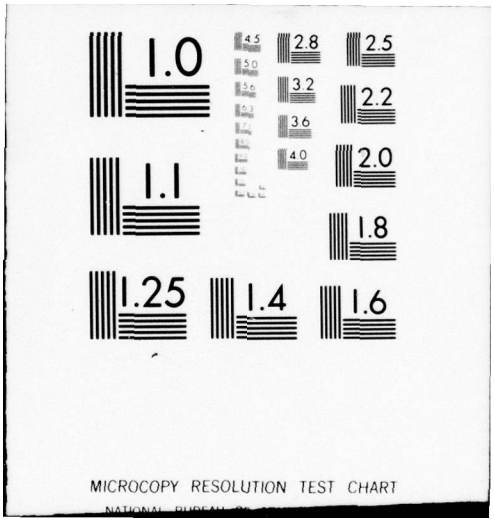
1.0
1.1
1.25
1.4
1.6
1.8
2.0
2.2
2.5
2.8
3.2
3.6
4.0
4.5
5.0
5.6
MICROCOPY RESOLUTION TEST CHART

(6) Implanted Ga is promising for device applications requiring shallow p^+ regions. By annealing heavily implanted samples near the Si recrystallization temperature ($\sim$ 550-600°C), high acceptor concentrations can be achieved with negligible thermal diffusion (Fig. 7.4). As is the case for BF_2^+ implants, however, an inactive region lies below the original amorphous-crystalline interface (I) after recrystallization.

8. STUDIES OF RESIDUAL DAMAGE

It is well known that ion-implanted crystals will contain a great deal of damage [111,112]. Especially in high-dose implanted Si, an amorphous Si layer can be created as discussed in Chapter 3. During annealing, the implanted dopants, such as B and Ga, are incorporated into electrically active sites and the mobility recovered close to bulk value (Chapters 4 and 7). However, more detailed studies of residual damage in high-dose implanted Si after annealing are necessary for high quality device applications. The crystallographic imperfection has been studied by aligned backscattering [25,26] and transmission electron microscopy [27,28]. The electrical effects of residual damage in the recrystallized amorphous Si sample have never been thoroughly studied, however. This chapter is devoted to the studies of electrical properties of residual damage.

The most important electrical effects of defects are the creation of deep levels in the silicon band gap, which serve as carrier traps or recombination centers. These defects will affect the reverse leakage current of p-n junctions, the quantum efficiency of light-emitting diodes, and charge transfer efficiency in surface devices such as CCDS. Almost all of the earlier data about deep level defects were obtained on uniform samples from the temperature dependence of the Hall effect and electrical conductivity [113] and from infrared spectroscopy [114]. The Hall effect and conductivity measurements are tedious and require variation of temperature from that of liquid helium to near room temperature. The accuracy is limited by uncertainties in the theoretical model of bound

electron or hole states in semiconductors, such as the unknown excited states and energy level degeneracy levels. Infrared spectra measurements suffer similar limitations and can only detect radiative levels. Recently, transient capacitance measurement techniques have been developed in conjunction with thermally stimulated currents and photoconductivity to provide information on electrical properties of deep-level impurities and defects [116,117]. The most powerful transient capacitance technique, called deep level transient spectroscopy (DLTS) [118], has been used in this work for the studies of residual damage in ion-implanted silicon. Some reverse bias leakage currents for p-n junctions are also measured to provide additional information about residual damage.

8.1. Deep Level Transient Spectroscopy (DLTS)

DLTS is a capacitance transient thermal scanning technique which has high sensitivity and speed, a wide range of observable trap depths, and the advantage of detecting nonradiative centers. The principles of DLTS and the apparatus used in this work will be briefly discussed here.

8.1.1. Pulsed Bias Capacitance Transients

The use of capacitance transients for trap studies in semiconductors is well known [116,117,120]. This technique is used to obtain information about an impurity level in the depletion region of a Schottky barrier or p-n junction. Following an initial nonequilibrium condition, one observes the capacitance transient associated with the return to thermal equilibrium of the occupation of the level. In DLTS this initial nonequilibrium condition is achieved by using voltage pulses [118,119]. A p-n asymmetric diode is used to illustrate the capacitance transient,

although the same results hold as well for an n^+ p junction, with appropriate changes of notation. Figures 8.1 and 8.2 show graphically the relation between the time evolution of the junction capacitance and defect charge states.

Defect levels can be divided roughly into two categories, depending on their location in the forbidden gap. In the space charge region of a reverse-biased diode, where thermal emission rates determine equilibrium, such levels tend to be empty of electrons. Such levels are called "majority carrier traps," since during a voltage pulse which reduces the reverse bias they tend to trap majority carriers (electrons). As shown in Figure 8.1, these majority carrier traps give rise to a negative capacitance transient after a majority carrier pulse.

The second category of levels shown in Figure 8.2 are "minority carrier traps" since they tend to be full of electrons in the space charge region and able to capture minority carriers during a voltage pulse which drives the diode into forward bias and injects holes (injection pulse). Such levels tend to be in the lower half of the gap in n-type material. As shown in Figure 8.2, a minority carrier trap gives rise to a positive capacitance transient after an injection pulse.

All of the capture and emission properties of a particular level may be determined from observation of the related capacitance transient. The trapped carrier emission rate (e) is simply the inverse of the transient time constant (τ). Thus the activation energy for emission may be determined from the temperature dependence of this time constant by plotting the log of the emission rate versus the inverse temperature (with appropriate corrections for the T^2 dependence of the prefactor to

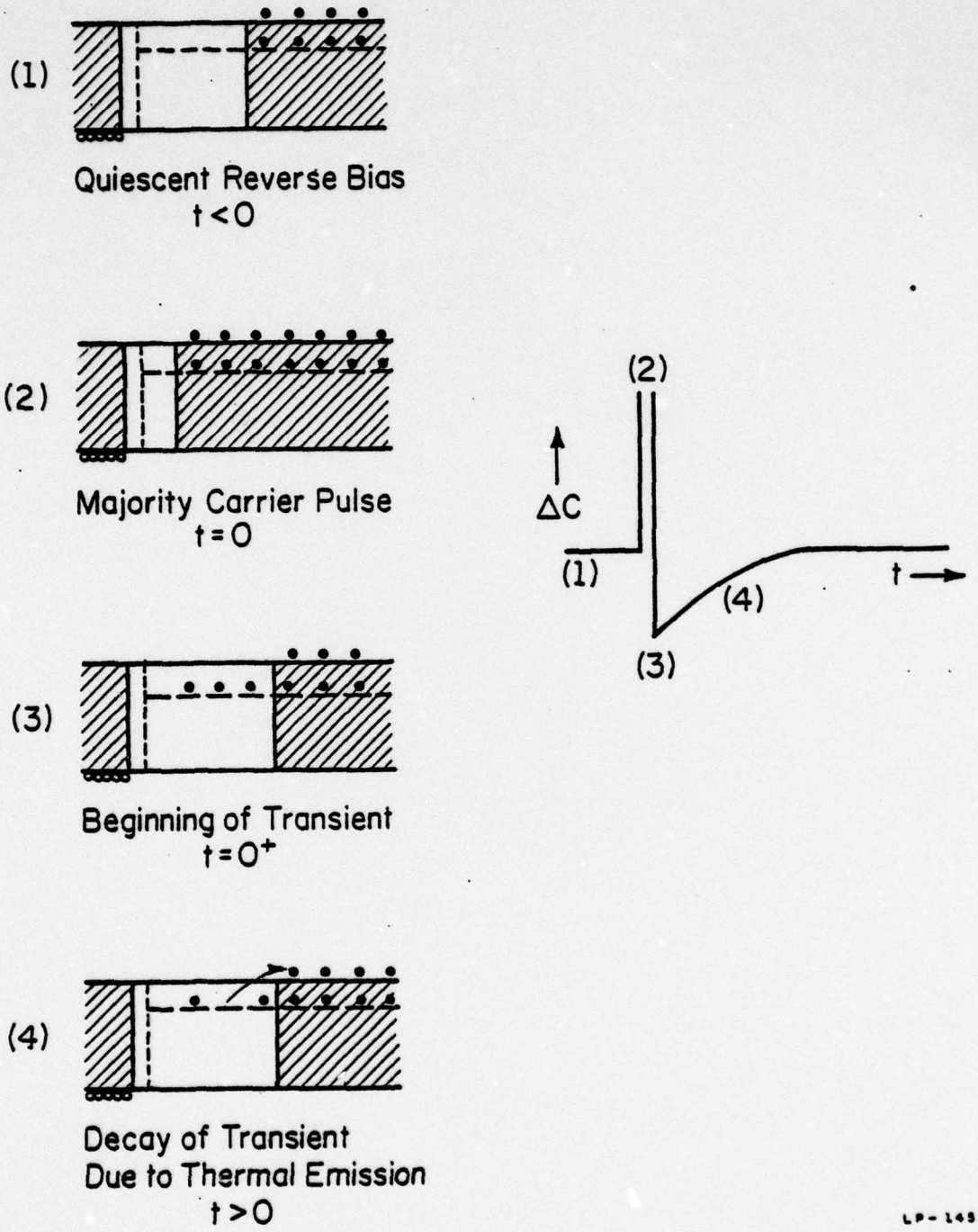

Fig. 8.1. Capacitance transient due to a majority carrier trap in a p^+-n diode. The insets labeled 1 through 4 schematically show the charge state of the defect level and width of the space charge region (unshaded portion) at various times before and during the transient. (Lang [118])

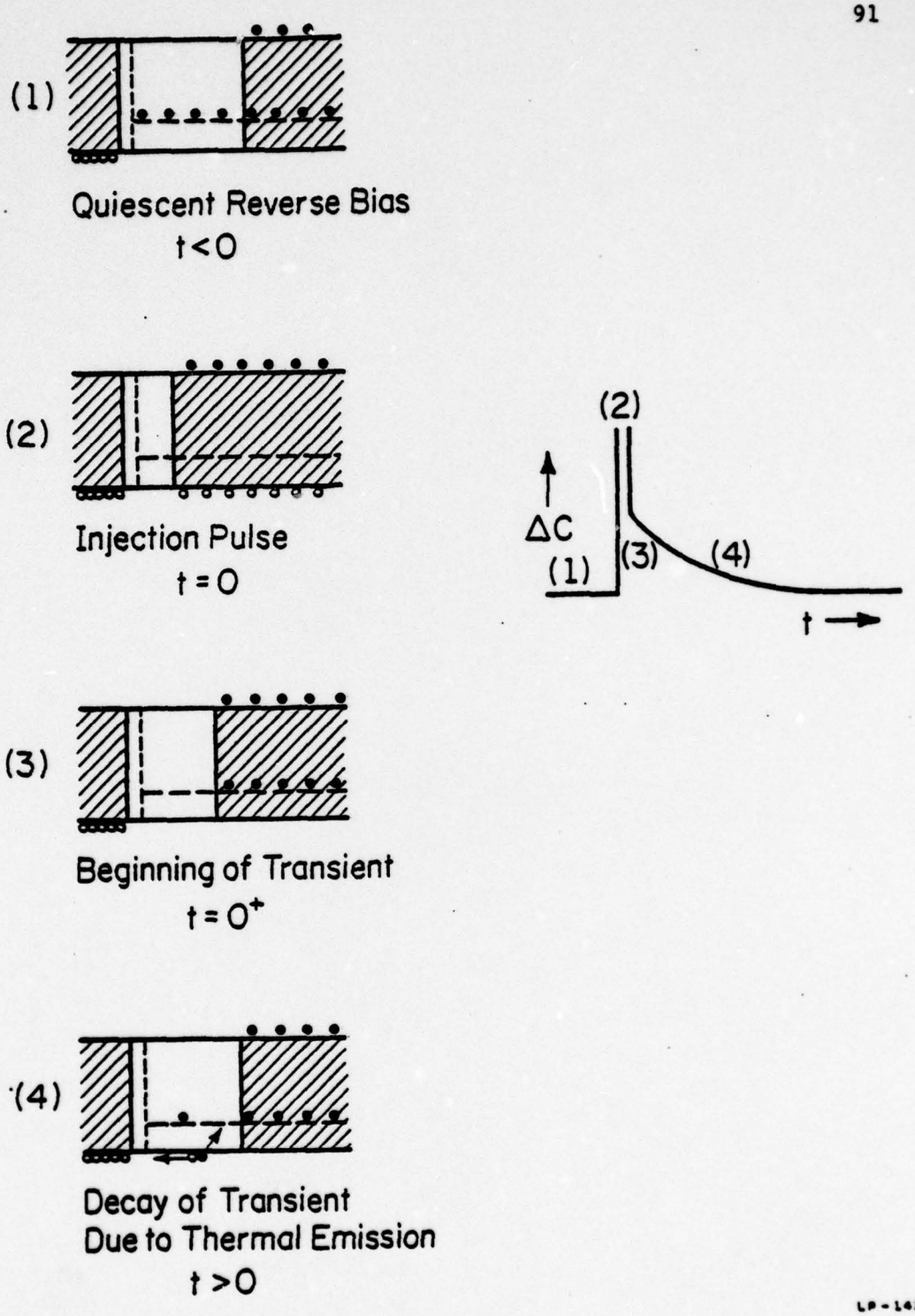

Fig. 8.2. Capacitance transient due to a minority carrier trap in a p^+-n diode. (Lang [118])

the exponential). The capture cross sections for holes and electrons can be determined from the dependence of the transient amplitude on the width of the bias pulse, as shown by Henry et al. [121]. The concentration of defects is given by the amplitude of the transient for those conditions where the pusle is long enough to completely fill all states of the defect [116]. If the concentration of the defect centers (N_T) is much smaller than the concentration of the majority doping impurity (N_{DD}), the relation between the amplitude of transient capacitance ΔC and quiescent capacitance C is

$$\frac{\Delta C}{C} = \frac{N_T}{2N_{DD}} \tag{8.1}$$

8.1.2. DLTS Methods

The DLTS method makes it possible to process the information inherent in capacitance transients in such a way as to present a spectrum defect levels. This allows rapid measurement, even of complicated systems with many defect levels such as residual damage in implanted Si. The key to the DLTS scheme is the rate window concept [118]. Basically, one employs a detection system which is tuned to respond only a repetitive transient having a particular time constant. As the temperature is varied, the emission rate of a defect level changes accordingly. Thus at a certain temperature the emission rate equals the tuned rate window, and a maximum response is registered (Fig. 8.3). Thus a spectrum of defect levels can be obtained as a function of temperature. Changing the rate window to lower (higher) rates shifts the spectrum to lower (higher) temperatures and enables one to construct an Arrhenius plot of emission rate versus inverse temperature from which the activation energies for emission may be determined. Majority carrier traps give negative transients and thus negative peaks; conversely,

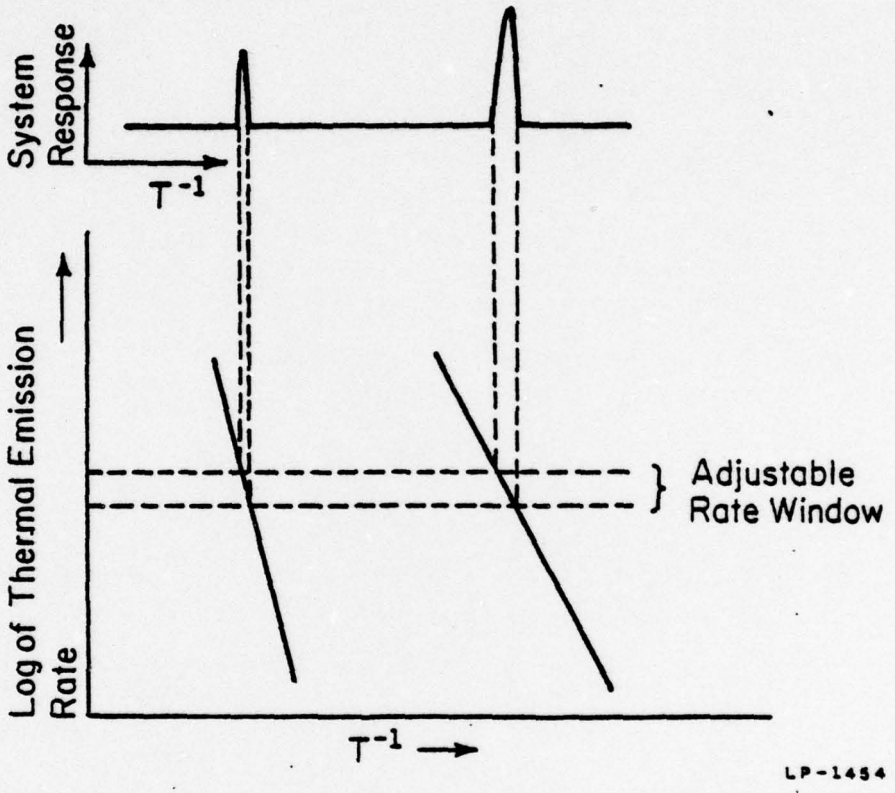

Fig. 8.3. The DLTS rate window concept. The lower half of the figure shows the typical temperature dependence of the emission rate of carriers of a sample with two defect levels. The upper half shows how the system response passes through a maximum whenever the temperature is such that the emission rate of a particular trap is within the preset rate window. (Lang [118])

minority carrier traps give positive peaks.

The rate window has been achieved in this work by either a lock-in amplifier or a dual gated boxcar integrator. Detailed description of the systems and the data analysis are presented in the following.

8.1.3. Experimental Apparatus

The block diagram of the DLTS system used in this work is shown in Fig. 8.4. The pulsed bias is generated by a precision power supply and a pulse generator. The pulse can be coupled to the diode through a pulse transformer as shown in Fig. 8.4. Another method is to connect the pulse generator output to the "low" side of the capacitance meter's bias terminal, and provide a constant voltage at the "high" side. Both circuits result in pulsed bias of the testing diode (Fig. 8.5a). If there is a majority carrier trap, the transient signal from the capacitance meter appears as shown in Fig. 8.5b. Since the signal during the pulse contains no important information and normally overflows the lock-in amplifier and boxcar integrator, a sample-and-hold circuit was designed to gate out the signal within the period of the pulse and the response time of the capacitance meter. Therefore, a transient signal due to trap levels is retained, as in Fig. 8.5c. Using the DLTS rate window concept, a PAR HR-8 lock-in amplifier is used for the rate window (Fig. 8.5d), or a dual gated boxcar integrator can be applied as a rate window PAR 162 (Fig. 8.5e). The output of the lock-in amplifier or boxcar integrator is plotted against temperature on an X-Y recorder. A Sulfrian cryogenic dewar was modified for electrical measurements. An Artronix temperature controller was used for temperature selection and thermal scanning. Both a thermocouple and a calibrated

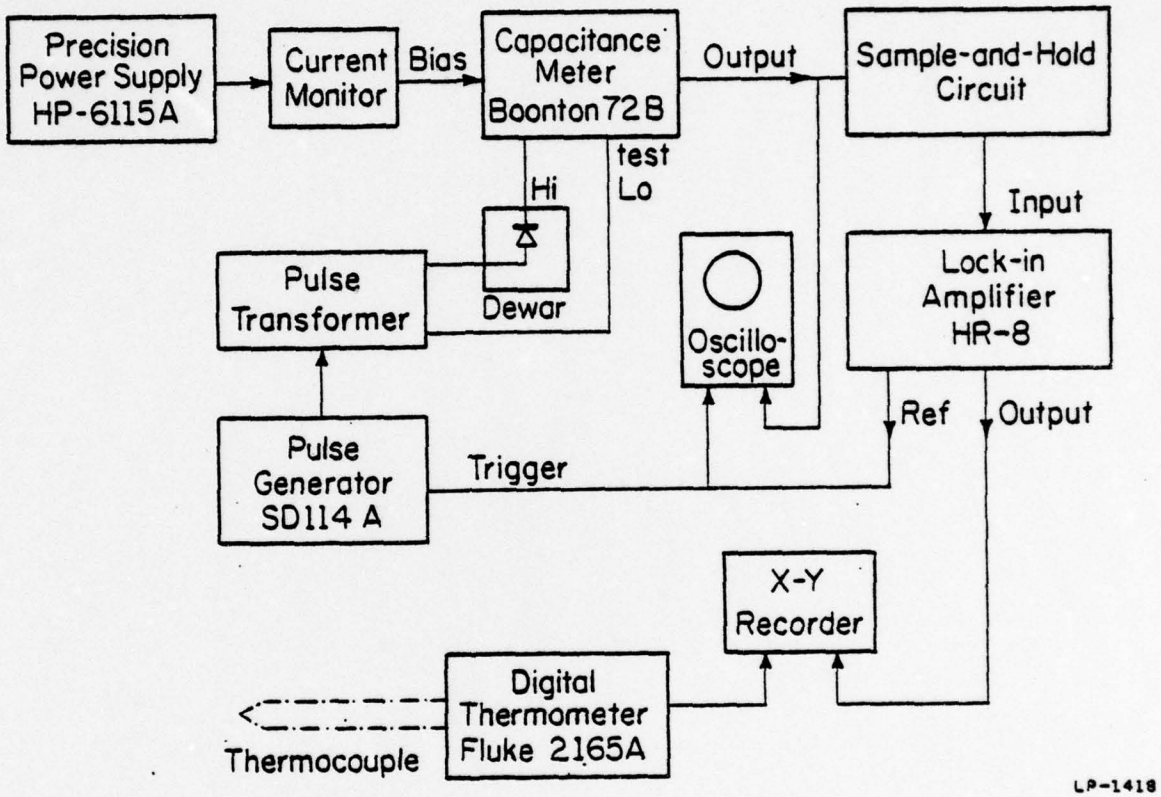

Fig. 8.4. Block diagram of DLTS system.

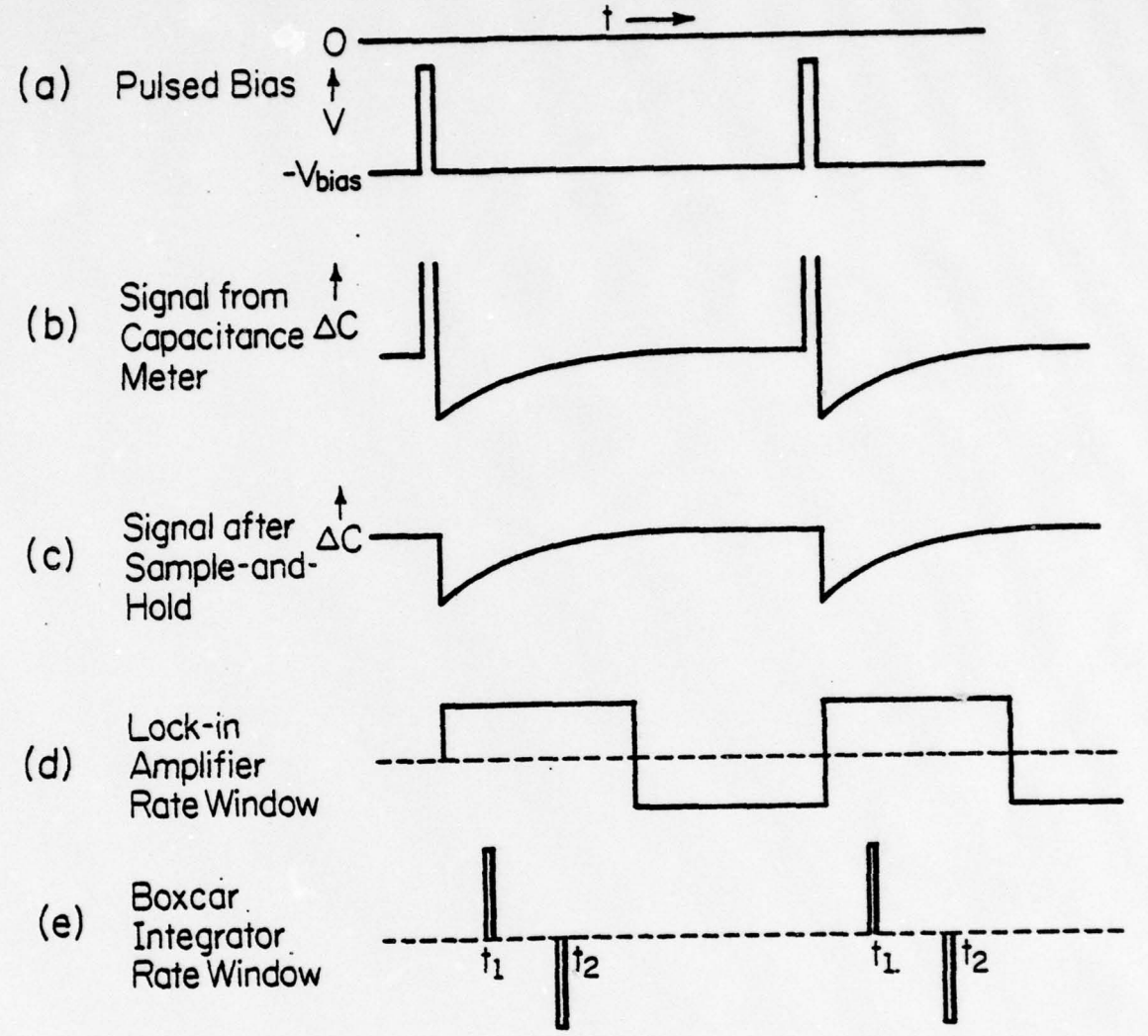

Fig. 8.5. Real signals processed in various points in the DLTS system.

Pt-thermometer were placed adjacent to the test diode for temperature measurements.

8.1.4. Data Analysis

Although the rate window concept is fairly simple, the data analysis involves rather complicated computation. Basically, the transient signal is characterized by a weighting function provided by a lock-in amplifier or boxcar integrator (Fig. 8.5d and e). The DLTS signal is the integration of the transient signal times the weighting functions [122]. For the boxcar integrator [119] with gates set at two instants (t_1 and t_2), the signal from the differential output is simply the capacitance at t_1 minus the capacitance at t_2, $C(t_1)- C(t_2)$. The value of decay time t at the maximum of $C(t_1)-C(t_2)$ vs. temperature T for a particular trap is called τ_{max}. It can be shown that

$$\tau_{max} = (t_2-t_1)/\ln(t_2/t_1) \qquad (8.2)$$

This result is based on the assumption that gate width of the boxcar in integrator is infinitesimal. It is known [119,122], however, that the signal to noise ratio increases with wider gate width (W). The detailed derivation of τ_{max} for a nonzero gate width W has been discussed elsewhere [123]. The resulting τ_{max}/t_1 vs. $p(= \frac{W}{t_2-t_1})$ for typical values of t_2/t_1 is shown in Fig. 8.6. If the midpoints of the gates $t_1 + \frac{W}{2}$ and $t_2 + \frac{W}{2}$ are used to substitute for t_1 and t_2 in equation 8.1, an approximation to τ_{max}/t_1 is obtained (shown dashed in Fig. 8.6). It is clear that the midpoint approximation introduces an error less than 10%.

Kimerling [124] has discussed the use of a lock-in amplifier for the DLTS rate window. The signal response, phase adjustment procedure,

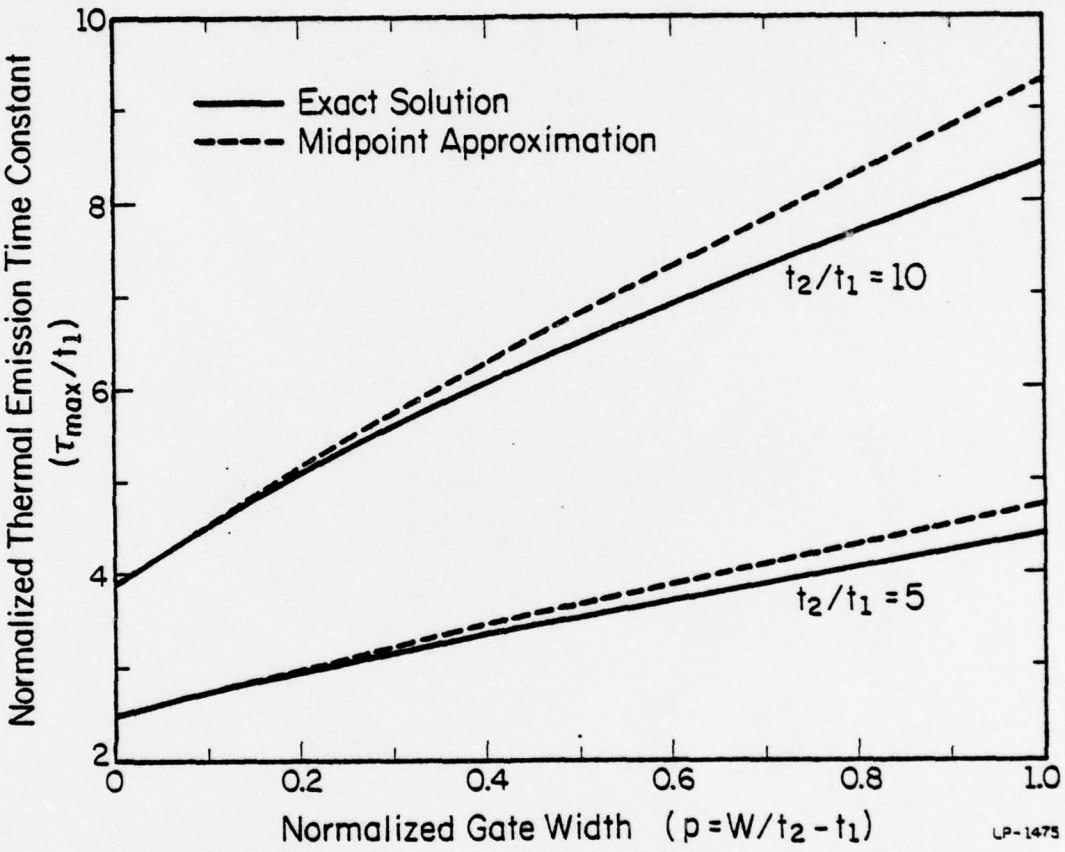

Fig. 8.6. Normalized emission time constant (τ_{max}/t_1) plotted vs. normalized gate width p for the boxcar integrator case. The solid lines are exact solutions and the dashed lines are the results from midpoint approximation.

and calculation of trap concentrations from the peak output of the lock-in amplifier have been discussed previously [125] for the ideal case, in which the system response time and overloading of the capacitance meter may be neglected. As discussed in Section 8.1.3, in fact a small portion (t_d) of the initial transient signal must be gated off by a sample-and-hold circuit. In this case, the ratio between transient peaks of the gated signal to the original signal is $e^{-t_d/\tau}$. Since τ is a function of temperature, the factor $e^{-t_d/\tau}$ complicates the data analysis. In the case of boxcar integrator, this complication can be avoided by setting $t_1 > t_d$. However, in the lock-in amplifier case, the analysis proposed by Schott et al. [125] is no longer valid. A detailed study of these effects and appropriate solutions has been discussed elsewhere [123]. The basic principle of the new analysis is to Fourier expand the transient signal, then calculate the τ_{max} as a function of lock-in amplifier frequency with correction for the gating-off period included.

The output of a lock-in amplifier depends on the phase tuning, We studied two methods [123], which we call the in-phase method and the maximum-output method. For the in-phase method one adjusts the internal reference signal of the lock-in amplifier in phase with the input signal. In the maximum-output method, one adjusts the phase angle to ϕ_{max}, giving maximum output for a certain transient signal input. Both methods yield the same information about a trap level, but use slightly different analysis. The normalized emission time constant τ_{max}/T_0 vs. f is plotted in Fig. 8.7, where $f(=\frac{1}{T_0})$ is the frequency of the lock-in amplifier. In the same figure, dashed lines show the results of neglecting the gating-off effect. The discrepancy is quite large; there, it is important to consider the gating-off effect in the lock-in amplifier DLTS system.

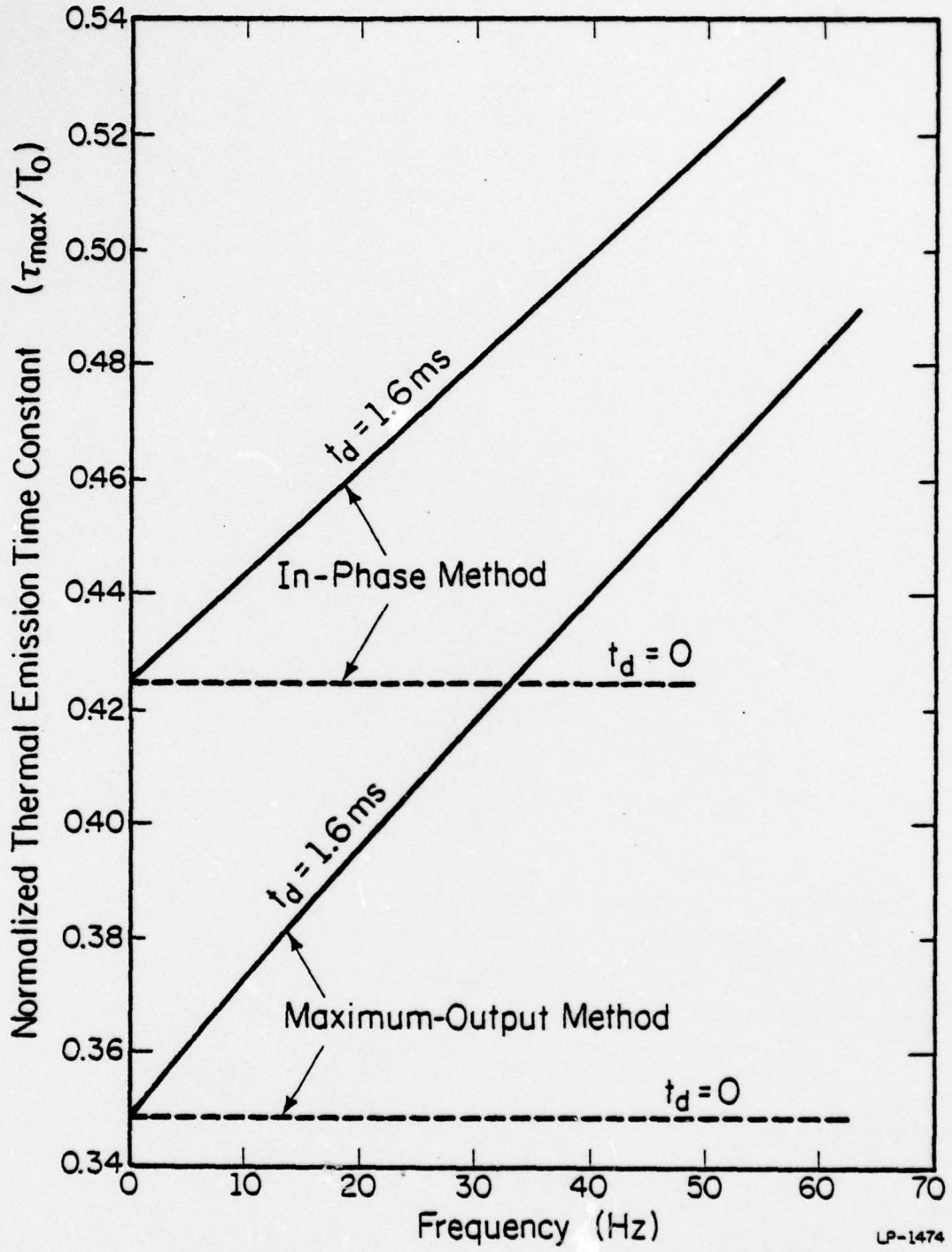

Fig. 8.7. Normalized emission time constant (τ_{max}/T_0) vs. pulse frequency f for the lock-in amplifier case. Results from both in-phase and maximum-output methods are shown. The dashed lines illustrate neglect of the gating-off effect.

8.1.5. System Calibration

Since Au-doped Si has been extensively studied before [126,127], characteristics of the Au levels are well known. To examine the various DLTS techniques discussed in the previous section, an n^+-p Au doped diode was measured. In order to simplify the results, only a Au-donor level was examined. The results are presented in Table 8.1. It is found that the midpoint approximation gives results almost identical to the exact solution for the boxcar integrator case. However, using the lock-in amplifier, neglect of the t_d effect introduces significant errors in τ_{max} and the energy level ΔE. The corrected in-phase method and maximum-input method yield the same results as obtained using the boxcar integrator. The corrected experimental value for the Au donor level ($\Delta E = .33 \pm .01$ eV) agrees well with Buehler's value [126]. This work on data analysis (Section 8.1.4) and system calibration (Section 8.1.5) of DLTS was done in collaboration with D.S. Day. The details are presented in Ref. 123.

8.2. Studies of Residual Damage in BF_2^+, Ga^+ Implanted Si

One of the useful applications of DLTS is the study of residual damage in ion-implanted semiconductors after annealing. Although the electrical activation of boron and gallium in Si has been studied thoroughly in Chapter 4 and 7 respectively, the residual damage is still not well understood. In this section, DLTS measurements on p^+-n diodes made from BF_2^+ or Ga^+ implanted Si are discussed. The results are compared with the current-voltage (I-V) characteristics.

8.2.1. Diode Fabrication

Either 150 keV BF_2^+ or 200 keV Ga^+ was implanted at room temperature into phosphorus-doped 4-6Ω-cm ⟨100⟩ Si to a fluence of 1×10^{15} cm^{-2}.

Table 8.1. Comparison of the thermal emission time constant and the energy level obtained from various methods.

CASE	METHOD	τ_{max} (msec)	ΔE (eV)
boxcar averager	exact solution	$2.73t_1$	0.33 ± 0.03
	midpoint approximation	$2.73t_1$	0.33 ± 0.03
lock-in amplifier	in-phase method:		
	with correction	$0.4282\ T_0 + 1.87$	0.33 ± 0.01
	without correction	$0.4282\ T_0$	0.36 ± 0.01
	maximum-output method:		
	with correction	$0.3485\ T_0 + 2.28$	0.33 ± 0.01
	without correction	$0.3485\ T_0$	0.38 ± 0.03

The energies chosen result in similar distributions of boron and gallium in silicon. After samples were annealed at 550°C for 2 hours, p^+-n diodes with 15 mil diameter were defined photolithographically and mesa etched. Al was used to form contacts to the p^+ region, and Au-Sb was alloyed to n region. After cleaving, diodes were mounted on TO-18 headers for measurement.

8.2.2. DLTS and I-V Measurements

The DLTS measurements for BF_2^+ and Ga^+-implanted mesa diodes are shown in Fig. 8.8 and 8.9 for two different majority carrier pulse heights, 10 and 8 volts. As illustrated in Fig. 8.5a, under the 10 V reverse bias, the 10 V pulse probes the area close to the junction region, whereas the 8 V pulse probes defects away from the junction. Since the output of the DLTS system is proportional to the concentration of defects [118,125], it is obvious the damage in the BF_2^+ diode is greater than that in the Ga^+ diode in the junction region (Fig. 8.8). Away from the junction (Fig. 8.9), however, the Ga^+ diode has more pronounced damage. These results are consistent with the electrical carrier profile measurements in Fig. 4.3 and Fig. 7.4, which indicate BF_2^+-implanted Si has a larger damaged region in the junction than does Ga^+-implanted Si after recrystallization at low temperature. It is not clear why the Ga^+-implanted diode exhibits greater damage away from the junction in DLTS, but it might be due to the propagation of defects from damaged region into n region in Ga^+-implanted Si during annealing.

The I-V characteristics of these diodes have been discussed elsewhere [128]. The data show BF_2^+ diodes have larger leakage current than Ga^+ diodes (at-70 V, leakage current is 5 na for Ga^+, 400 na for BF_2^+).

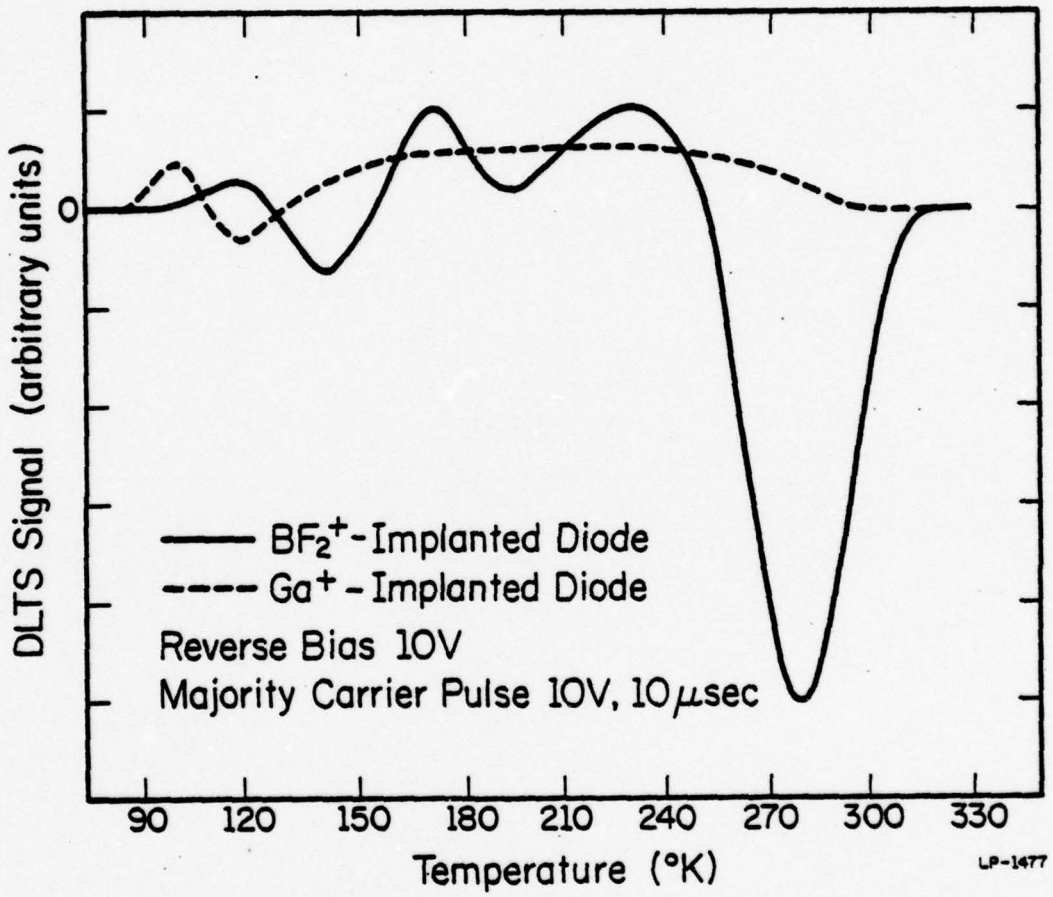

Fig. 8.8. DLTS data for BF_2^+ and Ga^+-implanted diodes. With 10V reverse bias, the 10V majority carrier pulse probes the damage close to the junction region.

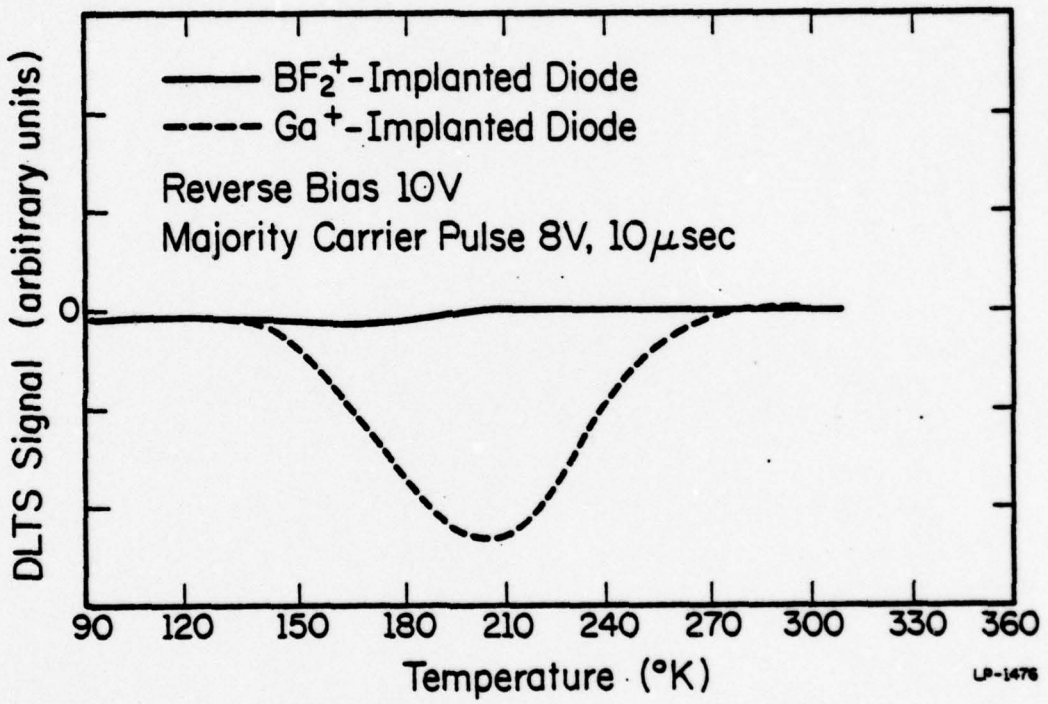

Fig. 8.9. DLTS data for BF_2^+ and Ga^+-implanted diodes. With 10V reverse bias, the 8V majority carrier pulse probes the damage away from the junction region.

This result agrees with our DLTS observation of more damage in the junction region of the BF_2^+ diode.

Both DLTS and I-V measurements were preliminary results and they were done on mesa etched diodes. Since the etched surface may have some effect on the results, measurements on planar diodes are needed to confirm these observations.

9. SUMMARY AND CONCLUSIONS

In this work, implanted amorphous Si formation through BF_2^+, $Si^+ + B^+$, or Ga^+ high-dose implantation has been studied by critical dose calculations and experimentally by amorphous Si etching. The electrical properties of recrystallized Si have been studied by differential resistivity and Hall effect measurements. The electrically active residual damage after annealing was examined by deep-level transient spectroscopy (DLTS). Anomalous redistribution of fluorine and gallium during annealing was investigated by secondary ion mass spectrometry (SIMS). Auger electron spectroscopy (AES) was used for studying the surface contamination produced by high-dose implantation. In this chapter, results and conclusions of this work are summarized.

I. Crystal Structure for High-Dose Implanted Si

After high-dose implantation, a continuous amorphous layer forms on the surface of the crystalline Si substrate, if the implanted ion dose is above the critical dose for amorphous state transformation at the implantation temperature. This amorphous Si transformation is illustrated by calculations using a critical-energy-density model or a damage-overlap model, and is detected by an experimental etching technique for the samples studied in this work. The theoretical calculations have some uncertainty, but the etching technique is verified to be a reliable method to detect amorphous Si and its thickness. Underneath this amorphous layer, a heavily damaged crystalline layer exists. As discussed below, this layer is responsible for electrical inactivation, gettering of impurities, and enhanced diffusion in Si.

The unique bilayer structure (amorphous and damaged crystalline layers) in high-dose implanted Si determines its annealing behavior. The

special electrical activation, impurity migration, and residual damage observed in high-dose BF_2^+, $Si^+ + B^+$, or Ga^+-implanted Si can be attributed to this bilayer structure.

II. Recrystallization of Implanted Amorphous Si

Although recrystallization of implanted amorphous Si has been studied by aligned backscattering methods [25,73], this work is the first to directly illustrate the recrystallization of amorphous layers from the underlying crystal toward the surface by the profiling of electrical carrier concentrations. We find that nearly 100% activation of implanted boron or gallium dopants can be achieved at 550-600°C annealing through recrystallization. In contrast, less than 85% activation can be obtained even after 900°C annealing for 30 min. Mobility is also recovered for boron in silicon through recrystallization at low temperature. However, the concentration of electrical carriers is found to be limited by the solid solubility ($1.2 \times 10^{20} cm^{-3}$) for boron in Si at 550°C (Chapter 4). In contrast, the activation of Ga by recrystallization in implanted amorphous layers can exceed the solid solubility. The advantage of high carrier concentration in Ga-implanted Si is compensated somewhat by lower mobility (Fig. 7.4). In addition, after annealing at 900°C, the activation of Ga is limited by solid solubility ($2 \times 10^{19} cm^{-3}$). The oversaturation of Ga activation at 550-600°C is the basic difference between boron and gallium in implanted amorphous Si.

Besides the good electrical activation of dopants in recrystallized amorphous Si, the impurity migration in this layer is also more predictable than in crystalline Si damaged by ion implantation. The normal migration of fluorine in Chapter 5 and normal diffusion of Ga in Chapter 7 are

confined to the recrystallized amorphous Si. This also indicates good crystal quality of the recrystallized amorphous Si.

A well-defined recrystallization rate, 80Å/min, has been found for implanted amorphous Si on ⟨100⟩ Si at 550°C [25], It has also been found that boron in amorphous Si will enhance the recrystallization rate [73]. In this work fluorine is found to have no electrical effect on the activation of boron in BF_2^+-implanted Si. Nevertheless, we find that fluorine slows down the recrystallization by comparing the recrystallization of amorphous Si containing BF_2 or B alone (Fig. 4.5 and 4.6). The estimated regrowth rate is 10-50Å/min at 550°C in BF_2^+-implanted Si.

III. Effects of Damaged Crystalline Si

Aligned backscattering methods have not been able to detect the damaged crystalline Si layer underneath the original amorphous Si layer after 550°C annealing [25,73]. This residual damage is apparently below the sensitivity limitation of backscattering methods. Transmission electron microscopy (TEM) has observed some defect clusters in the region under the recrystallized amorphous layer [28]. In this work, effects due to such damaged crystalline regions are reflected in electrical activation, impurity migration, and DLTS measurements. Whether the high-dose implants are performed at room temperature or near liquid nitrogen temperature, some residual damage is present after recrystallization.

The first effect is electrically inactive regions in BF_2^+, or Ga^+-implanted Si. An inactive tail is always observed below the original amorphous-crystalline interface after 550°C annealing (Figs. 4.3-4.5, 7.4). These cases of reduced activation are undoubtedly due to a combination of non-substitutional B or Ga (including Ga- or B-defect complexes) and

compensation of B or Ga acceptors by other defects. This inactive region is in sharp contrast to the ~100% activation in the recrystalled amorphous region itself.

The second effect observed is the gettering of fluorine by ion damage in BF_2^+-implanted Si. The pronounced fluorine peak found in the damaged crystalline region (Figs. 5.1, 5.3, 5.5) is a dramatic illustration of impurity-defect interaction. In samples implanted at room temperature, the gettering does not diminish until samples have been annealed at 1100^oC. It is interesting that this type of damage is much less severe in samples implanted at -110^oC, as indicated by the minor fluorine gettering observed in Fig. 5.5.

The damaged crystalline region in Ga^+-implanted Si is characterized by defect-enhanced diffusion. We find the diffusion coefficient for Ga in such damaged crystalline Si to be $\sim 4x10^{-14}$ cm^2sec^{-1} at 900^oC. This is a decade larger than the normal diffusivity of $4x10^{-15}$ cm^2sec^{-1} for Ga in Si, including recrystallized Si. The difference in diffusivity causes the anomalous redistribution observed in Ga^+-implanted Si (Fig. 4.1).

DLTS measurements also verify the existence of a damaged crystalline region near amorphous-crystalline interface. BF_2^+-implanted Si has more severe damage than Ga^+-implanted Si, since the damaged crystalline region in BF_2^+-implanted Si is larger. This reflects in the DLTS measurements and the diode characteristics reported here (Fig. 8.8, and Section 8.2).

IV. Low Temperature Annealing

As discussed above, the damaged crystalline Si layer in high-dose implanted Si is the cause of many problems. High activation can be achieved by recrystallization at low temperature ($\sim 550^{\circ}C$), but this underlying damaged crystalline Si region is still unannealed at this temperature. Therefore, Si^+ multiple implants are used to purposely create a continuous amorphous layer, then the desired dopant (e.g., B^+) is implanted into this pre-amorphized layer. This successfully removes the inactive tail (Fig. 4.6) which is always observed in BF_2^+-implanted Si. In these Si^+-preamorphized samples, the damaged crystalline layer still exists, but it is now located under the thicker amorphous layer, away from the junction. The effect of removing the damaged crystalline layer from the junction region has important implications, and deserves further study. This result allows the fabrication of high-quality junctions using low temperature processing, which is compatible with Al metallization and provides excellent profile control with negligible diffusion.

V. Surface Contamination

Another problem associated with high-dose implantation is the carbonaceous surface contamination produced by typical ion-implantation procedures. These contamination layers (up to $\sim 100\text{Å}$ thick) have been examined here by Auger electron spectroscopy. Such layers inhibit etching and interfere with ohmic contact formation. No simple methods apart from anodization and stripping have been found to remove these layers. However, by using perfluorinated polyether diffusion pump oil in the implanter target chamber vacuum system, the contamination layer can be effectively eliminated.

VI. Further Studies

The detailed nature of residual ion damage in high-dose implanted silicon is still unknown. In view of the importance of this problem, further studies should be performed to obtain a better understanding of the character of this damage.

(1) More detailed DLTS studies should be performed on recrystallized amorphous Si. The electrical activation and mobility in recrystallized amorphous layers formed by BF_2^+ or $Si^+ + B^+$ are extremely good. However, information on carrier lifetime and trapping inside the recrystallized layer is still lacking. A detailed DLTS study on recrystallized amorphous Si layer formed by Si^+ implants will provide the necessary information about the quality of the recrystallized layers.

(2) DLTS studies of the annealing behavior of the damaged crystalline layer should be performed. The damaged crystalline Si underneath the amorphized layer has been found in this work to be quite important. In typical high-dose implanted Si junctions, this layer is located at the p-n junction region. Isochronal annealing studies on diodes fabricated from BF_2^+-implanted Si may reveal the nature of this residual damage and the optimum annealing procedure.

(3) TEM Studies on high-dose implanted Si would be useful, particularly if it is correlated with electrical measurements. TEM is a powerful technique for revealing dislocations and clusters of defects. Although DLTS can measure the electrical properties of the residual damage, the microstructure inside the sample should be examined by TEM.

It would be particularly interesting to examine Ga^+-implanted Si by TEM. Changes in the crystalline microstructure might provide some basic understanding of the oversaturation effect in 600°C recrystallized Ga^+-implanted material (Fig. 7.4) and its loss of activity after annealing above 900°C (Fig. 7.5).

In conclusion, this work has identified the characteristics of electrical activation, impurity migration, and residual damage of high-dose BF_2^+, $Si^+ + B^+$, or Ga^+ implanted Si, and correlated these characteristics with the effects of recrystallization in amorphous Si and damage in crystalline Si. It also resolves the surface contamination problem introduced by high-dose implantation.

REFERENCES

1. J. W. Mayer, L. Eriksson, and J. A. Davies, Ion Implantation in Semiconductors, Academic Press, New York, 1970.

2. G. Dearnaley, J. H. Freeman, R. S. Nelson, and J. Stephen, Ion Implantation, North-Holland Publishing Co., Amsterdam, 1973.

3. I. Ruge and J. Graul, Ion Implantation in Semiconductors, Springer-Verlag, Berlin, 1971.

4. F. H. Eisen and L. T. Chadderton, Ion Implantation, Gordon and Breach, London, 1971.

5. B. L. Crowder, Ion Implantation in Semiconductor and Other Materials, Plenum Press, New York, 1973.

6. S. Namba, Ion Implantation in Semiconductors, Plenum Press, New York, 1975.

7. F. Chernow, J. A. Borders, and D. K. Brice, Ion Implantation in Semiconductors, Plenum Press, New York, 1977.

8. D. H. Lee and J. W. Mayer, "Ion implanted semiconductor devices," Proc. IEEE, Vol. 62, pp. 1241-1255, 1974.

9. J. Sansbury, "Applications of ion-implantation to semiconductor processing," Solid State Technology, pp. 31-43, November 1976.

10. T. H. P. Chang, "The potential of electron beam technology for microfabrication," Japan. J. Appl. Phys., Vol. 16, Supplement 16-1, pp. 9-16, 1976.

11. E. I. Gordan and D. R. Herriot, "Pathways in device lithography," IEEE Trans. Electron Devices, Vol. ED-22, pp. 371-375, 1975.

12. H. I. Smith and D. C. Flanders, "X-ray lithography," Japan. J. Appl. Phys., Vol. 16, Supplement 16-1, pp. 61-65, 1976.

13. J. S. Greeneich, "X-ray lithography," IEEE Trans. Electron Devices, Vol. ED-22, pp. 434-439, 1975.

14. R. L. Bersin, "A survey of plasma-etching process," Solid State Technology, pp. 31-36, May 1976.

15. A. Jacob, "The versatile technique of RF plasma etching," Solid State Technology, pp. 95-98, April 1978.

16. L. M. Ephrath, "Selective etching of silicon dioxide using reactive ion etching with CF_4-H_2," IBM Research Report, RC 6931, 1978.

17. L. Altman and C. L. Cohen, "The gathering wave of Japanese technology," Electrons, Vol. 50, No. 12, pp. 110-122, June 1977.

18. M. R. MacPherson, "Threshold shift calculations for ion-implanted MOS devices," Solid State Electron., Vol. 15, pp. 1319-1326, 1972.

19. T. W. Sigman and R. Swanson, "MOS threshold shifting by ion implantation," Solid State Electron., Vol. 11, pp. 1217-1232, 1973.

20. A. F. Tasch, Jr., P. K. Chatterjee, H-S. Fu, T. C. Holloway, "The Hi-C RAM cell concept," IEEE Trans. Electron. Devices, Vol. ED-23, pp. 31-41, 1978.

21. R. A. Moline and G. W. Reutlinger, "Self-aligned maskless chan stops for IGFET integrated circuits," IEEE Trans. Electron Devices, vol. ED-201 pp. 1129-1132, 1973.

22. F. F. Fang and H. S. Rupprecht, "High performance MOS integrated circuit using the ion implantation technique," IEEE J. Solid-State Circuits, Vol. SC-10, pp. 205-211, 1975.

23. S. Wagner, "Diffusion of boron from shallow ion implants in silicon," J. Electrochem. Soc., Vol. 119, pp. 1570-1576, 1972.

24. T. Tokuyama, "Use of ion implantation in device fabrication at Hitachi CRL," in Ref. 7, pp. 519-533.

25. L. Csepregi, J. W. Mayer, and T. W. Sigmon, "Channeling effect measurements of the recrystallization of amorphous Si layers on crystal Si," Phys. Lett., Vol. 54A, pp. 157-158, 1975.

26. L. Csepregi, E. F. Kennedy, S. S. Lau, and J. W. Mayer, "Disorder produced by high-dose implantation in Si," Appl. Phys. Lett., Vol. 29, pp. 645-648, 1976.

27. L. D. Glowinski, K. N. Tu, and P. S. Ho, "Direct observations of defects in implanted and postannealed silicon wafers," Appl. Phys. Lett., Vol. 28, pp. 312-313, 1976.

28. L. D. Glowinski, P. S. Ho, and K. N. Tu, "Residual damage in silicon implanted and post-annealed silicon," in Ref. 7, pp. 461-469.

29. H. J. Stein, F. L. Vook, D. K. Brice, J. A. Borders, and S. T. Picraux, "Infrared studies of the crystallinity of ion-implanted Si," in Ref. 4, pp. 17-24.

30. F. F. Morehead, Jr. and B. L. Crowder, "A model for the formation of amorphous Si by ion bombardment," Rad. Effects, Vol. 6, pp. 27-32, 1970.

31. R. G. Wilson and G. R. Brewer, Ion Beams with Application to Ion Implantation, John Wiley and Sons, New York, 1973, pp. 49-61.

32. P. Williams (Private communication).

33. J. Lindhard, M. Scharff, and H. Schiott, "Range concepts and heavy ion ranges (Notes on atomic collision II)," K. Dan. Vidensk. Selsk. Mat. Fys. Medd., Vol. 33, pp. 1-39, 1963.

34. This program was adapted from the formulation of Johnson, Gibbons, and Mylorie (Ref. 35) by W. E. Miller of NASA Langley.

35. J. F. Gobbons, W. S. Johnson, and S. V. Mylroie, Projected Range Statistics, Semiconductor and Related Materials, 2nd edition, Dowden, Hutchinson, and Ross, Stroudsburg, 1975.

36. F. H. Eisen, "Channeling of medium-mass ion through Si," Can. J. Phys., Vol. 46, pp. 561572, 1968.

37. L. Northcliffe and Schilling, Nuclear Data Tables A, 1968.

38. H. B. Dietrich and L. E. Plew, "^{19}F range-energy curve in Si from 100 to 500 keV," Appl. Phys. Lett., Vol. 29, pp. 406-408, 1976.

39. H. Muller, H. Ryssel, and I. Ruge, "A new method for boron doping of silicon by implantation of BF_2-molecules," in Ref. 3, pp. 85-95.

40. J. W. Mayer, O. J. Marsh, G. A. Shifrin, and R. Baron, "Ion implantation of silicon: II Electrical evaluation using Hall-effect measurements," Can. J. Phys., Vol. 45, pp. 4073-4089, 1967.

41. N. G. E. Johansson, J. W. Mayer, and O. J. Marsh, "Technique used in Hall-effect analysis of ion implanted Si and Ge," Solid State Electron., Vol. 13, pp. 317-335, 1970.

42. W. V. McLevige, P. K. Chatterjee, and B. G. Streetman, "Versatile double AC Hall-effect system for profiling impurities in semiconductors," J. Phys. E: Sci. Instrum., Vol. 10, pp. 335-337, 1977.

43. W. V. McLevige, "Annealing studies of beryllium in gallium arsenide and gallium arsenide phosphide," Ph.D. thesis, University of Illinois, 1977. Also Coordinated Science Laboratory Report R-802, UILU-ENG 77-2249.

44. L. J. van der Pauw, "A method of measuring specific resistivity and Hall-effect of discs of arbitrary shape," Philips Res. Rept., Vol. 13, pp. 1-9, 1958.

45. R. L. Petritz, "Theory of an experiment for measuring the mobility and density of carriers in the space-charge region of a semiconductor surface," Phys. Rev., Vol. 110, pp. 1254-1262, 1958.

46. K. B. Wolfstirn, "Hole and electron mobilities in doped silicon from radiochemical and conductivity measurements," Phys. Chem. Solids, Vol. 16, pp. 279-284, 1960.

47. J. Hilibrand and R. D. Gold, "Determination of the impurity distribution in junction diodes from capacitance-voltage measurements," RCA Rev., Vol. 21 , pp. 245-252, 1960.

48. D. P. Kennedy, P. C. Murley, and W. Kleinfelder, "On the measurement of impurity atom distributions in silicon by the differential capacitance technique," IBM J. Res. Develop., Vol. 12, pp. 399-409, 1968.

49. W. C. Johnson and P. T. Panousis, "The influence of Debye length on the C-V measurement of doping profiles," IEEE Trans. Electron Devices, Vol. ED-18, pp. 965-973, 1971.

50. W. E. Carter, H. K. Gummel, and B. R. Chawla, "Interpretation of capacitance vs. voltage measurements of p-n junctions," Solid-State Electron., Vol. 15, pp. 195-201, 1972.

51. C. P. Wu, E. C Douglas, and C. W. Mueller, "Limitation of the C-V technique for ion-implanted profiles," IEEE Trans. Electron Devices, Vol. ED-22, pp. 319-329, 1975.

52. C. A. Evans, Jr., "Ion probe mass spectrometry: overview," Thin Solid Films, Vol. 19, pp. 11-19, 1973.

53. C. A. Evans, Jr., "Surface and thin film analysis," Anal. Chem., Vol. 47, pp. 855-866, 1975.

54. P. Williams, R. K. Lewis, and C. A. Evans, Jr., "Evaluation of a cesium primary ion source on an ion microprobe mass spectrometer," Anal. Chem., Vol. 49, pp. 1399-1402, 1977.

55. T. A. Carlson, Photoelectron and Auger Spectroscopy, Plenum Press, New York, 1975, pp. 279-325.

56. R. J. Blattner, C. A. Evans, Jr., and A. J. Braundmeier, Jr., "Mechanism of high-temperature instability of CuO-Ag thin-film solar absorbers," J. Vac. Sci. Technol., Vol. 14, pp. 1132-1138, 1977.

57. B. L. Crowder, R. S. Title, M. H. Brodsky, and G. D. Pettit, "ESR and optical absorption studies of ion-implanted silicon," Appl. Phys. Lett., Vol. 16, pp. 205-308, 1970.

58. F. L. Vook, "Radiation damage during ion implantation," Radiation Damage and Defects in Semiconductors, edited by J. E. Whitehouse, Institute of Physis, London, 1972, pp. 60-71.

59. J. F. Gibbons, "Ion implantation in semiconductors: II Damage production and annealing," Proc. IEEE, Vol. 60, pp. 1062-1096, 1972.

60. J. R. Dennis and E. B. Hale, "Crystalline to amorphous transformation in ion-implanted silicon: a composite model," J. Appl. Phys., Vol. 49, pp. 1119-1127, 1978.

61. T. W. Sigman (private communication).

62. D. K. Brice, Ion Implantation Range and Energy Deposition Distributions, Vol. 1, IFI/Plenum Data Co., New York, 1975.

63. J. B. Mitchell, J. A Davies, L. M. Howe, R. S. Walker, K. B. Winterbon, G. Foti, and J. A. Moore, "The use of molecular ions for implantation studies in Si and Ge," in Ref. 6, pp. 493-500.

64. J. A. Davies, G. Foti, L. M. Howe, J. B. Mitchell, and K. B. Winterbon, "Polyatomic-ion implantation damage in silicon," Phys. Rev. Lett., Vol. 34, pp. 1441-1444, 1975.

65. H. J. Stein, "Divacancy formation by polyatomic ion implantation," in Ref. 7, pp. 401-407.

66. R. S. Nelson and D. J. Mazey, "The influence of temperature and channeling on ion-bombardment damage in Si," Can. J. Phys., Vol. 46, pp. 689-694, 1968.

67. F. F. Morehead, B. L. Crowder, and R. S. Title, "Formation of amorphous Si by ion bombardment as a function of ion, temperature, and dose," J. Appl. Phys., Vol. 43, pp. 1112-1118, 1972.

68. D. J. Mazey, R. S. Nelson, and R. S. Barnes, "Observation of bombardment damage in silicon," Phil. Mag., Vol. 17, pp. 1145, 1968.

69. M. H. Brodsky and R. S. Title, "Electron spin resonance in amorphous silicon, germanium, and silicon carbide," Phys. Rev. Lett., Vol. 23, pp. 581-585, 1969.

70. N. N. Gerasimenko, A. V. Dvurechenskii, S. I. Romanov, and L. S. Smirnov, "Effects of large doses of implanted ions on a semiconductor," Sov. Phys. Semicond., Vol. 7, pp. 1461-1464, 1974.

71. K. Shimizu, H. Kawakatsu, and K. Kanaya, "Contamination layers formed by argon ion bombardment," J. Phys. D: Appl. Phys., Vol. 8, pp. 1453-1459, 1975.

72. M. Yamaguchi and T. Hirayama, "Surface contamination of silicon produced by ion implantation," Japan. J. Appl. Phys., Vol. 15, pp. 365-372, 1976.

73. L Csepregi, E. F. Kennedy, T. J. Gallagher, J. W. Mayer, and T. W. Sigmon," Reordering of amorphous layers of Si implanted with ^{31}P, ^{75}As and ^{11}B ions," J. Appl. Phys., Vol. 48, pp. 4234-4240, 1977.

74. B. L. Crowder, "The role of damage in the annealing characteristics of ion implanted Si," J. Electrochem. Soc., Vol. 117, pp. 671-674, 1970.

75. B. L. Crowder, "The influence of the amorphous phase on ion distributions and annealing behavior of group III and group V ions implanted into Si," J. Electrochem. Soc., Vol. 118, pp. 943-952, 1971.

76. S. Prussin, "Ternary defects resulting from the implantation of B, F, BF, and BF_2 ions into silicon, their formation and effect upon device properties," in Ref. 6, pp. 449-456.

77. B. A. MacIver and E. Greenstein, "Damage effects in boron and BF_2 ion implanted p^+-n junctions in silicon," J. Electrochem. Soc., Vol. 124, pp. 273-275, 1977.

78. M. Y. Tsai, B. G. Streetman, P. Williams, and C. A. Evans, Jr., Anamalous migration of fluorine and electrical activation of boron in BF_2^+-implanted silicon," Appl. Phys. Lett., Vol. 32, pp. 144-147, 1978.

79. D. G. Beanland, "The behavior of boron molecular ion implants into silicon," Solid State Electronics, Vol. 21, pp. 537-547, 1978.

80. T. E. Seidel and A. U. MacRae, "The isothermal annealing of boron implanted silicon," in Ref. 4, pp. 149-154.

81. J. C. Irvin, "Resistivity of bulk silicon and of diffused layers in silicon," Bell Syst. Tech. J., Vol. 41, pp. 387-410, 1962.

82. F. A. Trumbore, "Solid solubilities of impurity elements in germanium and silicon," Bell Syst. Tech. J., Vol. 39, pp. 205-233, 1960.

83. H. B. Dietrich, W. H. Weisenberger, and J. Comas, "Anomalous migration of ion-implanted Al in Si," Appl. Phys. Lett. Vol. 28, pp. 182-184, 1976.

84. H. B. Dietrich and J. Comas, "Anomalous redistribution of ion-implanted dopants," in Ref. 7, pp. 735-742.

85. T. E. Seidel, R. L. Meek, and A. G. Cullis, "Direct comparison of ion-damage gettering and phosphorus-diffusion gettering of Au in Si," J. Appl. Phys., Vol. 46, pp. 600-609, 1975.

86. P. Ashburn and D. V. Morgan, "The role of radiation damage on the current-voltage characteristics of p-n junctions," Solid State Electronics, Vol. 17, pp. 689-698, 1974.

87. R. C. Henderson, R. B. Marcus, and W. J. Polito, " Carbide contamination of silicon surfaces," J. Appl. Phys., Vol. 42, pp. 1208-1215, 1971.

88. R. W. Christy, "Formation of thin polymer films by electron bombardment," J. Appl. Phys., Vol. 31, pp. 1680-1683, 1960.

89. Fomblin is a trademark of Montedison S. P. A.

90. R. W. Berry, P. M. Hall, and M. T. Harris, Thin Film Technology, Van Nostrand Reinhold Co., N. Y., 1978, pp. 22-24.

91. W. Kern and D. A. Puotiner, "Cleaning solutions based on hydrogen peroxide for use in silicon semiconductor technology," RCA Review, Vol. 31, pp. 187-206, 1970.

92. H. Jaskolska, L. Walis, and H. Golkowska, "The need to use appropriate calibration curves for the anodic oxidation of ion-implanted silicon," Thin Solid Films, Vol. 33, pp. 281-286, 1976.

93. G. Carter and J. S. Colligon, Ion Bombardment of Solids, American Elsevier, New York, 1968, pp. 313.

94. F. K. Naehring, A. Schmidt, and J. Schoneich, "Ion induced carbon contamination and recoil implantation," Phys. Stat. Sol., Vol. 44a, pp. K141-145, 1977.

95. D. E. Davies, "Post annealing conductance behavior of implanted layers in silicon," Appl. Phys. Lett., Vol. 14, pp. 227-229, 1969.

96. M. Y. Tsai, D. S. Day, B. G. Streetman, P. Williams, and C. A. Evans, Jr., "Recrystallization of implanted amorphous silicon layers: II. Migration of fluorine in BF_2^+-implanted silicon," J. Appl. Phys. (to be published Oct. 1978).

97. D. Kunze, O. Peters, and G. Sauerbrey, Z. Agnew. Phys., Vol. 22, pp. 69, 1967.

98. H. W. Conru and P. L. Laberge, "Oil contamination with the SEM operated in the spot scanning mode," J. Phys. E: Sci. Inst., Vol. 8, pp. 136-138, 1975.

99. M. A. Baker, L. Holland, and L. Laurenson, "The use of perfluoroalkyl polyether fluids in vacuum pumps," Vacuum, Vol. 21, pp. 479-481, 1971.

100. K. N. Tu, S. I. Tan, and B. L. Crowder, "Circular etch pits in ion-implanted amorphous silicon films," Appl. Phys. Lett., Vol. 22, pp. 274-275, 1973.

101. See for example, R. W. Aldrich and N. Holonyak, "Two-terminal asymetrical and symetrical silicon negatives resistance switches," J. Appl. Phys., Vol. 30, pp. 1819-1824, 1959.

102. D. P. Oosthoek, J. A. den Boer, and W. K. Hofker, Proc. European Conf. Ion Implantation, Reading, Peter Peregrinus Ltd., pp. 88, 1970.

103. J. Stephen and J. A. Grimshaw, "The electrical behavior of abrupt ion implanted and diffused p^+n junctions," Rad. Effects., Vol. 7, pp. 73-85, 1971.

104. J. H. Howes and G. Knill, Proc. European Conf. Ion Implantation, Reading, Peter Peregrinus Ltd., pp. 97, 1970.

105. K. Gamo, M. Iwaki, K. Masuda, S. Namba, S. Ishihara, I. Kimura, I. V. Mitchell, G. Ilic, J. L. Whitton, and J. A. Davies, "Enhanced diffusion and lattice location of indium and gallium implanted in silicon," Japan. J. Appl. Phys., Vol. 12, pp. 735-741, 1973.

106. G. Dearnaley, G. A. Gard, W. Temple, and M. A. Wilkins, "Depth distribution of gallium ions implanted into silicon crystals," Appl. Phys. Lett., Vol. 27, pp. 17-18, 1975.

107. N. G. E. Johansson and J. W. Mayer, "Hall effect measurements on Sb and Ga implanted silicon; anneal behavior and comparison with other species," Solid-State Electron., Vol. 13, pp. 123-130, 1970.

108. B. I. Boltaks, Diffusion in Semiconductors, Academic Press, New York, 1963, pp. 209-211.

109. B. L. Crowder and F. F. Morehead, Jr., "Annealing characteristics of n-type dopants in ion-implanted silicon," Appl. Phys. Lett., Vol. 14, pp. 313-315, 1969.

110. R. Baron, G. A. Shifrin, O. J. Marsh, and J. W. Mayer, "Electrical behavior of group III and V implanted dopants in silicon," J. Appl. Phys., Vol. 40, pp. 3702-3719, 1969.

111. J. F. Gibbons, "Ion implantation in semiconductors- Part II: damage production and annealing," Proc. IEEE, Vol. 60, pp. 1062-1096, 1972.

112. L. C. Kimerling and J. M. Poate, "Lattice defects in ion-implanted semiconductors," Inst. Phys. Conf. Ser. No. 23, Chapter 1, pp. 126-148, 1975.

113. D. S. Billington and J. H. Crawford, Jr., Radiation Damage in Solids, Princeton University Press, Princeton, N. J., 1961, pp. 312-368.

114. R. J. Spry and W. D. Compton, "Recombination luminescence in irradiated Si," Phys. Rev., Vol. 175, pp. 1010-1020, 1968.

115. C. G. Kirkpatrick, J. R. Noonan, and B. G. Streetman, "Recombination luminescence from ion implanted silicon," Rad. Eff., Vol. 30, pp. 97-106, 1976.

116. C. T. Sah, "Bulk and interface imperfections in semiconductors," Solid-State Electronics, Vol. 19, pp. 975-990, 1976.

117. H. Kukimoto, C. H. Henry, and F. R. Merritt, "Photocapacitance studies of the oxygen donor in GaP. I. optical cross sections, energy levels and concentration," Phys. Rev. B7, pp. 2486-2499, 1973.

118. D. V. Lang, "Deep-level transient specrroscopy: a new method to characterize traps in semiconductors," J. Appl. Phys., Vol. 45, pp. 3023-3032, 1974.

119. G. L. Miller, D. V. Lang, and L. C. Kimerling, "Capacitance transient spectroscopy," Ann. Rev. Mater. Sci., pp. 377-448, 1977.

120. R. Williams, "Determination of deep centers in conducting gallium arsenide," J. Appl. Phys., Vol. 37, pp. 3411-3416, 1966.

121. C. H. Henry, H. Kukimoto, G. L. Miller, and F. R. Merritt, "Photocapacitance studies of the oxygen donor in GaP. II. Capture cross sections," Phys. Rev. B, Vol. 7, pp. 2499-2507, 1973.

122. G. L. Miller, J. V. Ramirez, and D. A. H. Robinson, "A correlation method for semiconductor transient signal measurements," J. Appl. Phys., Vol. 48, pp. 2638-2644, 1975.

123. D. S. Day, M. Y. Tsai, B. G. Streetman, and D. V. Lang, "Deep-level transcient spectroscopy: system effects and data analysis," (unpublished).

124. L. C. Kimerling, "New developments in defect studies in semiconductors," IEEE Trans. Nucl. Sci., Vol. NS-23, pp. 1497-1505, 1976.

125. J. T. Schott, H. M. DeAngelis, W. R. White, "Transient capacitance measurement of deep defect levels in GaAs and Si," Report of Air Force Cambridge Research Laboratories, Hanscon, Mass., PSRP No. 655, 1976.

126. M. G. Buehler, "Impurity centers in p n junctions determined from shifts in the thermally stimulated current and capactiance response with heating rate," Solid-State Electron., Vol. 15, pp. 69-79, 1972.

127. C. T. Sah, L. Forbes, L. L. Rosier, A. F. Tasch, Jr., and A. B. Tole, "Thermal emission rates of carriers at Au centers in Si," Appl. Phys. Lett., Vol. 15, pp. 145-148, 1969.

128. K. J. Soda, M. Y. Tsai, and B. G. Streetman, "Properties of p^+-n implanted Si junctions fabricated with low temperature annealing, (unpublished).

APPENDIX 1

Projected Range Statistics of Implanted F in Si, obtained from LSS Theory

LSS RANGE STATISTICS FOR F IN SI

SUBSTRATE PARAMETERS-

SI

Z	14
M	28.086
N	.4995E+23
RHO/R	.3271E+02
EPS/E	.4838E-01
CNSE	.2474E+02
MU	1.478
GAMMA	.9628
SNO	.2207E+03

ION- F

Z	9
M	19.000

ELECTRONIC CROSS SECTIONS OF LINDHARD,SCHARFF,SCHIOTT

ENERGY (KEV)	PROJECTED RANGE (MICRONS)	PROJECTED STANDARD DEVIATION (MICRONS)	RANGE (MICRONS)	STANDARD DEVIATION (MICRONS)	NUCLEAR ENERGY LOSS (KEV/MICRON)	ELECTRONIC ENERGY LOSS (KEV/MICRON)
10	0.0217	0.0098	0.0339	0.0112	0.2726E+03	0.7825E+02
20	0.0415	0.0168	0.0619	0.0195	0.2439E+03	0.1107E+03
30	0.0626	0.0237	0.0902	0.0272	0.2191E+03	0.1355E+03
40	0.0841	0.0300	0.1183	0.0341	0.1992E+03	0.1565E+03
50	0.1060	0.0359	0.1464	0.0404	0.1819E+03	0.1750E+03
60	0.1282	0.0415	0.1744	0.0463	0.1673E+03	0.1917E+03
70	0.1506	0.0468	0.2021	0.0516	0.1556E+03	0.2070E+03
80	0.1729	0.0517	0.2295	0.0564	0.1466E+03	0.2213E+03
90	0.1951	0.0561	0.2565	0.0607	0.1372E+03	0.2347E+03
100	0.2174	0.0605	0.2832	0.0648	0.1277E+03	0.2474E+03
110	0.2398	0.0647	0.3098	0.0686	0.1193E+03	0.2595E+03
120	0.2623	0.0688	0.3360	0.0723	0.1117E+03	0.2711E+03
130	0.2847	0.0727	0.3620	0.0757	0.1052E+03	0.2821E+03
140	0.3070	0.0765	0.3877	0.0789	0.9954E+02	0.2928E+03
150	0.3292	0.0800	0.4130	0.0819	0.9488E+02	0.3031E+03
160	0.3512	0.0834	0.4379	0.0847	0.9118E+02	0.3130E+03
170	0.3729	0.0866	0.4625	0.0874	0.8844E+02	0.3226E+03
180	0.3942	0.0896	0.4866	0.0898	0.8665E+02	0.3320E+03
190	0.4152	0.0923	0.5102	0.0920	0.8581E+02	0.3411E+03
200	0.4357	0.0949	0.5334	0.0941	0.8593E+02	0.3499E+03
220	0.4757	0.0997	0.5785	0.0978	0.8206E+02	0.3670E+03
240	0.5150	0.1042	0.6226	0.1011	0.7594E+02	0.3833E+03
260	0.5539	0.1084	0.6656	0.1042	0.7059E+02	0.3990E+03
280	0.5922	0.1123	0.7077	0.1071	0.6600E+02	0.4140E+03
300	0.6300	0.1160	0.7490	0.1097	0.6218E+02	0.4286E+03
320	0.6671	0.1195	0.7893	0.1121	0.5912E+02	0.4426E+03
340	0.7035	0.1228	0.8287	0.1144	0.5683E+02	0.4563E+03
360	0.7393	0.1258	0.8672	0.1164	0.5531E+02	0.4695E+03
380	0.7743	0.1286	0.9049	0.1183	0.5454E+02	0.4824E+03
400	0.8085	0.1313	0.9417	0.1200	0.5454E+02	0.4949E+03
420	0.8419	0.1337	0.9777	0.1216	0.5419E+02	0.5071E+03
440	0.8748	0.1361	1.0130	0.1231	0.5191E+02	0.5190E+03
460	0.9073	0.1383	1.0478	0.1245	0.4976E+02	0.5307E+03
480	0.9393	0.1404	1.0820	0.1259	0.4774E+02	0.5421E+03
500	0.9710	0.1424	1.1156	0.1271	0.4585E+02	0.5533E+03
550	1.0484	0.1471	1.1975	0.1300	0.4170E+02	0.5803E+03
600	1.1234	0.1513	1.2765	0.1325	0.3835E+02	0.6061E+03
650	1.1963	0.1551	1.3527	0.1348	0.3581E+02	0.6309E+03
700	1.2670	0.1585	1.4265	0.1368	0.3409E+02	0.6547E+03
750	1.3356	0.1616	1.4980	0.1386	0.3317E+02	0.6776E+03
800	1.4022	0.1644	1.5673	0.1402	0.3306E+02	0.6999E+03
850	1.4668	0.1670	1.6345	0.1416	0.3267E+02	0.7214E+03
900	1.5298	0.1694	1.6999	0.1430	0.3130E+02	0.7423E+03
950	1.5915	0.1716	1.7638	0.1442	0.3005E+02	0.7627E+03
1000	1.6517	0.1737	1.8261	0.1453	0.2891E+02	0.7825E+03

APPENDIX 2

Computer Programs for Analysis of Differential Resistivity and Hall Effect Data

```
00100   C       NEWDA.F4
00200   C
00300   C       NEWDA.F4 IS THE SAME AS HDATI.F4 EXCEPT THE DATA IS READ IN
00400   C       AND OUT THROUGH DATA FILES (DA1.DAT AND DA2.DAT)
00500   C       THIS PROGRAM COMPUTES SHEET RESISTIVITY AND HALL COEFFICIENTS
00600   C       FOR DIFFERENTIAL DOUBLE AC VAN DER PAUW DATA
00700   C       NOTE: LPT 10 MUST BE ASSIGNED
00800   C       TO ENTER VAN DER PAUW DATA:  SOS DA1.DAT
00900   C       5F FORMAT:  VABCD(MV)  VBCDA(MV)  DELTAVBDAC(MV)  VAN DER PAUW
01000   C       FACTOR  CURRENT(MA)
01100   C       WHEN FINISHED ENTERING DATA IN DA1.DAT, TYPE ES TO DELETE
01200   C       LINE NUMBERS;  THEN  EX NEWDA.F4
01300   C       VALUES FOR SHEET RESISTIVITY AND HALL COEFFICIENT ARE
01400   C       AUTOMATICALLY ENTERED IN DA2.DAT
01500           REAL I(50)
01600           DIMENSION V1(50),V2(50),DV(50),F(50),RS(50),RH(50),US(50),CS(50)
01700
01800           OPEN(UNIT=20,ACCESS='SEQIN',MODE='ASCII',FILE='DA1.DAT')
01900           OPEN(UNIT=21,ACCESS='SEQOUT',MODE='ASCII',FILE='DA2.DAT')
02000           TYPE 1
02100       1   FORMAT(2X,'TYPE IN',/,2X,'B(GAUSS)',2X,
02200         1 '# OF DATA POINTS',2X,'HALL COEFFICIENT FACTOR'/)
02300           ACCEPT 2,B,N,HCF
02400       2   FORMAT(F,I,F)
02500           WRITE(10,6) B,HCF
02600       6   FORMAT(3X,'B =',2X,F6.1,' GAUSS',5X,'HALL COEFFICIENT FACTOR = '
02700         1 ,F5.2/)
02800           DO 4 M=1,N
02900           READ(20,5,END=4) V1(M),V2(M),DV(M),F(M),I(M)
03000       5   FORMAT (5F)
03100       4   CONTINUE
03200           WRITE(10,30)
03300      30   FORMAT(3X,'SHEET RESISTIVITY',3X,'HALL COEFFICIENT',5X,
03400         1 'MOBILITY',7X,'SHEET CARRIER CONC',3X,'VABCD',5X,'VBCDA',6X,
03500         1 'DVBDAC',6X,'F',7X,'I'/)
03600           WRITE(10,35)
03700      35   FORMAT(7X,'(OHM/SQ)',8X,'(CM**2/COUL)',7X,'(CM**2/V/SEC)',
03800         1 7X,'(CM**-2)',12X,'MV',8X,'MV',9X,'MV',16X,'MA'/)
03900           DO 15 K=1,N
04000           RS(K)=3.14159/ALOG(2.)*(V1(K)+V2(K))/(2.*I(K))*F(K)
04100           RH(K)=DV(K)/(I(K)*B*1.0E-8)*SQRT(2.0)
04200           US(K)=RH(K)/(RS(K)*HCF)
04300           CS(K)=HCF/(1.60219E-19*RH(K))
04400           WRITE(10,40) RS(K),RH(K),US(K),CS(K),V1(K),V2(K),DV(K),F(K),I(K)
04500           WRITE(21,101)  RS(K),RH(K)
04600     101   FORMAT(5X,E11.5,9X,E11.5)
04700      40   FORMAT(5X,E11.5,9X,E11.5,8X,F8.2,9X,E11.5,7X,F7.3,3X,F7.3,2X,
04800         1 E10.4,2X,F5.3,3X,E8.3)
04900      15   CONTINUE
05000           END
```

```
00100   C       NEWPR.F4
00200   C
00300   C       NEWPR.F4 IS THE SAME AS HPRFL.F4 EXCEPT THE DATA IS READ IN
00400   C       THROUGH A DATA FILE (DA2.DAT)
00500   C       THIS PROGRAM COMPUTES CARRIER CONCENTRATION PROFILES FROM
00600   C       DIFFERENTIAL RESISTIVITY AND HALL COEFFICIENT DATA
00700   C       NOTE: LPT 10 MUST BE ASSIGNED
00800   C       TO ENTER DATA:  SOS DA2.DAT
00900   C       2F FORMAT:  SHEET RESISTIVITY(OHM/SQ)  SHEET HALL COEFFICIENT
01000   C       (CM**2/COUL)
01100   C       WHEN FINISHED ENTERING DATA IN DA2.DAT, TYPE ES TO DELETE LINE
01200   C       NUMBERS;  THEN  EX NEWPR.F4
01300           DIMENSION SIGMA(50),UH(50),UC(50),CC(50),DEP(50)
01400           DIMENSION RS(50),RH(50)
01500           TYPE 1
01600     1     FORMAT(2X,'TYPE IN',/,2X,'STEP SIZE (A)',5X,'# OF DATA POINTS',
01700        1  5X,'HALL COEFFICIENT FACTOR'/)
01800           ACCEPT 2,D,N,HCF
01900     2     FORMAT( F,1,F)
02000           WRITE(10,12) HCF
02100     12    FORMAT(2X,'HALL COEFFICIENT FACTOR = ',F5.2/)
02200           WRITE(10,6) D
02300      6    FORMAT(2X,'RS (OHM/SQ)',5X,'RH (CM**2/COUL)',5X,'STEP SIZE ='
02400        1  ,F7.1,2X,'(A)'/)
02500           OPEN(UNIT=21,ACCESS='SEQIN',MODE='ASCII',FILE='DA2.DAT')
02600           DO 4 M=1,N
02700           READ (21,5) RS(M),RH(M)
02800     5     FORMAT (2F)
02900           WRITE(10,7) RS(M),RH(M)
03000      7    FORMAT(2X,E10.5,7X,E11.5)
03100     4     CONTINUE
03200           WRITE(10,30)
03300     30    FORMAT (2X,///,2X,'DEPTH (A)',3X,'MOBILITY (CM**2/V/SEC)',3X,'
03400        1   CARRIER CONC (CM**-3)'/)
03500           DO 15 K=1,N
03600           IF (K-1) 20,15,20
03700     20    SIGMA(K)=1.E8/D*(1./RS(K-1)-1./RS(K))
03800           UH(K)=RH(K-1)/RS(K-1)+RH(K)/RS(K)-(RH(K)-RH(K-1))/(RS(K)-RS(K-1))
03900           UC(K)=UH(K)/HCF
04000           CC(K)=SIGMA(K)/(1.60219E-19*UC(K))
04100           DEP(K)=D*(K-1.5)
04200           WRITE (10,35) DEP(K),UC(K),CC(K)
04300     35    FORMAT(3X,F7.1,12X,F6.1,17X,E)
04400     15    CONTINUE
04500           END
```

```
00100   C       NEWPR2.F4
00200   C
00300   C       NEWPR2.F4 IS THE SAME AS HPRFL2.F4 EXCEPT THE DATA IS READ
00400   C       IN THROUGH A DATA FILE (DA2.DAT)
00500   C       THIS PROGRAM INCLUDES DATA SMOOTHING BY AVERAGING TWO
00600   C       DATA POINTS
00700   C
00800           DIMENSION SIGMA(80),UH(80),UC(80),CC(80),DEP(80)
00900           DIMENSION RS(80),RH(80)
01000           TYPE 1
01100     1     FORMAT(2X,'TYPE IN',/,2X,'STEP SIZE (A)',5X,'# OF DATA POINTS',
01200        1  5X,'HALL COEFFICIENT FACTOR'/)
01300           ACCEPT 2,D,N,FUDGE
01400     2     FORMAT( F,1,F)
01500           WRITE(10,12) FUDGE
01600     12    FORMAT(2X,'HALL COEFFICIENT FACTOR = ',F5.2/)
01700           WRITE(10,6) D
01800      6    FORMAT(2X,'RS (OHM/SQ)',5X,'RH (CM**2/COUL)',5X,'STEP SIZE ='
01900        1  ,F7.1,2X,'(A)'/)
02000          OPEN(UNIT=21,ACCESS='SEQIN',MODE='ASCII',FILE='DA2.DAT')
02100           DO 4 M=1,N
02200          READ(21,5) RS(M),RH(M)
02300     5     FORMAT (2F)
02400           WRITE(10,7) RS(M),RH(M)
02500      7    FORMAT(2X,E10.5,7X,E11.5)
02600     4     CONTINUE
02700           WRITE(10,30)
02800     30    FORMAT (2X,///,2X,'DEPTH (A)',3X,'MOBILITY (CM**2/V/SEC)',3X,'
02900        1   CARRIER CONC (CM**-3)'/)
03000           DO 15 K=1,N
03100           IF (K-2) 15,15,20
03200     20    SIGMA(K)=0.5E8/D*(1./RS(K-2)-1./RS(K))
03300           UH(K)=0.5*(RH(K-2)/RS(K-2)+2.0*RH(K-1)/RS(K-1)+RH(K)/RS(K))
03400        1  -0.5*((RH(K)-RH(K-1))/(RS(K)-RS(K-1))+(RH(K-1)-RH(K-2))/
03500        1  (RS(K-1)-RS(K-2)))
03600           UC(K)=UH(K)/FUDGE
03700           CC(K)=SIGMA(K)/(1.60219E-19*UC(K))
03800           DEP(K)=D*(K-2)
03900           WRITE (10,35) DEP(K),UC(K),CC(K)
04000     35    FORMAT(3X,F7.1,12X,F6.1,17X,E)
04100     15    CONTINUE
04200           END
```

APPENDIX 3

Capacitance and Differential Capacitance-Voltage Measurement

There are many different methods for profiling low-concentration carrier profiles by capacitance-voltage measurement. Our system is based on a second-harmonic principle.

III.1. Principle

When a test diode is reverse bias by V_0, a small signal $a\sin\omega t$ is applied in addition to the reverse bias. The space charge then varies as

$$dQ = C(v)dv$$

$$= C(V_0 + dv)dv$$

$$= C(V_0)dv + C'(V_0)d^2v + \ldots.$$

where $v = V_0 + a\sin\omega t$

The small current changes due to dQ as

$$i = \frac{dQ}{dt}$$

$$= C(V_0)\, a\omega\cos\omega t + \frac{dC}{dV}(V_0)\,\frac{a^2}{2}\,\omega \sin 2\omega t + \ldots.$$

We neglect all terms higher than the 2nd power. Therefore, capacitance $C(V_0)$ is proportional to the first harmonic term of i, 90° out of phase. dC/dV is proportional to the second harmonic term in i, in phase. By using a PAR 181 current-sensitive preamplifier and a PAR 186 lock-in amplifier, we can plot C-V and $\frac{dC}{dV}$ - V directly on an X-Y recorder (Fig. 2.4).

III.2. Procedures for measurement

1. Calibrate the system with the standard capacitor.
2. When the calibration is complete, remove the standard capacitor and incorporate the test diode into the system as shown in Fig. 2.4.
3. Make a C-V plot, where reference frequency is f.
4. Retard the phase 90^{o} with the PAR 186 phase switch. Then set reference frequency 2f.
5. Adjust the sensitivity in the PAR 186 and X-Y recorder and record the ranges.
6. Make a second harmonic plot.

III.3. Computer program for data analysis

```
00100   C       CAP.F4
00200   C
00300   C
00400   C       THIS IS A PROGRAM TO CALCULATE THE IMPURITY PROFILE BY
00500   C       USING CAPACITANCE VALUE VS VOLTAGE
00600           DIMENSION C(50),DCDV(50),X(50),RN(50),V(50)
00700           DATA PI,EPISON/3.141593,1.03662/
00800           TYPE 10
00900   10      FORMAT('      THE NUMBER OF DATA POINTS',T30,'FREQUENCY')
01000           ACCEPT 20,N,FREQ
01100   20      FORMAT(I,E)
01200           TYPE 30,N,FREQ
01300   30      FORMAT(2X,I3,25X,E12.4)
01400           TYPE 35 .
01500   35      FORMAT(T5,'V(I)',T11,'C(I)(PF)',T21,'DC/DV(MV)')
01600           ACCEPT 40,(V(I),C(I),DCDV(I),I=1,N)
01700   40      FORMAT(3F)
01800           TYPE 50
01900   50      FORMAT(' CROSSING AREA(CM**2)',T20,'SIGNAL VOLTAGE(MV)',
02000           1T42,'SENSITIVITY(AMP)',T60,'CORRECTION')
02100           ACCEPT 60,A,SIGN,SEN,CORR
02200   60      FORMAT(E,F,E,F)
02300           FACT1=EPISON*A
02400           FACT2=SQRT(2.)*SEN*1.2E12/((SIGN)**2*1.E-3*FREQ*2.*PI)
02500           FACT3=1.602E-19*EPISON*A**2*1E12
02600           WRITE(3,110)
02700   110     FORMAT(1H1,3X,'VOLTAGE(V)',3X,'CAPACITANCE(PF)',3X,'DEPTH(UM)',
02800           13X,'DC/DV(PF/V)',3X,'CONCENNTRATION(CM**-3)')
02900           DO 200 J=1,N
03000           X(J)=FACT1/C(J)*1.E4
03100           DCDV(J)=FACT2*DCDV(J)*CORR
03200           RN(J)=C(J)**3/(FACT3*DCDV(J))
03300           WRITE(3,150) (V(J),C(J),X(J),DCDV(J),RN(J))
03400   150     FORMAT(1H0,5X,F5.2,10X,F7.2,6X,F8.3,6X,F8.3,10X,E12.4)
03500   200     CONTINUE
03600           END
```

APPENDIX 4

Hyperabrupt Junction Voltage Variable Capacitors Achieved by Ion-Implantation

To demonstrate the versatility of doping by ion-implantation, voltage variable capacitors (varactors) suitable for linear tuning have been successfully fabricated by using ion-implantation and an Al-Si Schottky barrier. Multiple implants of boron into a p-type silicon wafer are used to synthesize an impurity profile $N_A - N_D = Bx^{-\frac{3}{2}}$. The energies and doses of multiple implants are calculated by a computer program, which gives the optimal summation of Gaussians to construct the desired profile. The varactors with this profile have $C = K(V + V_b)^{-1.9}$ characteristics over a factor of three change in capacitance, where V is an applied reverse bias and V_b is a constant voltage due to the lack of an infinite impurity concentration at the surface (Fig. A.1).

An impurity profile measured by the differential capacitance technique shows the device has the desired electrically active $Bx^{-\frac{3}{2}}$ profile (Fig. A.2). The capacitance varies with the -1.9 power of voltage instead of the -2.0 power. This may be attributed to the discrepancy between the LSS computed profile and the electrically active profile.

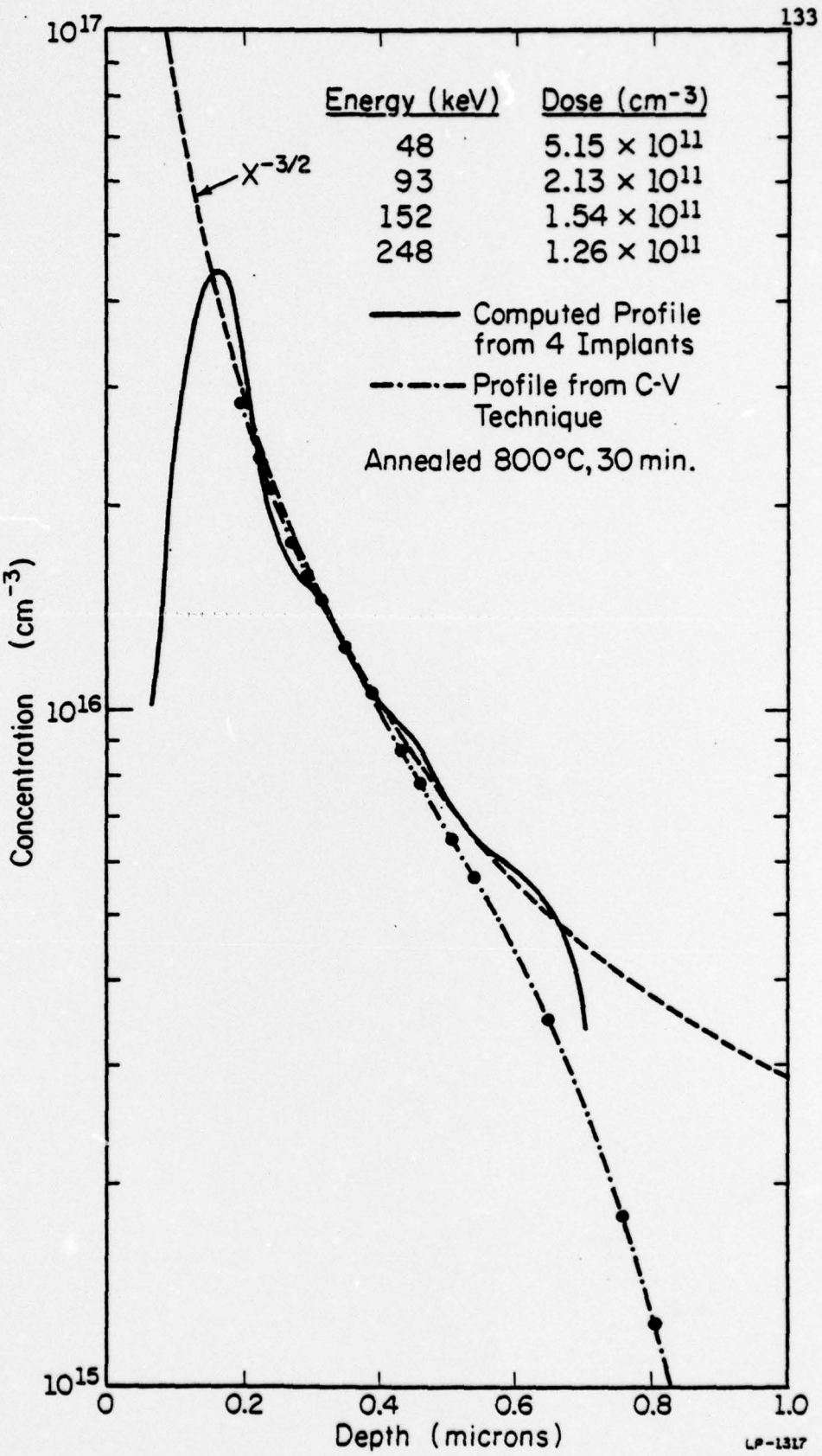

A.1. Electrical carrier concentration and computed atomic profiles for a varactor fabricated by multiple implants shown.

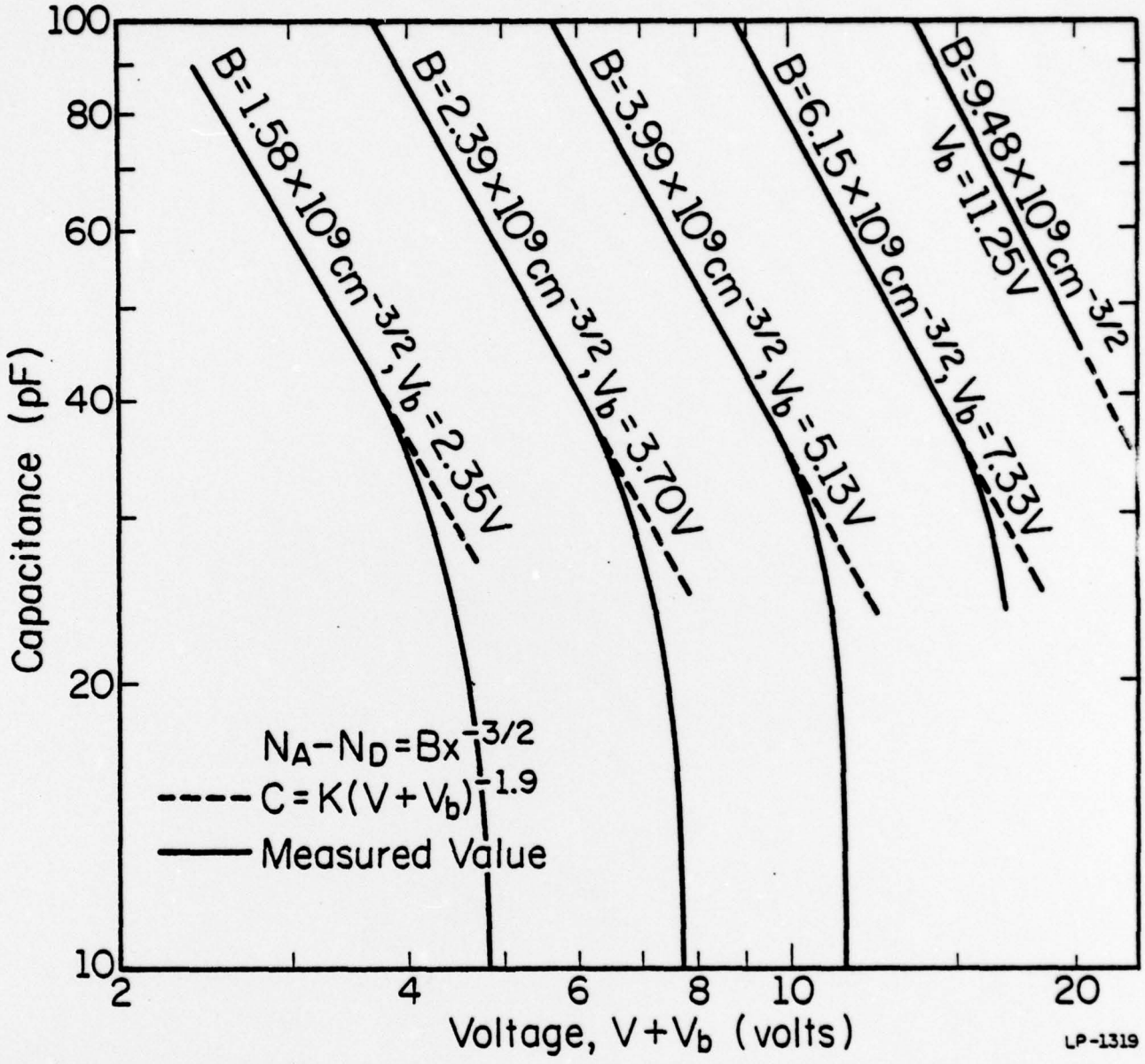

A.2. C-V relationship for varactors synthersizing $N_A - N_B = BX^{-3/2}$ by multiple implants. V_b is the constant off-set voltage due to the lack of an infinite impurity concentration at the surface.

VITA

Mon Yen Tsai was born on January 16, 1950 in Taipei, Taiwan. He attended National Taiwan University at Taipei, Taiwan where he received a Bachelor of Science in Electrical Engineering with highest honor in June 1972. Since September 1974, he has been attending the University of Illinois at Urbana-Champaign. He received a Master of Science degree in Electrical Engineering in October 1975. Mr. Tsai is a member of the Institute of Electrical and Electronic Engineers and the Phi Kappa Phi honor society.